Evaluation of the Performance of Coherent Optical Communications Commercial DSP ASICs in Low Earth Orbit Radiation Environments

by

Raichelle Joy Aniceto

B.S. Aerospace Engineering
Massachusetts Institute of Technology, 2016

Submitted to the Department of Aeronautics and Astronautics
in partial fulfillment of the requirements for the degree of

Master of Science in Aeronautics and Astronautics

at the

MASSACHUSETTS INSTITUTE OF TECHNOLOGY

June 2017

Signature redacted

Signature of Author ....
Department of Aeronautics and Astronautics
May 18, 2017

Signature redacted

Certified by ....
Kerri Cahoy
Assistant Professor of Aeronautics and Astronautics
Thesis Supervisor

Signature redacted

Accepted by ....
Youssef M. Marzouk
Associate Professor of Aeronautics and Astronautics
Chair, Graduate Program Committee

Evaluation of the Performance of Coherent Optical Communications Commercial DSP ASICs in Low Earth Orbit Radiation Environments

by

Raichelle Joy Aniceto

Submitted to the Department of Aeronautics and Astronautics
On May 18, 2017 in Partial Fulfillment of the Requirements for the Degree of
Master of Science in Aeronautics and Astronautics

ABSTRACT

Coherent optical communications systems on satellites have the potential to contribute meeting to world-wide data capacity demand. Digital signal processing (DSP) application specific integrated circuits (ASICs) for coherent optical communications systems, first developed in 2008 with current capabilities of over 100 Gbps for commercial terrestrial applications, are a key technology needed for space-based applications. However, in order to develop coherent optical communications systems for space applications, the performance of these commercial ASICs must be evaluated with consideration of the radiation effects from the space environment. This work investigates the performance of the Inphi CL20010A1 optical coherent DSP ASIC in a low earth orbit (LEO) radiation environment and assesses whether this ASIC could be a viable option for a coherent optical communications system on a LEO spacecraft.

The approach consists of simulation and experiment. First the radiation environment is modeled for three sample LEO orbits: International Space Station (ISS) orbit, 800 km polar orbit, and 1000 km 0° inclination, for 1-year, 5-year, and 10-year mission durations. Total ionizing dose (TID) requirements were determined for each mission and used to experimentally evaluate the TID tolerance of the CL20010A1. The CL20010A1 on an evaluation board system (EVK) is modeled and simulations with Stopping Range In Matter (SRIM) program are used to simulate 64.0 MeV protons penetrating through the system. The SRIM simulations are used to calculate the proton energy levels entering the silicon active region of the CL20010A1 and to determine the proton energy level sufficient for depositing ionizing dose in the active region and penetrating through the active region. The simulations determine the lower threshold of proton energy level needed for experimental testing.

Two proton test campaigns of the CL20010A1-EVK were completed at UC Davis Crocker Nuclear Laboratory (CNL) and Tri-University Meson Facility (TRIUMF) using energy levels of 64.0 MeV and 480 MeV, respectively. The CL20010A1 ASIC survived and experienced no performance degradation from TID exposure up to 170 krad(Si). The measured CL20010A1 single event effect (SEE) cross section was 2.46×10^{-9} cm^2 at the 64 MeV proton energy level and 3.82×10^{-10} cm^2 at the 480 MeV proton energy level.

The SEE cross section data from the proton test campaigns was used to calculate the CL20010A1 SEE rate for the sample LEO missions. The SEE cross section results were compared to the results from previous studies on proton-induced SEEs of other Complementary Metal Oxide Semiconductor (CMOS) devices with silicon active regions. Mitigation strategies against LEO radiation effects for the CL2001A1 are considered, such as spot shielding, strategic placement in spacecraft, incorporation of protective electronic devices in the circuit system design, and programming periodic CL20010A1 resets or full system power cycles. Expansion of this work, such as additional proton radiation test campaigns at different energy levels below 64.0 MeV and between 64.0 MeV and 480 MeV as well as heavy ion test campaigns to assess SEEs induced by heavy ions from galactic cosmic rays (GCRs) and solar energetic particles (SEPs), would provide additional insights on potential effects of the LEO radiation environment on the CL20010A1. Heavy ion test campaigns would provide SEE cross section data, which could be used to calculate the expected heavy-ion induced SEE rate for a given LEO mission. This work serves as an initial step toward the development of a DSP coherent optical communications transceiver for LEO satellite applications.

Thesis Supervisor: Kerri Cahoy
Title: Associate Professor of Aeronautics and Astronautics

Acknowledgements

I would like to acknowledge and thank my graduate advisor, Dr. Kerri Cahoy for her support of this work and for her guidance throughout my time in the MIT Department of Aeronautics and Astronautics Master of Science program. I would not be where I am today without Kerri's continued support and encouragement since freshman year of my MIT undergraduate education.

I would like to also acknowledge my technical mentor Dr. Slaven Moro for his support and guidance with my thesis research. I sincerely thank him for all of the opportunities he has provided for me to learn and grow technically. I am grateful for all of his time and effort spent in the laboratory to teach me about optical communications technology. I would also like to thank Dr. Randall Milanowski for providing his expertise and knowledge with radiation. He has significantly supported this work through teaching me how to use SRIM and providing insight on radiation effects. Special thanks to Christopher Isabelle, Norman Hall, and Bert Vermeire for assistance with proton radiation test campaigns.

I would like to also thank my personal mentor, Dr. Whitney Lohmeyer. She is my role model and the source of my inspiration to pursue graduate school. She provided helpful insight, feedback, and advice for this thesis. I would also like to thank Marie Stuppard, Beth Marois, and Professor Eytan Modiano for their support toward my completion of the Master of the Science Degree.

Special thanks to my colleagues and friends. William Tang provided useful insight on chemical compounds and material composition. Emily Clements provided helpful resources and guidance with optical communications systems. Rodrigo Diez provided useful information on electronic components used to mitigate against radiation effects.

Finally, I would like to thank my parents, Romeo and Ruth Aniceto, for their encouragement and prayers throughout my journey in the MIT AeroAstro Master of Science program.

Contents

1. Introduction 22

1.1 Free-Space Optical Communications Systems 22

1.1.1 Space-Based FSOC Systems in Development 23

1.1.2 Demonstrated Space-Based FSOC Systems 25

1.2 Coherent Optical Communications Systems 28

1.3 Thesis Structure 32

2. Low Earth Orbit Radiation Environment 35

2.1 Low Earth Orbit Radiation Environment 35

2.1.1 Trapped Particles in the Inner Radiation Belt 36

2.1.2 Galactic Cosmic Rays 39

2.1.3 Solar Energetic Particles 39

2.1.4 Summary of Low Earth Orbit Radiation Environment 40

2.2 Low Earth Orbit Radiation Environment Effects of Spacecraft Components 41

2.2.1 Total Ionizing Dose Effects 42

2.2.2 Total Non-Ionizing Dose or Displacement Damage Effects 44

2.2.3 Single Event Effects 45

2.2.3.1 Types of Single Event Effects 46

2.2.3.2 Single Event Effect Rate 49

2.2.4 Summary of Low Earth Orbit Radiation Effects of Spacecraft Devices 51

2.3 OMERE Radiation Environment Analyses for Sample Low Earth Orbit Missions 52

3. CL20010A1 Optical Coherent DSP ASIC 59

3.1 CL20010A1 ASIC Description 59

3.1.1 CL20010A1 ASIC Functionality 59
3.1.2 CL20010A1 ASIC Evaluation Board System 61
3.2 Potential Radiation Damage to the CL20010A1 ASIC in a Low Earth Orbit Space Environment 63
3.2.1 Ionizing Radiation Damage to CMOS Devices 64
3.2.2 Total Ionizing Dose and Single Event Upset Trends in CMOS Devices 65

4. SRIM Analyses of the CL20010A1 ASIC **67**
4.1 CL20010A1-EVK System Modeling 69
4.2 TRIM Analyses of CL20010A1-EVK System 72
4.2.1 Integrated CL20010A1-EVK System TRIM Simulation 75
4.2.1.1 Worst Case Integrated System TRIM Simulation 77
4.2.2 Layer-by-Layer CL20010A1-EVK System TRIM Simulations 78
4.2.2.1 Worst-Case Layer-by-Layer System TRIM Simulation 81
4.3 TRIM Analyses Summary 83

5. Single Event Effect and Total Ionizing Dose Assessment of the CL20010A1 ASIC with Proton Radiation Test Campaigns **85**
5.1 Experimental Approach 86
5.1.1 Single Event Effect and Total Ionizing Dose Proton Test Campaign at Crocker Nuclear Laboratory Facility 86
5.1.2 Single Event Effect Proton Test Campaign at TRIUMF National Laboratory 88
5.2 Experimental Results 90
5.2.1 Single Event Effects 90
5.2.2 Total Ionizing Dose 91

6. Single Event Effect Calculations for CL20010A1 ASIC **93**
6.1 Proton Single Event Effect Cross Section Calculations and Analyses . . . 94

6.2 Proton Single Event Effect Rate Calculations for the CL20010A1 ASIC 98

7. Mitigation Strategies Against Radiation Damage to the CL20010A1 ASIC 102
7.1 Spot Shielding 102
7.2 Strategic Placement in Spacecraft 103
7.3 Incorporation of Protective Electronic Devices in Circuit System Design 103
7.4 Programming Periodic CL20010A1 Resets or Full System Power Cycles 104

8. Conclusions and Future Work 106
8.1 Conclusions 106
8.2 Future Work 108
  8.2.1 Additional Proton Radiation Test Campaigns 108
  8.2.2 Heavy Ion Radiation Test Campaigns 110
  8.2.3 Development of Coherent Optical Transceiver for LEO Spacecraft Application 111

9. Appendix 113
A1. Single Event Effects 113
A2. Matlab Script for TRIM Simulation Data Analyses 114

List of Figures

Figure 1.1 Demonstrated FSOC missions based on maximum optical link distance, data rate, and transmit power

Figure 1.2 Approach used in this work to evaluate the CL20010A1 ASIC for LEO space radiation environment

Figure 2.1 High-level approach used in this work to evaluate the CL20010A1 ASIC for LEO space radiation environment with Chapter 2 accomplishments highlighted in yellow.

Figure 2.2 Integral flux mapping for 1 MeV trapped protons. The OMERE flux mapping module used to model trapped protons with AP8-MIN and IGRF for Earth's magnetic field. Red represents trapped protons with highest fluxes between ~1 x 10^6 and ~1 x 10^7 particles/cm^2/s, yellow represents fluxes between ~5 x 10^4 and ~1 x 10^6 particles/cm^2/s, and green represents fluxes between ~1 x 10^2 and ~5 x 10^4 particles/cm^2/s.

Figure 2.3 Integral flux mapping for 1 MeV trapped electrons. The OMERE flux mapping module is used to model trapped protons with AE8-MAX and IGRF for Earth's magnetic field. Red represents trapped protons with the highest fluxes between ~1 x 10^6 and ~1 x 10^7 particles/cm^2/s, yellow-orange represents fluxes between ~5 x 10^4 and ~1 x 10^6 particles/cm^2/s, and green represents fluxes between ~1 x 10^2 and ~5 x 10^4 particles/cm^2/s.

Figure 2.4 OMERE model of trapped protons. Concentration of high energy protons near the region southeast of Brazil highlights the South Atlantic Anomaly. Red represents trapped protons with the highest fluxes between ~1 x 10^7 and ~1 x 10^8 particles/cm^2/s, yellow-orange represents fluxes between ~5 x 10^4 and ~1 x 10^7 particles/cm^2/s, and green represents fluxes between ~1 x 10^2 and ~5 x 10^4 particles/cm^2/s.

Figure 2.5 LEO radiation environment sources, types of particles from each source, and radiation effects caused by each type of particle

Figure 2.6 Non-destructive and destructive SEEs

Figure 2.7 (a,b,c,d). Dose depth curves for LEO Mission at ISS Orbit for (a 1-year, (b) 5-year, and (c) 10-year (bottom left) mission durations, showing TID and contributions from trapped particles, bremsstrahlung protons, and solar protons. Estimated TID comparison for all three mission durations (d). The TID values at 100 mils aluminum shielding thickness are marked and labeled.

Figure 2.8 (a,b,c,d). Dose depth curves for LEO Mission at 800 km polar orbit for 1-year (a), 5-year (b), and 10-year (c) mission durations, showing TID and contributions from trapped particles, bremsstrahlung protons, and solar protons. Estimated TID comparison for all three mission durations (d). The TID values at 100 mils aluminum shielding thickness are marked and labeled.

Figure 2.9 (a,b,c,d). Dose depth curves for LEO Mission at 1000 km, 0° inclination orbit for 1-year (a), 5-year (b), and 10-year (c) mission durations, showing TID and contributions from trapped particles, bremsstrahlung protons, and solar protons. Estimated TID comparison for all three mission durations (d). The TID values at 100 mils aluminum shielding thickness are marked and labeled.

Figure 3.1 Egress and ingress data paths for CL20010A1 ASIC as interface between host system and optical components [Inphi, 2014].

Figure 3.2 Data Path through CL20010A1 ASIC [Inphi, 2014].

Figure 3.3 CL20010A1 ASIC integrated on EVK with optical transceiver. Computer and power supply connected to EVK.

Figure 3.4 Test setup of CL20010A1-EVK system. CL20010A1-EVK connected to computer and power supplies.

Figure 4.1 High-level approach used in this work to evaluate the CL20010A1 ASIC for LEO space radiation environment with Chapter 4 accomplishments highlighted in yellow.

Figure 4.2 Energy loss for 64.0 MeV protons in silicon as a function of distance from material surface. Bragg peak indicated.

Figure 4.3 Model of CL20010A1 between EVK and Heat Sink

Figure 4.4 TRIM ionization data file "IONIZ.txt" used for calculating energy loss through EVK PCB copper layer.

Figure 4.5 Integrated CL20010A1-EVK System Model TRIM Simulation Method

Figure 4.6 Integrated system TRIM simulation of five thousand 64.0 MeV protons penetrating through CL20010A1-EVK system.

Figure 4.7 Integrated system TRIM simulation of five thousand 64.0 MeV protons penetrating through CL20010A1-EVK system Worst case scenario modeled for protons through copper-filled vias in PCB.

Figure 4.8 Layer-by-layer TRIM Simulation Method. The ionization energy level is input to a feedback loop, unlink the integrated simulation method in Figure 4.5.

Figure 4.9 Layer-by-layer TRIM simulation of five thousand 49.97 MeV protons penetrating through CL20010A1 ASIC silicon active region

Figure 4.10 "Worst case" layer-by-layer TRIM simulation of five thousand, 23.43 MeV protons penetrating through CL20010A1 ASIC silicon active region.

Figure 5.1 High-level approach used in this work to evaluate the CL20010A1 ASIC for LEO space radiation environment with Chapter 5 accomplishments highlighted in yellow.

Figure 5.2 CL20010A1 SEE and TID experimental block diagram for CNL Testing

Figure 5.3 EVK proton irradiation test setup at CNL; (left) front side of board with CL20010A1 in top right corner and CFP2-ACO in top left; (right) irradiated back side of board and laser used for proton beam alignment.

Figure 5.4 CL20010A1 SEU experimental block diagram for TRIUMF testing

Figure 5.5 EVK proton irradiation test setup at TRIUMF. Front side of board with CL20010A1 in top right corner and CFP2-ACO in top left. Laser used for proton beam alignment.

Figure 5.6 CL20010A1 Pre-FEC BER vs TID

Figure 6.1 High-level approach used in this work to evaluate the CL20010A1 ASIC for LEO space radiation environment. Chapter 6 accomplishments highlighted in yellow. The transition in the path with the SEE data collected from the proton test campaigns is showed. SEE rate calculation will be used to assess mitigation strategies against radiation effects on the CL20010A1.

Figure 6.2 CL20010A1 ASIC proton single event effect cross-section data

Figure 6.3 LET versus energy curve for protons through silicon target material

Figure 6.4 CL20010A1 proton SEE cross section Weibull fit curve

Figure 6.5 Nominal proton SEE cross section Weibull distribution behavior

List of Tables

Table 1.1 Demonstrated FSOC systems and key parameters

Table 2.1 Summary of LEO radiation sources, particles from radiation sources, particle energy level in LEO, and affects areas in LEO

Table 2.2. Types of SEEs and susceptible devices and technologies. Relevant SEEs to CL20010A1 ASIC indicated (*).

Table 2.3 Summary of radiation effects, types of particles inducing each effect, susceptible devices and technologies to radiation effects, and characterization of radiation effects

Table 2.4 LEO space missions modeled with OMERE

Table 2.5 Estimated total ionizing dose levels for sample LEO missions, calculated from OMERE radiation environment simulation.

Table 2.6 Total Ionizing Dose Requirements for sample LEO missions based on 100 mils aluminum shielding thickness and factor of 2 margin.

Table 4.1 CL20010A1-EVK system layers modeled into TRIM based on atomic composition, density, and layer thickness

Table 4.2 TRIM simulation results for CL20010A1-EVK integrated system model.

Table 4.3 TRIM simulation results for CL20010A1-EVK integrated system model worst-case scenario.

Table 4.4 CL20010A1-EVK system layer-by-layer TRIM model calculations for average ionization energy loss per target depth thickness, the total ionization energy loss, and the final ionization energy level at the end of the layer.

Table 4.5 CL20010A1-EVK system layer-by-layer TRIM model calculations for "worst-case" scenario of protons through PCB copper-filled vias. Calculations for average ionization energy loss per target depth thickness, the total ionization energy loss, and the final ionization energy level at the end of the layer.

Table 4.6 Summary of TRIM Simulation Results for ionization energy level of protons penetrating into and completely through the CL20010A1 ASIC active region.

Table 5.1 CL20010A1 SEE data from CNL test campaign with 64 MeV protons

Table 5.2 CL20010A1 SEE data from TRIUMF test campaign with 480 MeV protons.

Table 5.3 CL20010A1 ASIC TID data summary from CNL test campaign with 64 MeV protons

Table 6.1 SEE cross section results from proton beam testing of CL20010A1 ASIC

Table 6.2 Weibull parameters for curve fit from proton SEE cross section data.

Table 6.3 Proton SEE rate calculations for each modeled LEO orbit

Table 8.1 Proposed future proton test campaigns to further assess performance of CL20010A1 to LEO radiation effects.

List of Equations

Equation 2.1 Total ionizing dose calculation and units

Equation 2.2 Linear energy transfer as a function of ionizing energy loss and normalized by target density

Equation 2.3. Total ionizing dose as a function of the incident particle fluence and linear energy transfer

Equation 2.4 Non-ionizing energy loss as a function of nuclear energy loss and normalized by target density

Equation 2.5 Total non-ionizing dose as a function of the incident particle fluence and non-ionizing energy loss

Equation 2.6 Single event effect cross section calculation

Equation 2.7 Ion single event effect rate calculation. Integration of the product of the CREME rate at each linear energy transfer value and the linear energy transfer threshold distribution over the whole ion cross section curve

Equation 2.8 Proton single event effect rate calculation. Integration of the product of the proton cross section and the proton flux over all proton energy levels.

Equation 4.1 Total ionization energy loss by ions

Equation 4.2 Final ionization energy level of protons. Calculation used for integrated CL20010A1-EVK system approach.

Equation 4.3 Ionization energy level of protons at end of a layer. Calculation used for layer-by-layer CL20010A1-EVK system approach.

Equation 6.1 Functional form of the Weibull function used to calculate the proton single event effect cross section in units of cm^2

List of Abbreviations

ADC – Analog-to-Digital Converter

AFE – Analog Front End

ARTEMIS – Advanced Relay and TEchnology MIssion Satellite

ASIC – Application Specific Integrated Circuit

BCB – Benzocyclobutene

BCD – Bulk Chromatic Dispersion

BEOL – Back End of Line

BER – Bit Error Rate

BJT – Bipolar Junction Transistor

BPSK – Binary Phase Shift Keying

BT – Bismaleimide Trizxine

CCD – Charged Coupled Device

CD – Chromatic Dispersion

CFP2-ACO – Compact Form Pluggable 2 Analog Coherent Optics

CL20010Al-EVK – CL20010A1 ASIC Evaluation Board System

CME – Coronal Mass Ejections

CMOS – Complementary Metal Oxide Semiconductor

CNL – Crocker Nuclear Laboratory

COTS – Commercial Off The Shelf

CubeSat – Cube Satellite

DAC – Digital-to-Analog Converter

DC – Direct Current

DD – Displacement Damage

DLR – German Aerospace Center

DP – Dual Polarization

DRAM – Dynamic Random Access Memory

DSP – Digital Signal Processing

DUT – Device Under Test

EDFA – Erbium Doped Fiber Amplifier

EDC – Electronic Dispersion Compensation

ELDRS – Enhanced Low Dose Rate Sensitivity

ESA – European Space Agency

ETS – Engineering Test Satellite

EVK – Evaluation Board System

FEC – Forward Error Correction

FET – Field Effect Transistor

FLARE – Freespace Lasercom and Radiation Experiment

FPGA – Field Programmable Gate Array

FSOC – Free Space Optical Communications

Gbps – Gigabits Per Second

GEO – Geostationary Earth Orbit

GCR – Galactic Cosmic Ray

IC – Integrated Circuit

ICR – Integrated Coherent Receiver

ILD – Interlayer Dielectric

IP – Internet Protocol

JAXA – Japanese Aerospace Exploration Agency

JPL – Jet Propulsion Laboratory

keV – kilo-electron-Volt

LADEE – Lunar Atmosphere and Dust Environment Explorer

LCE – Laser Communications Experiment

LCL – Latch-Up Current Limiter

LCP – Liquid Crystal Polymeric

LCT – Laser Communications Terminals

LEO – Low Earth Orbit

LET – Linear Energy Transfer

LLCD – Lunar Laser Communications Demonstration

LLST – Lunar Laser Space Terminal

LO – Local Oscillator

LOL – Loss of Lock

LUCE – Laser Utilizing Communications Equipment

MAP – Constellation Mapping

Mbps – Megabit per second

MBU – Multiple Bit Upset

MCU – Multiple Cell Upset

MEMS – Micro-Electric Mechanical Systems

MEO – Mid-Earth Orbit

MeV – Mega-electron-Volt

MIT – Massachusetts Institute of Technology

NASA – National Aeronautics and Space Administration

NICT – National Institute of Information and Communications Technology

NIEL – Non-Ionizing Energy Loss

NFIRE – Near Field Infrared Experiment

NLC – Nonlinearity Compensation

NODE – Nanosatellite Optical Downlink Experiment

NPTC – Northeast Proton Therapy Center

NRZ – Non Return to Zero

NTIA – National Telecommunications and Information Administration

OBPF – Optical Bandpass Filter

OCSD – Optical Communications and Sensor Demonstration

OGS – Optical Ground Station

OICETS – Optical Inter-orbit Communications Engineering Test Satellite

OMERE – Outil de Modélisation de l'Environnement Radiatif Externe

OOK – On-Off Keying

OPALS – Optical Payload for Laser Communications Science

OSNR – Optical Signal to Noise Ratio

OTA – Optical Transceiver Assembly

Pbps – Petabits Per Second

PCB – Printed Circuit Board

PDL – Polarization Dispersion Loss

PI – Polyimide

PM – Polarization Multiplexed

PMD – Polarization Mode Dispersion

PMQ – Polarization-Multiplexed Quadrature

POL – Point of Load

PPO – Polyphenylene Oxide

PTFE – PolyTetraFluoroEthylene

QAM – Quadrature Amplitude Modulated

QPSK – Quadrature Phase Shift Key

Rad-Hard – Radiation-Hardened

RF – Radio Frequency

Rx – Receive

SAA – South Atlantic Anomaly

SD – Soft Decision

SEB – Single Event Burnout

SEDR – Single Event Dielectric Rupture

SEE – Single Event Effect

SEFI – Single Event Functional Interrupt

SEGR – Single Event Gate Rupture

SEHE – Single Event Hard Error

SEL – Single Event Latch-Up

SEP – Solar Energetic Particle

SESB – Single Event Stuck Bit

SET – Single Event Transient

SEU – Single Event Upset

SILEX – Semiconductor Inter-satellite Link Experiment

SOI – Silicon On Insulator

SPE – Solar Particle Event

SPOT4 – Satellite Pour l’Observation de la Terre 4

SRAM – Static Random Access Memory

SRIM – Stopping Range in Matter

TerraSAR-X – Synthetic Aperture Radar for Earth Observation

TID – Total Ionizing Dose

TNID – Total Non-Ionizing Dose

TRIM – Transport of Ions in Matter

TRIUMF – Tri-University Meson Facility

Tx – Transmit

VOA – Variable Optical Attenuator

WDM – Wavelength-Division Multiplexed

ZB – ZettaByte

Chapter 1

Introduction

Global Internet Protocol (IP) traffic is estimated to reach 2.3 zettabytes (ZB) (10^{21}) per year by 2020 [Cisco, 2016]. Satellite communications systems have the potential to play a key role in meeting worldwide data capacity demand as they evolve towards providing broadband that can augment or compete with terrestrial broadband. Satellite systems are well-suited for providing connectivity to large areas with low population densities and enable subscribers to connect to broadband and Internet backbone networks rapidly with little setup overhead required for the ground terminal, only a modem and an antenna. The cost to field satellite terminals for providing connectivity may be competitive with costs for point-by-point roll out of terrestrial fiber networks [ITU and UNESCO, 2015].

The development and launch of satellites as well as the construction of satellite broadband infrastructure is a still significant investment. Second to satellite launch costs, which can reach tens of millions of dollars, capital and operating expenditures for radio frequency (RF) gateways dominates the cost of connectivity via broadband systems. Due to limited bandwidth (*e.g.* K band), increasing capacity requires additional, spatially diverse ground gateway sites.

1.1 Free-Space Optical Communications Systems

Free space optical communications (FSOC) could serve as a viable and more cost-effective solution for future satellite systems. The larger carrier frequency and narrow transmit beamwidth of optical or laser communications are the key advantages over RF [Hemmati, 2008]. Higher frequency provides for greater bandwidth, reduces system mass, volume, and power consumption for transmit and receive apertures based on mission application, and allows for these systems to not be subjected to frequency regulation and spectrum restrictions of RF communications systems [Toyoshima, 2005; Cornwell, 2016]. The National Telecommunications and Information Administration (NTIA) of the United States Department of Commerce does not require authorization for the use of frequencies above 3000 GHz [NTIA, 2015]. However, the higher frequency of optical communications yields vulnerability to weather outages, such as cloud coverage, if crosslinks and multiple optical ground stations are not incorporated in the overall system design. A narrow beamwidth provides for greater power efficiency and potentially increased security, but at the cost of precision pointing control [Yoon, 2017]. FSOC systems are currently not as prevalent as RF communications systems on satellites due to challenges with fine beam pointing and cloud coverage [Hemmati, 2008]. As fine beam pointing technology further develops, mitigation strategies for cloud coverage progresses, and development of optical communications systems advances, there is significant potential for an increase in space-based, FSOC systems in the near future.

1.1.1 Space-Based FSOC Systems in Development

Currently, there are several efforts by industry, government entities, and academic institutions to develop FSOC systems for satellites. A few of the efforts are mentioned in this section, but many others exist.

Through funding with the National Aeronautics and Space Administration (NASA) Small Satellite Technology Program, the Aerospace Corporation is developing the Optical Communications and Sensor Demonstration (OCSD) for cube satellite (CubeSat) applications. OSCD-B on AeroCube-7B and OSCD-C on AeroCube-7C will be launched in late 2017 and are designed to downlink up to 200 Megabits per second (Mbps) at a 900 km distance from low Earth orbit (LEO) to a ground station. Each CubeSat with OCSD as payload is 2.5 kg [Janson and Welle, 2016].

The Aerospace Corporation and Draper Laboratory are in collaboration with BridgeSat to develop an optical communications network through the design of laser terminals on LEO satellites and optical ground stations [BridgeSat, 2017]. Vialight, founded in 2009, is a spin-off company from the German Aerospace Center (DLR), working on the development of satellite-to-ground optical communications system [Vialight, 2017]. Laser Light Communications intends to deploy a global optical network, HALO, consisting of up to 12 optical satellites in medium Earth orbit (MEO) with data rates up to 200 Gigabits per seconds (Gbps) for inter-satellite links and up to 100 Gbps for uplinks and downlinks between MEO and ground stations [Laser Light Communications, 2014].

Sinclair Interplanetary is working on optical communications for small spacecraft. Datasheets have been released for a laser crosslink system with data rates up to 100 Mbps at 250 km range and up to 6.25 Mbps at 1000 km range. The transmitter is designed with 1 W optical output power and the system weighs ~0.4 kg. A downlink laser transmitter system has been designed with data rates up to 1 Gbps for distances up to 1000 km and data rates up to 250 Mbps for distances up to 2000 km. The downlink transmitter system is designed with 1 W output power and has a mass of ~0.34 kg [Sinclair Interplanetary, 2017].

The Massachusetts Institute of Technology (MIT) is developing two FSOC demonstrations, the Nanosatellite Optical Downlink Experiment (NODE) and the Freespace Lasercom and Radiation Experiment (FLARE), for CubeSats. Both FSOC systems are designed with commercial off the shelf (COTS) components. NODE will be hosted on a CubeSat, which is scheduled for launch in 2017, and is designed for an optical downlink with 0.2 W transmit power and data rates up to 70 Mbps. FLARE is designed to demonstrate optical crosslinks between two LEO CubeSats with data rates greater than 10 Mbps [Clements, 2016].

1.1.2 Demonstrated Space-Based FSOC Systems

Within the past two decades, several FSOC systems have been successfully demonstrated with optical links between spacecraft and Earth ground stations as well as optical inter-satellite links.

The National Institute of Information and Communications Technology (NICT) performed the first bi-directional optical communications demonstration in 1994 between the Laser Communication Experiment (LCE) onboard the Engineering Test Satellite (ETS-VI) and both NICT optical ground station in Tokyo, Japan and Jet Propulsion Laboratory (JPL) optical ground station in Table Mountain, California. During the demonstration, ETS-VI was in a highly elliptical orbit of 38,700 km apogee, 8.560 km perigee, and 13-degree inclination. LCE weighed 22.4 kg and transmitted data with Manchester coded pulse modulation at ~1 Mbps. 13.8 mW average optical output power was transmitted over a 37,800 km link distance. [Araki et al., 1997].

In 2001, the European Space Agency (ESA) demonstrated Semiconductor Inter-satellite Link Experiment (SILEX), the first optical inter-satellite link from a LEO French spacecraft, Satellite Pour l'Observation de la Terre 4 (SPOT4), to a geostationary Earth orbit (GEO) spacecraft, Advanced Relay and TEchnology MIssion Satellite (ARTEMIS). The optical link was a distance of nearly 40,000 km with data rate of 50 Mbps using On-Off Keying (OOK) modulation with Non-Return to Zero (NRZ) coding [Tolker-Nielsen and Oppenhaeuser, 2002]. The SILEX terminals were about 100 kg [Fletcher et al., 1991]. The Japanese Aerospace Exploration Agency (JAXA) designed an optical communications terminal, Laser Utilizing Communications Equipment (LUCE), onboard the JAXA spacecraft Optical Inter-orbit Communications Engineering Test Satellite (OICETS). The LUCE system weighed 140 kg and transmitted an average of 100 mW. In 2005, LUCE and SILEX, onboard ARTEMIS, demonstrated the first bi-directional optical inter-orbit communications experiment between LEO and GEO. The optical link was nearly 40,000 km with the LEO to GEO uplink transmitting at data rate of 50 Mbps and the GEO to LEO downlink transmitting at data rate of 2 Mbps [Fujiwara et al., 2007; Toyoshima et al., 2004].

The DLR developed laser communications terminals (LCTs) based on homodyne binary phase shift keying (BPSK). One LCT was flown on the US satellite, Near Field Infrared Experiment (NFIRE) and a second LCT was flown on German satellite, Synthetic Aperture Radar for Earth Observation (TerraSAR-X). In 2008, the two LCTs demonstrated a LEO to LEO optical inter-satellite link over five thousand km distance at 5.625 Gbps [Gregory et al., 2011]. The LCT on TerraSAR-X also demonstrated an optical link at 5.625 Gbps from LEO to European Space Agency (ESA) Optical Ground Station (OGS) in Tenerife, Spain [Ciminelli et al., 2016]. The LCTs have a mass of 32 kg and a peak transmit power of 0.7 W [Fields et al., 2009].

MIT Lincoln Laboratory designed the Lunar Laser Communications Demonstration (LLCD) FSOC system, Lunar Laser Space Terminal (LLST) with mass of 30 kg, onboard the NASA mission, Lunar Atmosphere and Dust Environment Explorer (LADEE). In 2013, the LLST transmitted an optical downlink from lunar orbit to their Earth ground terminal with data rate of 622 Mbps and 0.5 W optical output power over 400,000 km maximum link distance [Robinson etal., 2011; Boroson etal., 2014].

In 2014, NASA JPL demonstrated the Optical Payload for Laser Communications Science (OPALS) system with an optical downlink from the International Space Station (ISS) to a ground station at Table Mountain, California. The OPALS system transmitted with a data rate of 50 Megabits per second (Mbps) using OOK modulation and Reed Solomon forward error correction (FEC). The system weighed 50 kg and transmitted with an average optical output power greater than 0.83 W [Oaida etal., 2014].

Table 1.1 summarizes FSOC systems that have been successfully demonstrated and describes some of the key parameters of each system.

Table 1.1 Demonstrated FSOC systems and key parameters

FSOC System	**Mass**	**Maximum Link Distance**	**Optical Link Source**	**Optical Link End**	**Data Rate**	**Detection**	**Tx Power**
OPALs (JPL 2014)	50 kg	700 km	ISS	Optical Ground Terminal (JPL)	50 Mbps	Direct	> 0.83 W
LLCD (MIT LL 2013)	30 kg	400000 km	Lunar Orbit (LADEE s/c)	Optical Ground Terminal	622 Mbps	Direct	0.5 W
LCT (DLR 2008)	32 kg	5100 km	LEO (NFIRE s/c)	LEO (TerraSAR-X s/c)	5.625 Gbps	Coherent	0.7 W
LCT (DLR 2008)	32 kg	5100 km	LEO (NFIRE s/c)	Optical Ground Terminal (ESA)	5.625 Gbps	Coherent	0.7 W
LUCE (JAXA 2005)	140 kg	38000 km	LEO (OICETS s/c)	GEO (ARTEMIS s/c)	50 Mbps	Direct	100 mW
SILEX (ESA 2005)	100 kg	38000 km	GEO (ARTEMIS s/c)	LEO (OICETS s/c)	2.048 Mbps	Direct	37 mW
SILEX (ESA 2001)	100 kg	38000 km	LEO (SPOT4 s/c)	GEO (ARTEMIS s/c)	50 Mbps	Direct	60 mW
LCE (NICT 1994)	22.4 kg	38700 km	Elliptical Orbit (ETS-VI)	Optical Ground Terminal (NICT, JPL)	1.024 Mbps	Direct	13.8 mW

A majority of the described FSOC systems were designed with direct detection optical communications systems and reached data rates on the order of 100s of Mbps. Figure 1.1 plots the demonstrated FSOC missions based on the maximum optical link distance and maximum achieved data rate. LCT designed by DLR achieved the highest data rate of 5.625 Gbps with a coherent optical communications system.

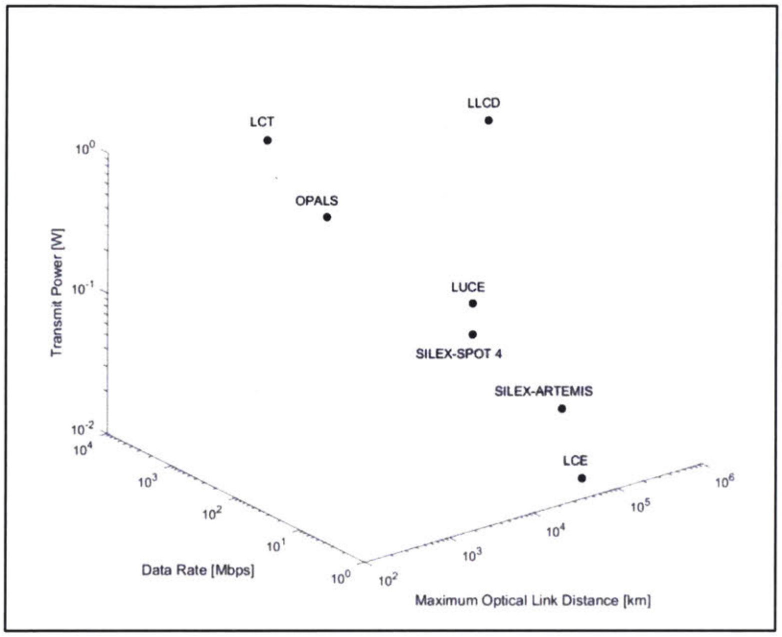

Figure 1.1 Demonstrated FSOC missions based on maximum optical link distance, data rate, and transmit power

In comparison to a direct detection system, a coherent system uses both the phase and intensity of a light wave to transmit information. In a direct detection system, the received optical signal is focused directly onto a photodetector, which generates a signal current proportional to the number of photons received. In a coherent system receiver, the received optical signal is superimposed with a light wave generated by a local oscillator (LO) laser and both optical signals are focused onto a photodetector. The signal current from the photodetector is non-linear and is dependent on the amplitude, phase, and polarization of the received optical signal and LO light wave [Pribil and Hemmati, 2008]. Coherent optical communications have the potential to meet high bandwidth and data capacity demands through multi-level modulation formats [Xiang et al., 2014].

1.2 Coherent Optical Communications Systems

Coherent optical communications systems will serve a key role in terrestrial optical network capacity expansion [Xiang et al., 2014]. Coherent systems have potential to achieve highest receiver sensitivity, high spectral efficiency, tolerance against dispersion effects, and superior performance over long transmission distances [Pfau et al., 2008]. The performance of optical coherent detection systems could enable future systems with transmission at 200 Gbps, 400 Gbps, and up to 1000 Gbps per wavelength [Roberts et al., 2009].

Coherent optical communications were studied in the 1980s, however, interest shifted toward wavelength-division multiplexed (WDM) direct detection using erbium-doped fiber amplifiers (EDFAs). In the past few years, there has been revived interest in coherent systems since recent technological advancements in optical coherent receivers and high speed digital circuits now allow for realization of coherent optical communications [Kikuchi, 2010]. Coherent optical receivers require high-speed analog-to-digital converters (ADCs) with sampling rates which can reach the symbol rate of high data rate signals. Fast circuit ADCs have been developed with sampling rates greater than 10 Giga-samples per second to meet the needs of high data rate coherent optical communications systems [Pfau et al., 2008].

Digital signal processing (DSP) through application specific integrated circuits (ASICs) is the key technological advancements to the realization of coherent optical communications systems. Prior to the development of optical coherent DSP ASICs in 2007, coherent systems would store transmitted data in a computer and analyze bit errors offline. The combination of coherent detection and DSP through an ASIC provides for real-time operation of digital coherent receivers [Savory, 2008; Kikuchi, 2010]. Advances to Complementary Metal Oxide Semiconductor (CMOS) ASIC technology affords the ADCs and DSP necessary to access and manipulate optical electric field signal for optical coherent systems [Roberts et al., 2009].

Optical coherent DSP ASICs have streamlined complex optical and analog functions to simplify transceiver implementation. DSP ASICs have integrated capabilities of analog-to-digital conversion, FEC encoding, constellation mapping (MAP), fiber nonlinearity compensation (NLC), electronic dispersion pre-compensation (EDC), and link equalization [Rasmussen et al., 2013]. Fast demultiplexers built into ASICs provide high speed interfaces with the input signals from ADCs [Pfau et al., 2008]. DSP ASICs optimize optical coherent system performance by providing robustness to additive noise and tolerance to linear transmission impairments, such as chromatic dispersion (CD) and polarization mode dispersion (PMD) [Rasmussen et al., 2013].

Optical coherent DSP ASICs can also reduce the size, cost, and power consumption of optical communications systems. Optical coherent ASICs with advanced DSP techniques can improve transmission capacity and performance for a given set of optoelectronic components, and DSP can be used to compensate for high dispersion, error, or noise [Xiang et al. 2014]. Implementation of a DSP ASIC with integrated low-cost optoelectronic components can yield an overall lower-cost optical communications system. However, customized optical coherent DSP ASICs can have high development costs in the range of tens of millions of dollars with CMOS technologies [Rasmussen et al., 2013]. Significant investments of time and money would be required to fabricate space-qualified versions of commercial ASICs.

ASICs created with state-of-the-art commercial processes have been at least two generations ahead of space-qualified ASICs created with radiation-hardened (rad-hard) processes. Alternatives to creating space-grade ASICs with cost and time intensive rad-hard processes include (1) applying CMOS hardness-by-design approaches (*e.g.* guard banding around MOS transistors or using redundant latches) to custom ASICs created in commercial foundries and (2) testing or qualifying commercially-made ASICs against space mission radiation requirements. The latter option of using commercial ASICs has been recently approached based on increasing demand for higher system performance with the continuously evolving commercial processes [Lacoe, 2000]. With the small satellite revolution, and even for larger satellites, there has been a shift over the past decade toward evaluating, qualifying, and using commercial components for space applications [Sinclair and Dyer, 2013].

In order for a commercial ASIC to be used for a space mission, space systems engineers typically require the device to undergo extensive qualification tests for survivability and reliability in the space environment, including exposure to ionizing radiation. Spacecraft mission parameters, such as orbit and duration, as well as spacecraft materials and geometry play a role in the radiation environment and total ionizing dose (TID) that spacecraft components will encounter. Non-rad-hard, commercial components must be tested for survival at the TID requirements of the mission as well as tested for exposure to high energy protons and heavy ion particles. Radiation damage from high-energy protons and energetic proton events in the space environment can have detrimental effects on microelectronics, such as increased noise in photonics and single event effects (SEEs) [Petersen, 2011; Hiemtra & Blackmore, 2003]. The purpose of this thesis is not focused on describing in detail the effects of radiation on materials and devices in spacecraft applications. There is literature that can provide further detail on this topic [Hastings and Garrett, 2004; Petersen, 2011; Stark, 2011].

The lowest lead time and cost option for applying current optical coherent DSP ASICs to a space-based system would be to test them to specific space-mission radiation requirements. Optical coherent DSP ASICs are used in commercial optical transceiver packages. In 2007, an Agile Engine DSP ASIC was implemented in an optical coherent dual polarization (DP) quadrature phase shift key (QPDK) receiver. The coherent system demonstrated real-time, continuous measurements of 40 Gbps optical signal transmission [Sun et al., 2008; Roberts et al., 2009]. This laboratory demonstration was a key milestone in the development of coherent optical communications systems using DSP ASICs, and the Agile Engine DSP ASIC was one of the first known optical coherent DSP ASICs commercially designed and successfully demonstrated [Kikuchi, 2010]. Acacia Communications, Inc. (Acacia) developed the first industry product line of 100 Gbps coherent optical transceivers with DSP ASICs for analog-to-digital conversion and soft-decision (SD) FEC. With long-haul system experiments over 1000 km, Acacia demonstrated the robustness of their 120 Gbps coherent, polarization-multiplexed (PM) QPSK optical transceiver package [Nelson, 2012].

The Inphi CFP2-ACO coherent optical transceiver module was designed with a polarization-multiplexed quadrature (PMQ) modulator transmitter, an integrated coherent receiver (ICR), and a DSP ASIC (CL20010A1). The Inphi CFP2-ACO coherent optical module with ASIC CL20010A1 was tested over long-haul distances of 7000 km and 1600 km to demonstrate transmission with 100 Gbps and 200 Gbps rates [Reis, 2016]. This work will focus on the Inphi CL20010A1 since this commercial optical coherent DSP ASIC has the highest achievable data rate out of all current commercially available coherent optical communications DSP ASICs.

1.3 Thesis Structure

Studies on space radiation testing and qualification of commercial optical coherent DSP ASICs, such as those mentioned in Section 1.2, have not yet been published and current work on radiation testing of these types of ASICs is unknown. This work investigates if a commercially-available, optical coherent DSP ASIC, specifically the Inphi CL20010A1, can meet LEO space mission radiation requirements.

In Chapter 2, the space radiation environment for sample LEO missions are modeled and analyzed using radiation environment modeling software, Outil de Modélisation de l'Environnement Radiatif Externe (OMERE) (English Translation: Modeling Tool for Space Radiation Environment) version 5.0, created by TRAD Tests and Radiation in Toulouse, France. Models of the sample LEO missions are used to generate dose depth curves and determine TID requirements for testing the CL20010A1 ASIC. The three sample LEO missions included ISS orbit, 800 km polar orbit, and 1000 km 0° inclination orbit, for 1-year, 5-year, and 10-year mission durations. Chapter 2 also discusses background of the LEO radiation environment and describes the radiation environment modeling for each of the sample LEO missions.

The Inphi CL20010A1 ASIC and the CL20010A1 ASIC evaluation board system (CL20010A1-EVK) for experimental testing are described in Chapter 3. Potential radiation damage to the CL20010A1 ASIC in a LEO space environment is also discussed.

Chapter 4 discusses simulations with the nuclear modeling program, Stopping Range In Matter (SRIM). SRIM analyses are used to simulate protons penetrating the CL20010A1-EVK and to evaluate the minimum proton energy level to reach the CL20010A1 silicon active region.

Two proton radiation test campaigns are completed to assess the TID effects and SEEs from ionizing proton radiation on the CL20010A1. A description of the test campaigns is in Chapter 5. Proton SEE cross section results from the test campaigns are used to calculate the SEE rate of the CL20010A1 for the three sample LEO missions. The SEE rate calculation is detailed in Chapter 6.

Radiation mitigation strategies for the CL20010A1 are determined for potential application to a LEO space mission in Chapter 7. Finally, the CL20010A1 is assessed for a LEO space mission, based on the initial radiation requirements from the sample LEO missions modeled and the results of the investigation. Figure 1.2 outlines the investigative approach, which is used to evaluate the performance of the CL20010A1 ASIC for a LEO space radiation environment.

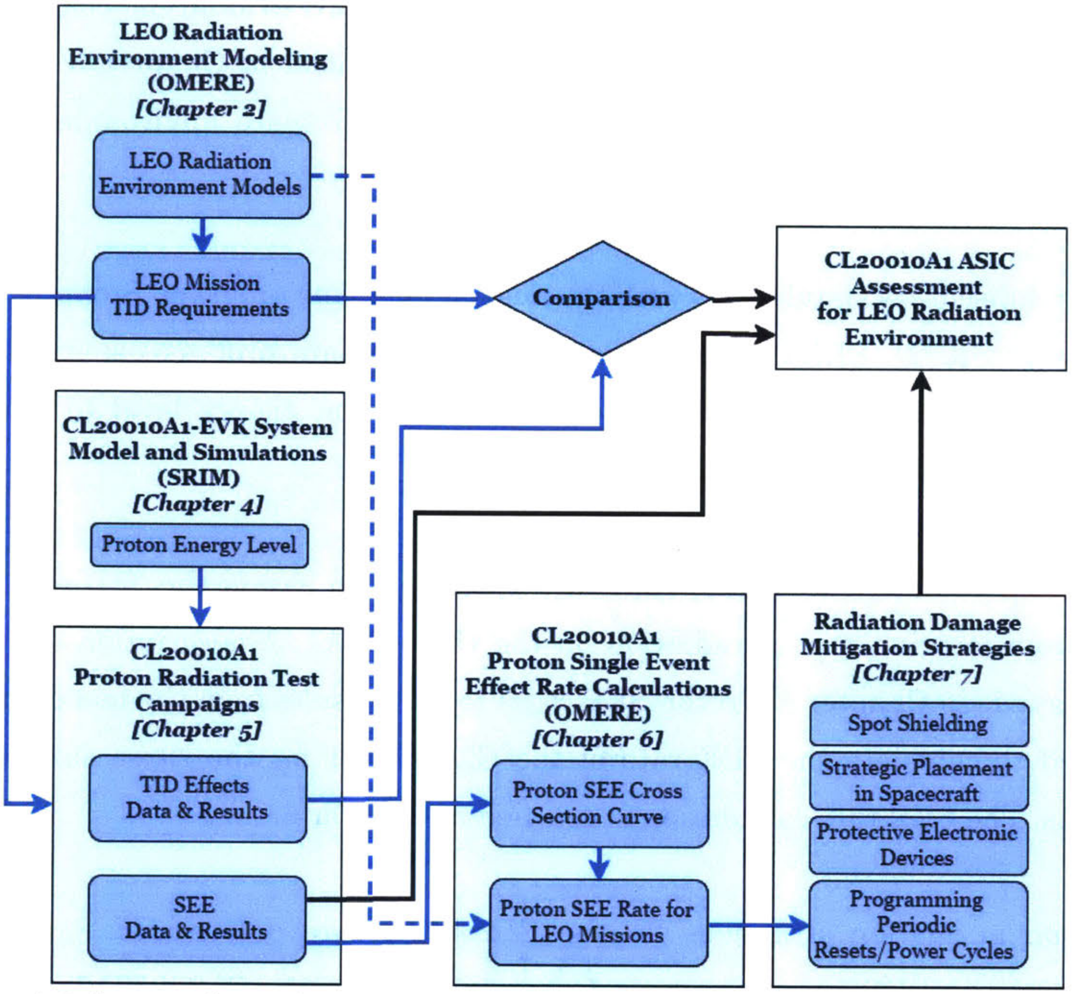

Figure 1.2 Approach used in this work to evaluate the CL20010A1 ASIC for LEO space radiation environment

Overall, the results of this work can be used to evaluate if the commercial Inphi CL20010A1 optical coherent DSP ASIC can be feasibly implemented for a LEO space application. This work is a key step toward the widespread implementation of high data rate, coherent optical communications systems on satellites.

Chapter 2

Low Earth Orbit Space Radiation Environment

This chapter introduces the LEO radiation environment, discusses the radiation sources and effects that are relevant to the focus of this thesis to DSP ASICs, and models the radiation environment of LEO missions to create a set of TID requirements. Figure 2.1 shows the high level approach used in this work, based on the detailed approach in Figure 1.2, and highlights the relevant contributions from this Chapter toward assessing the CL20010A1 ASIC for application in the LEO radiation environment.

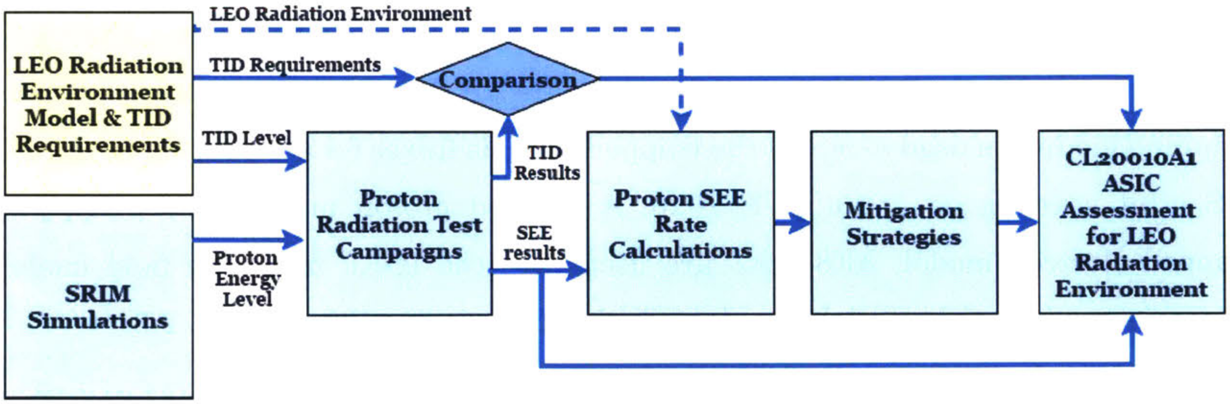

Figure 2.1 High-level approach used in this work to evaluate the CL20010A1 ASIC for LEO space radiation environment with Chapter 2 accomplishments highlighted in yellow.

2.1 Low Earth Orbit Radiation Environment

The radiation environment for LEO space missions consists primarily of trapped particles in the inner Van Allen Radiation Belt, galactic cosmic rays (GCRs), and solar energetic particles (SEPs) that penetrate into the Earth's magnetosphere [Badhwar, 1997].

2.1.1 Trapped Particles in the Inner Radiation Belt

The inner belt has a typical altitude range of 1000 km to 6000 km [Ganushkina et al., 2010]. Within the inner belt, charged particles from GCRs and solar winds are trapped in the Earth's magnetic field and follow the magnetic field lines. Energetic trapped protons dominate the inner belt and reach energy levels from 10 kilo-electron-volts (keV) to 300 Mega-electron-volts (MeV) [Suparta, 2014]. Trapped electrons reach energy levels from 10 keV to 5 MeV [Stassinopoulous, 1988] in the inner belt. For LEO, trapped particles dominate at low inclination orbits with high altitude. Trapped proton fluxes in the inner belt are anti-correlated to solar activity [Suparta, 2014, Varotsou, 2017].

Models of 1 MeV trapped protons and 1 MeV trapped electrons within the Van Allen radiation belts are shown in Figure 2.1 and Figure 2.2, respectively. The greatest concentration of high energy trapped particles are in the region between the inner and outer radiation belts in Figure 2.2 and Figure 2.3. The OMERE (version 5.0) flux mapping module is used to model the trapped particle fluxes for a 1-year mission with ISS orbit starting on January 1, 2020. A trapped proton model, AP8-MIN, and trapped electron model, AE8-MAX are used with the IGRF magnetic field model. These trapped particle models are described in further detail in Section 2.3.

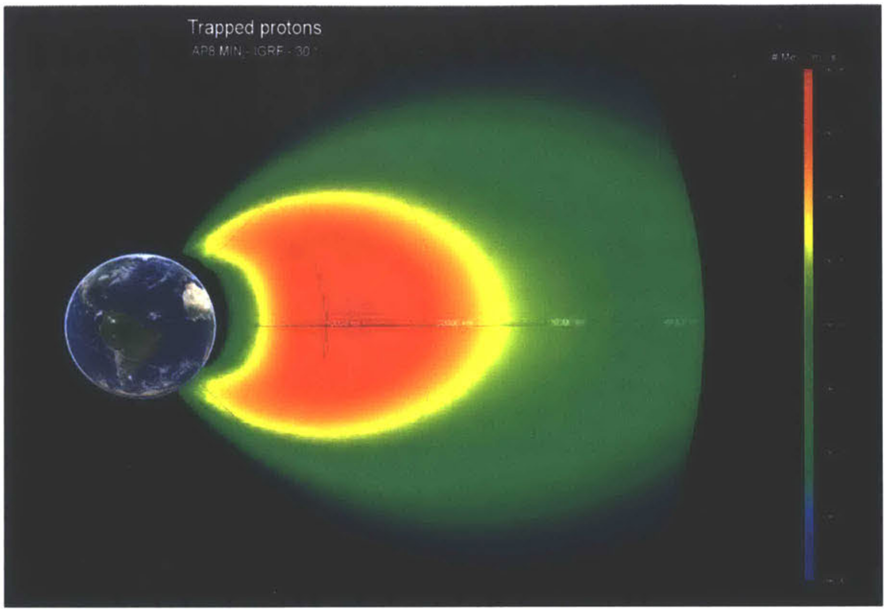

Figure 2.2 Integral flux mapping for 1 MeV trapped protons. The OMERE flux mapping module is used to model trapped protons with AP8-MIN and IGRF for Earth's Magnetic Field. Red represents trapped protons with highest fluxes between ~1 x 10^6 and ~1 x 10^7 particles/cm^2/s, yellow represents fluxes between ~5 x 10^4 and ~1 x 10^6 particles/cm^2/s, and green represents fluxes between ~1 x 10^2 and ~5 x 10^4 particles/cm^2/s.

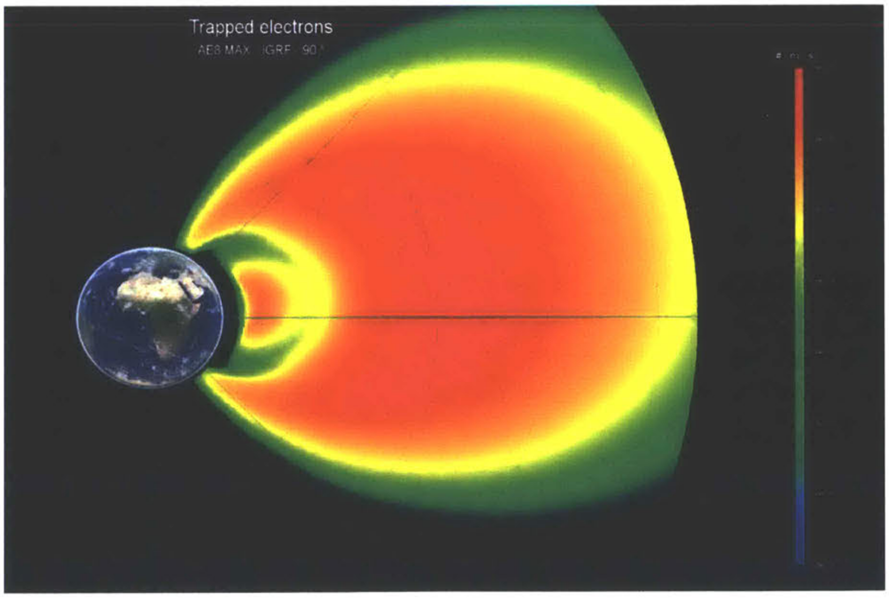

Figure 2.3 Integral flux mapping for 1 MeV trapped electrons. The OMERE flux mapping module is used to model trapped protons with AE8-MAX and IGRF for

Earth's magnetic field. Red represents trapped protons with the highest fluxes between ~1 x 10^6 and ~1 x 10^7 particles/cm^2/s, yellow-orange represents fluxes between ~5 x 10^4 and ~1 x 10^6 particles/cm^2/s, and green represents fluxes between ~1 x 10^2 and ~5 x 10^4 particles/cm^2/s.

The South Atlantic Anomaly (SAA) is a region with increased energetic particle fluxes [Stark, 2011]. Highly energetic protons in the SAA can affect spacecraft at orbital altitudes of up to ~1000 km and orbital inclinations of 35-60 degrees [Lohmeyer, 2015]. The SAA is caused by an offset between the Earth's magnetic field axis and Earth's rotational axis by angle of ~ 11 degrees and by an additional Northward offset of ~ 500 km [Varotsou, 2017; ESA, 2008; Stark, 2011]. The SAA is generally located in the region to the southeast of Brazil, but the geomagnetic field is dynamic and influences the geographic location of the SAA [Heynderickx, 2002].

The OMERE flux mapping module is used in Figure 2.4 to show the SAA for the trapped proton environment of the 1-year mission with ISS orbit starting on January 1, 2020. Figure 2.4 shows the SAA at 400 km altitude with a concentration of high energy trapped protons near the region southeast of Brazil.

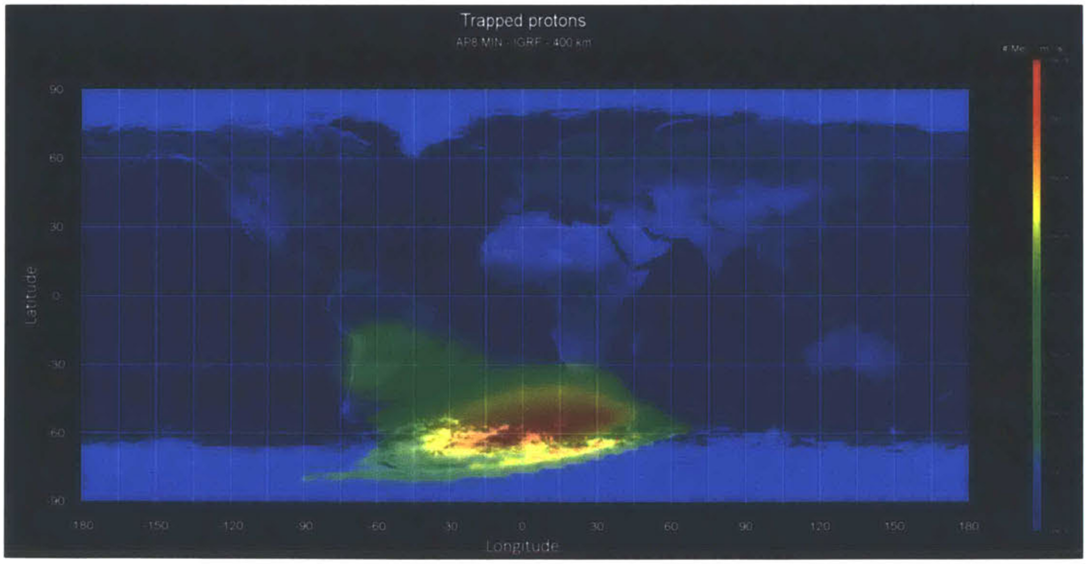

Figure 2.4 OMERE model of trapped protons. Concentration of high energy protons near the region southeast of Brazil highlights the South Atlantic Anomaly. Red represents trapped protons with the highest fluxes between ~1 x 10^7 and ~1 x 10^8 particles/cm^2/s, yellow-orange represents fluxes between ~5 x 10^4 and ~1 x 10^7 particles/cm^2/s, and green represents fluxes between ~1 x 10^2 and ~5 x 10^4 particles/cm^2/s.

2.1.2 Galactic Cosmic Rays

GCRs originate from outside the solar system and are formed from diffusive shock acceleration of supernova remnants. GCRs detected within our solar system reach energy levels of ~ 1 GeV [Suparta, 2014]. A spacecraft in ISS orbit can encounter proton energy range greater than 1 GeV and up to ~10 GeV with fluences of ~10^{-2} particles/m^2·sec [Hastings and Garrett, 1996]. Ions from GCRs can reach energy levels up to ~300 MeV per nucleon and tend to have lower fluxes but higher energy levels [Varotsou, 2017]. Primary GCRs consist of protons, alpha particles, and heavy nuclei. Secondary GCRs consist of neutrons, pions, positrons, and muons, and are a result of primary GCR decay by interaction with Earth's atmosphere. GCRs are anti-correlated with the solar cycle, reaching a maximum during solar minimum, and can be deterred by solar wind, which is strongest during solar maximum. GCR particles move perpendicular to the Earth's magnetic field lines and can be deflected at the equator, and funneled toward the poles. Thus, for LEO spacecraft, GCRs are most relevant at high altitude and high inclination, polar orbits [Suparta, 2014].

2.1.3 Solar Energetic Particles

SEPs consist of electrons, protons, and heavy ions from solar flares and coronal mass ejections (CMEs). The Earth's magnetosphere helps to shield spacecraft from solar particles, especially ions and electrons, but high-energy protons may not be deterred by the magnetosphere. This yields a greater amount of solar protons in comparison to electrons and heavy ions, and these solar protons dominate among the SEPs due to the high energy level. Solar particle events (SPEs) are solar flares and CMEs, which yield protons with energies greater than 30 MeV with flux up to 10^7 cm^{-2} and protons with energies greater than 10 MeV with higher fluxes of up to 10^{10} cm^{-2} [Suparta, 2014]. Solar energetic protons have energy levels that can range from a few keV up to 500 MeV, while solar energetic ions have energy levels that can range from 1 to 100 MeV per nucleon [Varotsou, 2017]. SPEs are correlated with the solar cycle and tend to occur during solar maximum. Solar particles are a significant source of radiation for high altitude and high inclination Earth orbits, since high energy protons tend to penetrate the magnetosphere in these regions [Suparta, 2009].

2.1.4 Summary of Low Earth Orbit Radiation Environment

LEO spacecraft are affected by trapped protons and trapped electrons in the inner belt, protons and ions from SEPs, and protons and ions from GCRs. Table 2.1 below summarizes the types of particles from each LEO radiation environment source, the particle energy levels in LEO, and the relevant areas in LEO that are affected by each type of particle.

Table 2.1 Summary of LEO radiation sources, particles from radiation sources, particle energy level in LEO, and affects areas in LEO

Radiation Source	Particle Type	Particle Energy Level in LEO	Affected Areas in LEO
Inner Belt	Protons	10 keV – 300 MeV	SAA and high inclinations
	Electrons	10 keV – 5 MeV	SAA and high inclinations
GCR	Protons	< ~ 1 GeV	High inclinations
	Ions	< ~ 300 MeV/n	High inclinations
SEP	Protons	keV – 500 MeV	High altitudes and low inclinations
	Ions	1 – 100 MeV/n	High altitude and low inclinations

Particles from the space radiation environment generate TID effects, total non-ionizing dose (TNID) or displacement damage (DD) effects, and SEEs. Figure 2.5 outlines the main LEO radiation environment sources, the types of particles from each source, and the radiation effects caused by the particles. The radiation effects caused by the particles of each LEO radiation source are further described in Section 2.2.

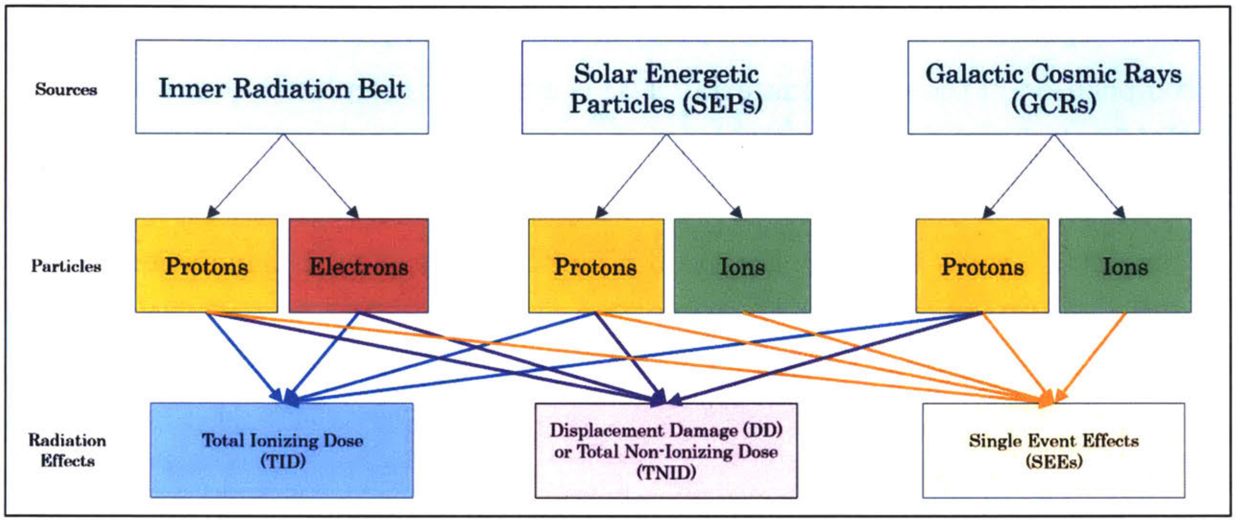

Figure 2.5 LEO radiation environment sources, types of particles from each source, and radiation effects caused by each type of particle

2.2 Low Earth Orbit Radiation Environment Effects on Spacecraft Components

The three main radiation effects in the LEO space environment are TID effects, TNID or DD effects, and SEEs. TID and TNID are cumulative radiation effects based on long-term exposure to a large number of charged particles penetrating into an electrical device. Thus, TID and TNID are related to mission duration and result in progressive degradation. SEEs are non-cumulative and are the result of a single charge particle penetrating into device material and causing functional disruption or failure in the electrical device [McMorrow et al., 2004].

2.2.1 Total Ionizing Dose Effects

Trapped protons and electrons from the radiation belts, protons from SPEs, and protons from GCRs are sources of TID effects on spacecraft electronics [Varotsou, 2017]. TID effects occur when charged particles deposit ionizing energy into target material and the ionization alters the material by generating electron-hole pairs and inelastic Coulombic scattering [Alig and Bloom, 1975; Miroshnichenko, 2003].

TID level depends on the type and energy of the incident particle(s) and the density and composition of the target material. TID is generally calculated as the amount of total energy deposited by all incident particles in the target material divided by the total mass of the incident particles. TID is expressed in units of Joules per kilogram, Gray, or rad (1 Gray = 100 rad). Equation 2.1 outlines the general calculation for TID.

$$TID = \frac{Energy\ Deposited}{Mass} \left[\frac{J}{kg} = Gray = 100\ rad\right] \text{(Equation 2.1)}$$

TID can be described with the ionizing stopping power or linear energy transfer (LET) of a single particle. As a proton or electron penetrates an electronic device, energy is transferred from the particle to the device material and the particle slows down. Electrons within the device material act as a viscous medium to slow down particles and cause ionizing energy loss. LET is a function of the ionizing energy loss by path length of a particle and normalized by the target density [McMorrow et al., 2004]. LET is expressed in units of MeV cm^2 per μm. Equation 2.2 displays the expression for LET.

$$LET = \left(\frac{1}{\rho}\right) \cdot \left(\frac{dE}{dx}\right)_{ionizing} \left[\frac{MeV \cdot cm^2}{\mu m}\right] \text{(Equation 2.2)}$$

The LET and the fluence of incident particles are multiplied to calculate TID. Equation 2.3 shows the relationship between TID and LET with fluence of incident particles.

$$TID = \Phi \cdot \text{LET (Equation 2.3)}$$

TID effects in electronic devices result from charge trapping in insulators, such as gate oxides, and semiconductor/insulator interfaces. TID effects are observed as electrical device parameters drift [Tuite, 2013]. Trapped particles in the inner belt can cause interference with sensors and degradation of spacecraft electronic parts from accumulated TID [Stark, 2011; Suparta, 2009].

Technologies sensitive to TID effects include MOS (Metal Oxide Semiconductor) transistors, field effect transistors (FETs), linear integrated circuits (ICs), and bipolar junction transistors (BJTs). TID effects can cause a shift in the threshold voltage of NMOS devices and a decrease in the drive current of PMOS devices. For CMOS devices, TID effects can result in decreased switching speed and increased leakage current. The effects of ionizing radiation on CMOS devices are further detailed in Chapter 3.2. In junction gate FETs or JFETs, TID effects include enhanced source-drain leakage currents. TID effects on BJTs include degradation to the gain current for low current conditions [Poizat, 2009].

Common spacecraft electronic devices with MOS, FET, IC, and BJT technologies include charged-coupled devices (CCDs), optical components, micro-electro-mechanical systems (MEMS), memory chips, bipolar electronic devices, and general microelectronics. The most sensitive devices to TID failures are bipolar electronic devices. CCDs and optical components can experience increased dark current. Charge build-up in the dielectric layers of MEMS from TID can lead to a shift in response. Memory devices, such as static random access memory (SRAM) chips are also sensitive to TID failures due to CMOS, BJT, and FET technologies within the chips [Sukhaseum, 2017]. Potential TID damage on digital microelectronics includes enhanced transistor leakage and logic failures due to reduced gain in BJTs or shifted threshold voltages and reduced switching speeds in CMOS. TID effects can cause gain degradation and change the offset voltage, offset current, and bias-current of analog microelectronics [Poizat, 2009].

TID sensitivity of an electronic device is dependent on the technology passivation, device structure, and when and where the device was manufactured. Different foundries manufacture electrical devices with different doping levels that produce cause dose sensitivity levels. Although manufacturing quality of semi-conductor regions is controlled based on doping levels, there are differences in the manufacturing quality of the oxide layer among different foundries or even among different manufacturing lots of the same foundry [Dodd et al., 2010].

2.2.2 Total Non-Ionizing Dose or Displacement Damage Effects

Trapped protons and electrons from the radiation belts, protons from SPEs, and protons from GCRs cause DD or TNID effects on spacecraft electronics [Varotsou, 2017]. TNID effects are caused by incident particles entering the target material and interacting with nuclei. When an incident particle hits a nucleus, the nucleus can become displaced in the crystal lattice, causing elastic scattering and nuclear reactions. Displacement damage results from the cumulative physical degradation of the lattice material [Miroshnichenko, 2003].

TNID can be described by the nuclear stopping power or non-ionizing energy loss (NIEL) of a particle penetrating the target material and transferring energy to the nucleus. NIEL is a function of the nuclear energy loss by path length unit of a particle and normalized by the target density. NIEL is expressed in units of MeV cm^2 per μm. Equation 2.4 shows the expression for NIEL.

$$NIEL = \left(\frac{1}{\rho}\right) \cdot \left(\frac{dE}{dx}\right)_{nuclear} \left[\frac{MeV \cdot cm^2}{\mu m}\right] \text{ (Equation 2.4)}$$

The NIEL and the fluence of incident particles are multiplied to calculate TNID. Equation 2.5 shows the relationship between TNID and NIEL with fluence of incident particles. TNID is expressed in units of Joules per kilogram, Gray, or rad.

$$TNID = \Phi \cdot NIEL \text{ (Equation 2.5)}$$

The TNID level or the amount of DD at a sensitive region of the device is calculated for a specific mission based on the radiation environment. TNID effects cause stable defects, which behave as recombination centers, trap centers, and diffusion centers. Recombination centers impact the carrier lifetime, trap centers impact resistivity of electronic circuits, and diffusion centers impact mobility of electrons and holes. The following types of devices are sensitive to displacement damage effects and are listed in order of most sensitive: opto-electronics, bipolar ICs, MOS transistors, power MOSFETs, and CMOS. The most sensitive devices are minority carrier devices [Sukhaseum, 2017].

2.2.3 Single Event Effects

Protons and heavy ions from both GCRs and solar flares as well as trapped protons in the inner radiation belt cause SEEs in electronic devices on LEO spacecraft [Varotsou, 2017]. The greatest potential hazard from GCRs for LEO spacecraft are SEEs, caused primarily by abundant deposition of iron nuclei [Suparta, 2009]. Energetic heavy ions from GCRs can deposit significant amounts of energy in spacecraft electronics, and large amount of kinetic energy from GCRs can have permanent, damaging effects on materials through which the particles may pass [ESA, 2008; Stark, 2011]. Heavy ions from GCRs and energetic protons can trigger latch up by producing charge in the well-substrate junction of electronic devices. In some LEO environments, trapped protons can have greater energy levels (such as in the SAA) than GCR heavy ions and may induce more SEEs [Petersen, 1996].

SEEs occur when a charged particle is deposited or passed through active components with electrical circuits, such as memory, power, and logic devices. Specifically, SEE radiation damage is caused when a charged, high-energy particle, commonly a proton, impacts the energy structure and lattice structure of a semiconductor material in an electronic device. The charged particle transmits energy to the semi-conductor material and can cause a displacement of a lattice atom in the material. Local ionization occurs within the material from the generated charge along the ion path and an impulsive release of charge from the ionization process causes a SEE [Stark, 2011]. Within microelectronic devices, SEEs result from energetic protons interacting with silicon nuclei and producing ionizing nuclear recoils [Hiemstra, 2003]. SEEs cause a disruption in electronic device operation and can have either destructive or non-destructive consequences to devices.

2.2.3.1 Types of Single Event Effects

SEEs can be destructive or non-destructive to spacecraft components. Figure 2.6 outlines the types of SEEs based on destructive and non-destructive effects.

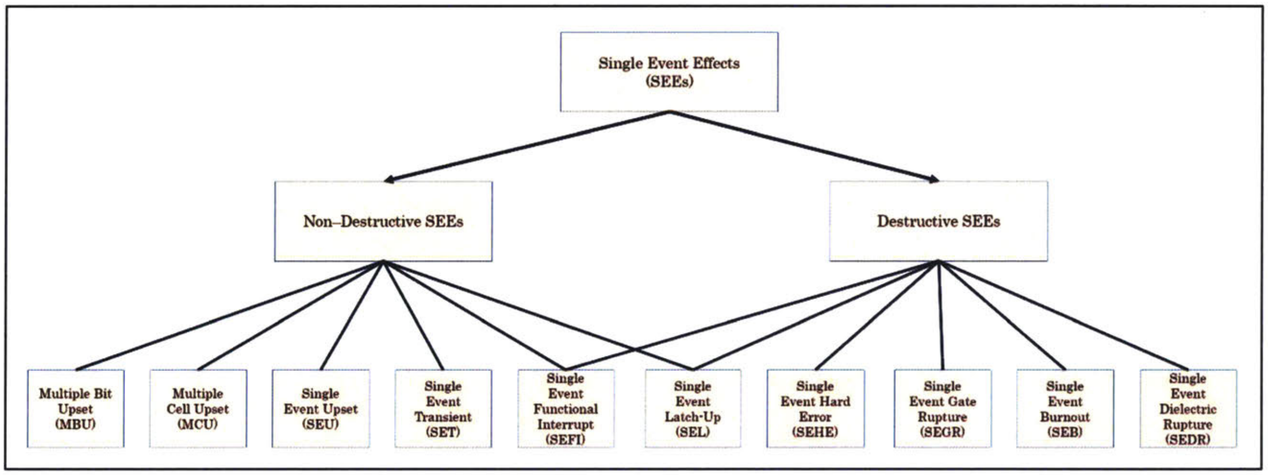

Figure 2.6 Non-destructive and destructive SEE

SEEs are particular to certain electronics and components, based on the structure or technology. Table 2.2 lists the types of SEEs as well as some devices and technologies that are susceptible to each type of SEE. The types of SEEs relevant to the

CL20010A1 ASIC, which is a CMOS device, are highlighted and indicated in Table 2.2 and include single event upsets (SEUs), single event functional interrupts (SEFIs), multiple bit upsets (MBUs), multiple cell upsets (MCUs), single event latch-ups (SELs), and single event hard errors (SEHEs) [Mutuel, 2016]. The non-relevant types of SEEs to the CL20010A1, such as single event transients (SETs), single event gate ruptures (SEGRs), single event burn-outs (SEBs), and single event dielectric rupture (SEDR), are further discussed in Section A.1 of the appendix.

Table 2.2. Types of SEEs and susceptible devices and technologies. SEEs relevant to CL20010A1 ASIC indicated (*).

Single Event Effect	**Susceptible Devices and Technologies**	**Destructive?**
Single Event Upset (SEU)*	Digital devices, analog devices, CMOS devices, microprocessors, FPGAs, ASICs, memories, buffers, latches, converters, and optical components	Non-Destructive
Single Event Functional Interrupt (SEFI)*	Memories, microprocessors, state controllers, FPGAs, ASICs, ADCs, DACs	Non-Destructive
Single Event Transient (SET)	Memories, Analog devices, linear devices, power devices, converters	Non-Destructive
Multiple Bit Upset (MBU)*	Memories, microprocessors, FPGAs, latches, ASICs	Non-Destructive
Multiple Cell Upset (MCU)*	Memories, microprocessors, FPGAs, latches, ASICs	Non-Destructive
Single Event Latch-Up (SEL)*	CMOS devices	Destructive
Single Event Hard Error (SEHE)*	Memories, latches, microprocessors,	Destructive

	FPGAs, ASICs, buffer devices	
Single Event Gate Rupture (SEGR)	Power MOSFETs, converters	Destructive
Single Event Burn-out (SEB)	N-channel power MOSFETs, converters, analog devices	Destructive
Single Event Dielectric Rupture (SEDR)	FPGAs, programmable ICs, linear devices, Power MOSFETs	Destructive

Non-destructive SEEs relevant to the CL20010A1 include SEUs, SEFIs, MBUs, MCUs, [Samaras, 2014; Mutuel, 2016]. SEUs are one of the most common SEEs for spacecraft electronics. SEUs occur in digital, analog, and optical components, and device areas sensitive to SEUs include memories, buffers, and latches. SEUs change the logic state of a circuit in an electronic device and induce soft errors [Baker, 2002]. Within MOS devices, Off NMOS and PMOS drain transistors are sensitive to SEUs [McMorrow, 2004]. A reset or rewrite of the device logic after an SEU occurrence can typically restore normal operation of the device.

SEFIs are characterized by a loss of normal device operation and are identified by device functional "hangs" in which the device falls into an unknown or unmanaged state. SEFIs can also result in permanent damage to a device. To counteract a SEFI, devices must be reset or power cycled to recover normal operation. SEFIs occur in complex devices with built-in state or control sections such as field programmable gate arrays (FPGAs), ASICs, dynamic random-access memory (DRAM), ADCs, and digital-to-analog converters (DACs) [Normand, 2004; Samaras, 2014].

Both MBUs and MCUs occur when a single particle triggers several bit flips, typically within memory devices. A MBU induces the corruption of several bits in the same memory word or address [Normand, 2004]. A MCU triggers several upsets or transients as it penetrates through a device or system.

Destructive SEEs relevant to the CL20010A1 include SEHEs and SELs [Samaras, 2014; Mutuel, 2016]. SEHEs result from a SEU causing permanent change to the state of a memory element or buffer. SELs have an induced high current state, which can result in the loss of device functionality or potentially permanent damage. SELs are short-circuits between the ground and supply voltage and occur in CMOS and BiCMOS technologies. A power reset can be used to return to normal operation after occurrence of an SEL, but this type of SEE can also be destructive [Samaras, 2014].

2.2.3.2 Single Event Effect Rate

SEE device sensitivity is characterized by the probability of an SEE occurrence or the device cross section. The device cross section is determined based on specific conditions, such as the type of device, particle, and SEE. The SEE cross section of a device at a given particle energy level is the ratio of the total number of events from SEEs to the particle fluence, expressed in units of cm^2. Equation 2.6 shows the calculation for SEE cross section of a device.

$$\sigma = \frac{Total\ Number\ of\ Events}{Particle\ Fluence}\ [cm^2]\ \text{(Equation 2.6)}$$

For ions, the device cross section is defined by the LET of heavy ions. There is a critical LET level or the LET threshold, over which a particle will induce a SEE [Hastings and Garrett, 1996]. For protons, the device cross section is defined by the energy level transported. Data points for the device cross section at specific LET or energy levels are collected from radiation testing with protons or heavy ions. These data points are used to generate a Weibull distribution and a cross section curve fitted to the test data. The Weibull distribution is the typical distribution used to parametrize SEE cross section data since it levels to a limiting value [Petersen et al., 1992]. The Weibull distribution provides better empirical description of cross section data in comparison to other distributions, such as Bendel 2-parameter fits [Tylka et al., 1996]. The cross section curve is then used to calculate the SEE rate for a device

[Samaras, 2014]. This process is used to calculated the proton SEE rate for the CL20010A1 ASIC in Chapter 6. SEE data for the calculations are collected from proton radiation test campaigns described in Chapter 5.

The software program, OMERE, calculates the ion SEE rate for one sensitive volume within a device at all LET values and integrates over the ion SEE cross section curve. OMERE uses the Cosmic Ray Effect on Electronics (CREME) model by Adams [1986] to generate a CREME rate. The CREME model assumes a rectangular parallelepiped sensitive volume, constant LET along the ion path, and a critical charge of the sensitive volume. The CREME rate at each LET is generated by modeling charged ions through a volume and defines that an event occurs if the charge of a penetrating ion is greater than the critical charge of the sensitive volume. The product of the CREME rate at each LET and the LET threshold distribution is integrated over the device cross section curve to generate the device SEE rate [Samaras, 2014]. Equation 2.7 shows the calculation for the device SEE rate with the parameters as the CREME rate, *T*, and the LET threshold distribution, ζ, as functions of LET, *L*.

$$\tau = \int_{L0}^{\infty} T(L) \cdot \zeta(L)\, dL \; [\frac{Number\ SEEs}{Unit\ Time}] \text{ (Equation 2.7)}$$

The process for calculating the ion SEE rate will be completed in future work with heavy ion test campaigns, as described in Section 8.2.2.

The proton cross section curve from the Weibull distribution fit is expressed as a function of the incident energy. The proton SEE rate is calculated by integrating the product of the cross section and proton flux at each energy level [Samaras, 2014]. Equation 2.8 displays the calculation for the proton SEE rate with parameters of proton cross section, Σ, and the proton flux, φ, as functions of proton energy, *E*.

$$\tau = \int_{E0}^{\infty} \varphi(E) \cdot \Sigma(E)\, dE \; [\frac{Number\ SEEs}{Unit\ Time}] \text{ (Equation 2.8)}$$

The OMERE SEE rate calculation module uses Equation 2.7 and Equation 2.8 to determine the expected ion and proton SEE rates, respectively, of a device for a given mission. Prior to SEE rate calculations, the mission radiation environment must be modeled to determine input parameters to the equations, such as LET threshold distribution and proton flux. The proton SEE rate calculation for the CL20010A1 is based on sample LEO missions modeled in Section 3.3.

For a device and spacecraft mission, the SEE rate is calculated to gain an understanding of the device sensitivity to SEEs and to determine how often the device should be power cycled or reset in order to restore nominal operation from SEE occurrences.

2.2.4 Summary of Low Earth Orbit Radiation Effects on Spacecraft Devices

The mission orbit determines the types of radiation effects that the spacecraft and components could encounter, while the mission duration and timeline determine the potential amount of cumulative dose or rate of single events. Each type of radiation effect is characterized to generate mission radiation requirements. Table 2.3 summarizes the types of radiation effects in a LEO environment based on the types of particles inducing each effect, examples of susceptible devices and technologies, and characterization of each type of radiation effect.

Table 2.3 Summary of radiation effects, types of particles inducing each effect, susceptible devices and technologies to radiation effects, and characterization of radiation effects

Radiation Effect	Types of Particles Inducing Effect	Susceptible Devices and Technologies	Characterization
TID	Protons Electrons	CCDs, optical devices, MEMs, memory devices, MOS transistors, FETs, linear ICs, BJTs, microelectronics	Fluence, LET

TNID or DD	Protons Electrons	Opto-electronic devices, bipolar ICs, MOS transistors, FETs	Fluence, NIEL
SEE	Protons Ions	Memories, microelectronics, ASICs, FPGAs, programmable ICs, CMOS devices, MOSFET devices	SEE Cross Section, LET, Transported Energy

2.3 OMERE Radiation Environment Analyses for Sample Low Earth Orbit Missions

Radiation analyses are conducted to evaluate the radiation environment for sample LEO missions. The web interface and space radiation environment simulation, OMERE version 5.0 is used to calculate the expected TID levels for the sample missions. TID radiation requirements based on the OMERE analyses are used to evaluate the radiation tolerance level of the commercial ASIC.

The three LEO space missions with different orbital parameters are modeled, (1) ISS Orbit (400.2 km perigee, 409.5 km apogee, 51.64 inclination), (2) 800 km altitude polar orbit, and (3) 1000 km altitude, 0° inclination orbit, with OMERE for mission durations of 1 year, 5 years, and 10 years with an arbitrary mission start date of January 1, 2020. Table 2.4 summarizes the LEO space missions modeled.

Table 2.4 LEO space missions modeled with OMERE

LEO Mission	Orbit Altitude	Orbit Inclination	Orbit Type
1	(ISS) 400.2 km perigee, 409.5 km apogee	51.64°	Circular
2	800 km	Polar	Circular
3	1000 km	0°	Circular

OMERE simulates the radiation environment for each mission based on models for trapped proton and electron fluxes, solar particle fluxes, and GCRs. Trapped proton fluxes are modeled using the European standard trapped proton model AP8-MIN and trapped electron model AE8-MAX, which were both created by NASA. The AP8-MIN model includes proton energy levels from 0.1 MeV to 400 MeV and represents the worst cases trapped proton fluxes, which occur during solar minimum. The AE8-MAX model includes electron energy levels from 0.04 MeV to 7 MeV and represents the worst case trapped electron fluxes, which occur during solar maximum. AP8-MIN is used to model all missions except for GEO and MEO. OMERE uses the data from both AP8-MIN and AE8-MAX models to calculate the mean flux for trapped particles by calculating the flux spectrum at each orbit point and taking the average of the flux spectrum [Varotsou, 2017].

The fluxes and fluences from solar ions and protons are calculated with OMERE solar particle modules: *Average Statistical Models* and *Solar Flare Models.* Cumulated solar particle effects are calculated with *Average Statistical Models.* The mean solar proton fluxes and fluences for each mission are calculated with the ESP model for a 99% confidence level. The ESP model is an ECSS 10-04 standard for solar proton fluences and covers energy levels ranging from 1 MeV to 300 MeV. The mean solar ion fluxes and fluences for each mission are calculated with the PSYCHIC solar ion model for a 99% confidence level. Peak ion and proton fluxes during solar flares for single event rates are calculated using *Solar Flare Models.* Proton solar events for each mission are modeled using the ONERA model for the worst case 5-minute proton fluxes at each energy level. Heavy ion solar events for each mission are modeled using the CRÈME 96 model for elements He to U. CRÈME 96 is the ECSS 10-04 standard for heavy ion solar event fluxes [Varotsou, 2017].

GCRs are modeled with the OMERE *Cosmic Ray* module. The GCR ISO 15390 model is used to calculate the proton and heavy ion fluxes from cosmic rays for each mission. The GCR ISO 15390 is the standard model for cosmic rays. The 1996.4 Solar Minimum temporal configuration is used with the model, since this represents a worst case scenario for GCRs.

TID is quantified using dose model SHIELDOSE-2, with shielding configuration set as center of aluminum spheres and target material set as silicon. For a given orbit, SHIELDOSE-2 determines the absorbed dose behind a range of aluminum shielding thicknesses on different detector materials from user-input electron and proton fluences [Seltzer, 1980; Seltzer, 1994]. SHIELDOSE-2 quantifies total ionizing dose based on calculations of electrons, bremsstrahlung photons, and protons in the radiation environment of a given orbit. On-orbit dose rates generated by SHIELDOSE-2 are generally consistent with dose rates less than or equal to 10 mrad/s specified in the Enhanced Low Dose Rate Sensitivity (ELDRS) radiation test procedure in MIL-STD-883H [Bogorad et al., 2010; Lohmeyer, 2015].

Figure 2.7, Figure 2.8, and Figure 2.9 display the dose depth curves for various aluminum shielding thicknesses estimated with the SHIELDOSE-2 model for the chosen orbits and mission durations of 1-year (a), 5-years (b), and 10 years (c). A comparison of the TID curves for the 3 different mission durations is shown in Figure 2.7(d), Figure 2.8(d), and Figure 2.9(d). The dose depth curves display TID contributions from trapped electrons, trapped protons, solar protons, and gamma photons, as indicated with the different colored curves defined in the legend. For a space mission, the dose depth curve is used to define the top-level dose requirement assuming a conservative shielding thickness, typically 100 mils (2.54 mm) of aluminum shielding [Poivey and Day, 2002]. The TID values at 100 mils aluminum shielding thickness are marked on the TID curves in the figures.

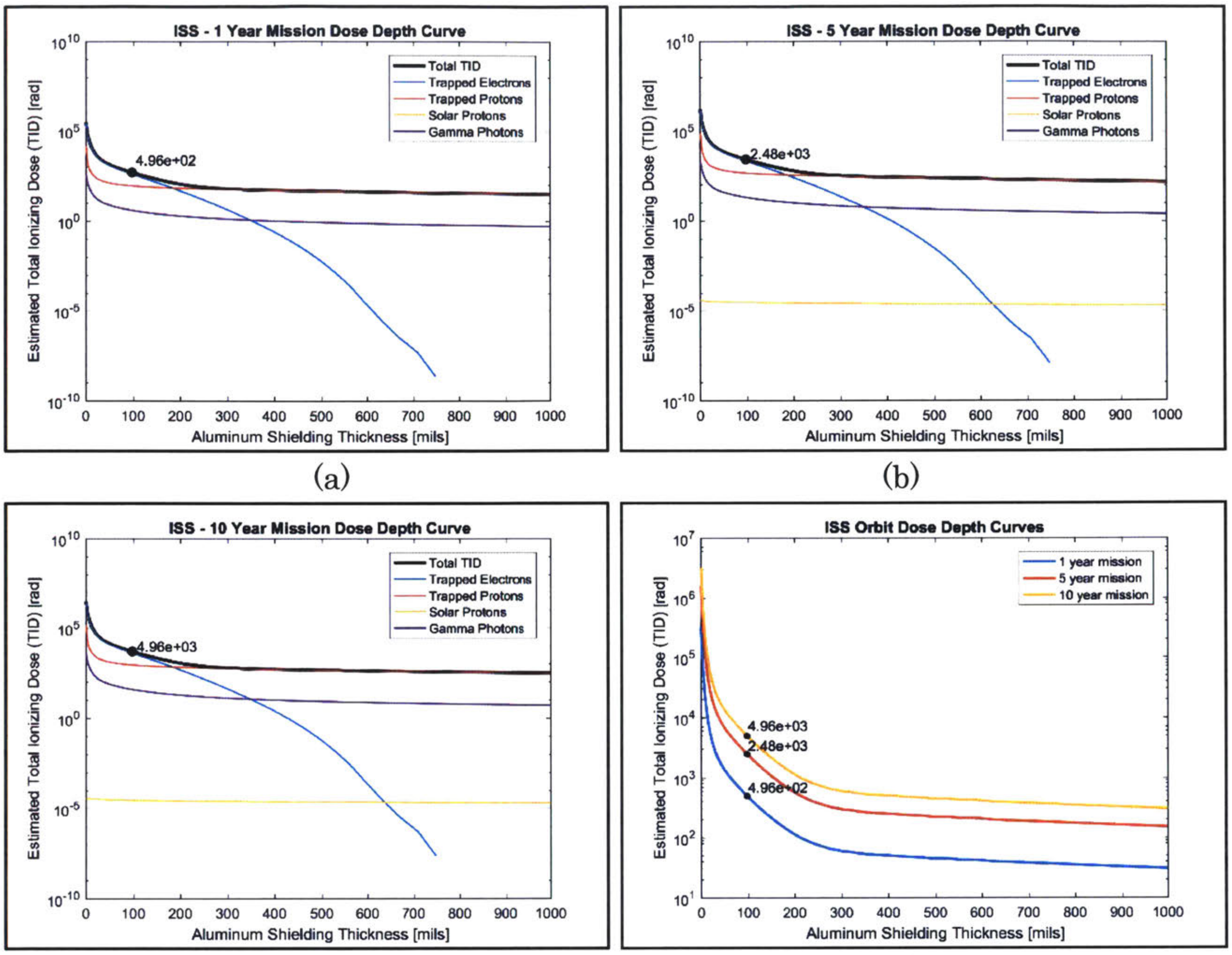

(a)

(b)

(c)

(d)

Figure 2.7 (a,b,c,d). Dose depth curves for LEO Mission at ISS Orbit for (a 1-year, (b) 5-year, and (c) 10-year (bottom left) mission durations, showing TID and contributions from trapped particles, bremsstrahlung protons, and solar protons. Estimated TID comparison for all three mission durations (d). The TID values at 100 mils aluminum shielding thickness are marked and labeled.

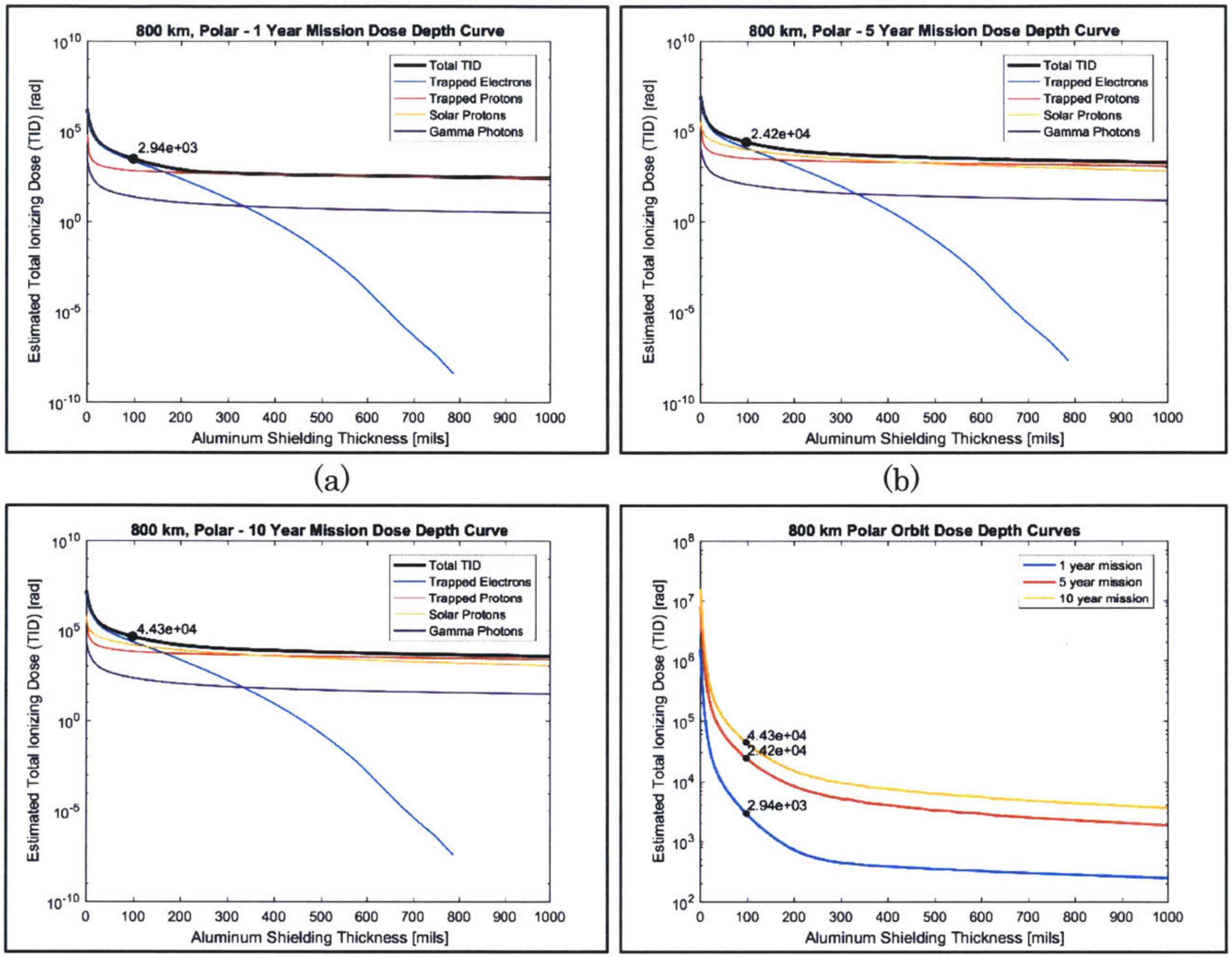

(a) (b)

(c) (d)

Figure 2.8 (a,b,c,d). Dose depth curves for LEO Mission at 800 km polar orbit for 1-year (a), 5-year (b), and 10-year (c) mission durations, showing TID and contributions from trapped particles, bremsstrahlung protons, and solar protons. Estimated TID comparison for all three mission durations (d). The TID values at 100 mils aluminum shielding thickness are marked and labeled.

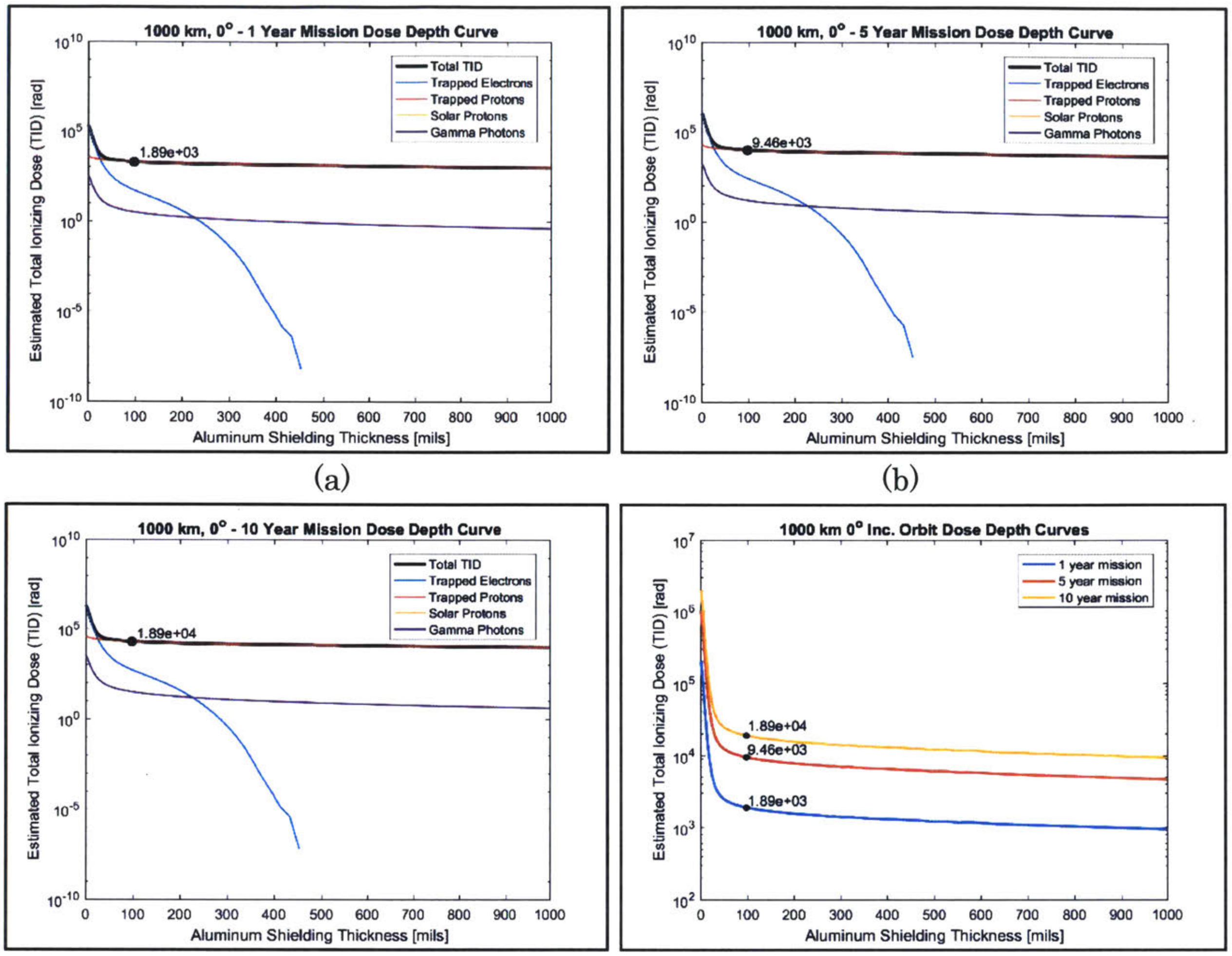

(a) (b)

(c) (d)

Figure 2.9 (a,b,c,d). Dose depth curves for LEO Mission at 1000 km, 0° inclination orbit for 1-year (a), 5-year (b), and 10-year (c) mission durations, showing TID and contributions from trapped particles, bremsstrahlung protons, and solar protons. Estimated TID comparison for all three mission durations (d). The TID values at 100 mils aluminum shielding thickness are marked and labeled.

As displayed in the TID curves in Figure 2.7, Figure 2.8, and Figure 2.9, the magnitude of TID decreases as aluminum shielding thickness increases. For a given aluminum shielding thickness and orbit inclination, accumulated TID steeply increases as LEO altitude increases, and for a given aluminum shielding thickness and altitude, TID increases as LEO inclination increases [Lohmeyer, 2015]. For a given aluminum shielding thickness, LEO altitude, and inclination, the TID increases as mission duration increases.

Table 2.5 lists the TID values at 100 mils aluminum shielding thickness for each orbit and mission duration, based on the dose depth curves.

Table 2.5 Estimated total ionizing dose levels for sample LEO missions, calculated from OMERE radiation environment simulation.

Total Ionizing Dose for 100 mils (2.54 mm) Aluminum Shielding Thickness			
Orbit	1-Year Mission	5-Year Mission	10-Year Mission
ISS	0.50 krad	2.48 krad	4.96 krad
1000 km, 0° Inc.	1.89 krad	9.46 krad	18.9 krad
800 km, Polar	2.94 krad	24.2 krad	44.3 krad

With the selected dose requirement, a general guideline is to use a factor of two margin on the expected TID of the mission for qualifying and testing spacecraft components [Lohmeyer, 2015]. Table 2.6 defines top-level dose requirements for the sample LEO missions with a factor of two margin from the estimated TID in Table 2.5. These TID requirement values will be used to assess if the CL20010A1 ASIC is suitable for use in LEO missions.

Table 2.6 Total Ionizing Dose Requirements for sample LEO missions based on 100 mils aluminum shielding thickness and factor of 2 margin.

Total Ionizing Dose Requirement with 2x Margin for 100 mils (2.54 mm) Aluminum Shielding Thickness			
Orbit	1-Year Mission	5-Year Mission	10-Year Mission
ISS	1.0 krad	4.96 krad	9.92 krad
1000 km, 0° Inc.	3.78 krad	18.92 krad	37.8 krad
800 km, Polar	5.88 krad	48.4 krad	88.6 krad

Chapter 3

CL20010A1 Optical Coherent DSP ASIC

3.1 CL20010A1 ASIC Description

The Inphi CL20010A1 is the device-under-test (DUT) investigated for this work. The CL20010A1 is an optical coherent DSP ASIC modem. The ASIC is a monolithic, 28-nm CMOS modem, which supports transmission and detection of 100 Gbps and 200 Gbps information rates with polarization-multiplexed differential and non-differential QPSK and 16 quadrature amplitude modulated (QAM) signals. The CL20010A1 handles host and line framing/de-framing, SD-FEC encoding/decoding and high-speed (~60 GSPS) analog input and output [Inphi, 2014]. In addition, the receive channel performs high-speed DSP functions comprising polarization rotation, carrier phase recovery, and optical fiber dispersion compensation.

3.1.1 CL20010A1 ASIC Functionality

The CL20010A1 ASIC can benefit coherent optical transceiver systems through its integrated transmitter, Tx DAC, framer, and digital algorithms. An integrated transmitter removes the need for a separate Tx multiplexer. A Tx DAC supports spectral shaping for tight wavelength packing. The framer enables optical lane alignment, detection, and automatic correction for phase rotation, and polarization reversal without external support. The digital algorithms programmed in the ASIC provide consistent performance and eliminate the need for optical dispersion compensation with losses and associated amplification [Inphi, 2014].

The CL20010A1 ASIC interfaces between a host system and optical hardware or components (line side). Figure 3.1 below displays the high-level data path model through the ASIC. In the Tx host-to-optics path or "egress" path, Tx data from the host is input to the ASIC for DSP, framing, and FEC processing. The Tx processed data from the ASIC is then output to optical transmitter components, such as an optical modulator, laser, etc. For the receive (Rx) optics-to-host path or "ingress" path, Rx data from optical receiver components, such as a coherent receiver, are input to the ASIC. The Rx processed data from the ASIC is then sent to the host system [Inphi, 2014].

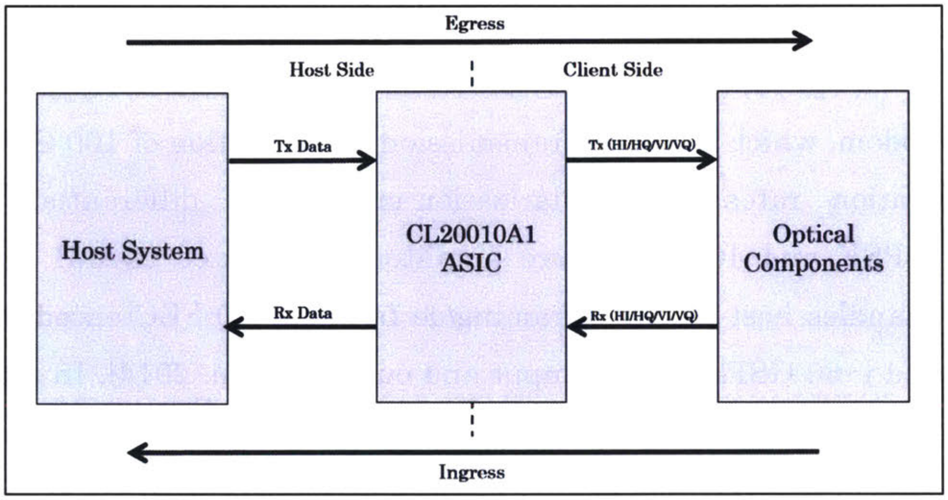

Figure 3.1 Egress and ingress data paths for CL20010A1 ASIC as interface between host system and optical components [Inphi, 2014].

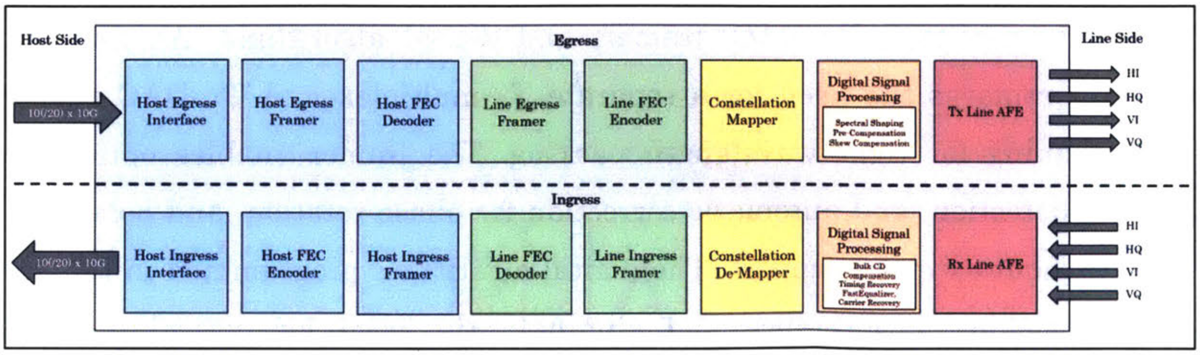

Figure 3.2 Data Path through CL20010A1 ASIC [Inphi, 2014].

The detailed data path through the ASIC is modeled in Figure 3.2. For the egress data flow, Tx data initially enters host analog front end (AFE) circuitry, where clock and data are recovered for individual lanes, and signal interfaces, which align the signal to support client rate modes. The lane signals are then multiplexed and sent to the egress host framer and host FEC decoder. Tx data is forwarded to the egress line framer and line FEC encoder. Tx data then undergoes constellation mapping and Tx DSP with spectral shaping, pre-compensation, and skew compensation. The processed, digital Tx data is converted into four analog signal lanes (HI, HQ, VI, VQ) by DACs within AFE circuitry.

The ingress data flow is complementary to the egress data flow. Line side data is received at the line AFE circuitry and sampled by an ADC. DSP of the Rx signal includes bulk chromatic dispersion (BCD) equalization and timing recovery, impairment equalization, such polarization mode dispersion (PMD) and polarization dispersion loss (PDL), and carrier recovery. The 4 lanes (HI, HQ, VI, VQ), are de-skewed and the constellation de-mapper is used to de-map the symbols. The ingress data is then sent to the line ingress framer and line FEC decoder, followed by the host ingress framer and FEC encoder. The data is de-multiplexed and is processed through the host ingress interface to support host protocols.

3.1.2 CL20010A1 ASIC Evaluation Board System

The CL20010A1 was integrated on a custom-developed, coherent optical transceiver evaluation board (EVK). Due to high power consumption (~50W) of the CL20010A1, a large copper heat sink with a dedicated fan was integrated onto the EVK above the ASIC. For a space application, an alternative thermal design would need to be created to manage the CL20010A1 heat dissipation. This work does not focus on evaluating the entire CL20010A1-EVK system for a space application. Rather, the purpose of this work is to assess the performance of the CL20010A1 based on potential radiation effects from the LEO environment.

An optical transceiver, the Finisar FTLC3321x3NL Compact Form Pluggable 2 Analog Coherent Optics (CFP2-ACO) transceiver module was also integrated onto the EVK to serve as the transmit and receive optical line side. An external power supply provides +3.3V to the CFP2-ACO.

The EVK comprises of a printed circuit board (PCB), FPGA, and Ethernet interface. Ethernet connection between a computer and the EVK allows for a graphical user interface (GUI) to control the CL20010A1 and the EVK. An external power supply provides +12.0 V to the EVK. Figure 3.3 shows the block diagram of the integrated system with the CL20010A1, external heat sink, and optical transceiver on the EVK, connected to a computer/GUI and power supplies. Figure 3.4 shows the test setup of the CL20010A1-EVK system connected to a computer/GUI and power supplies

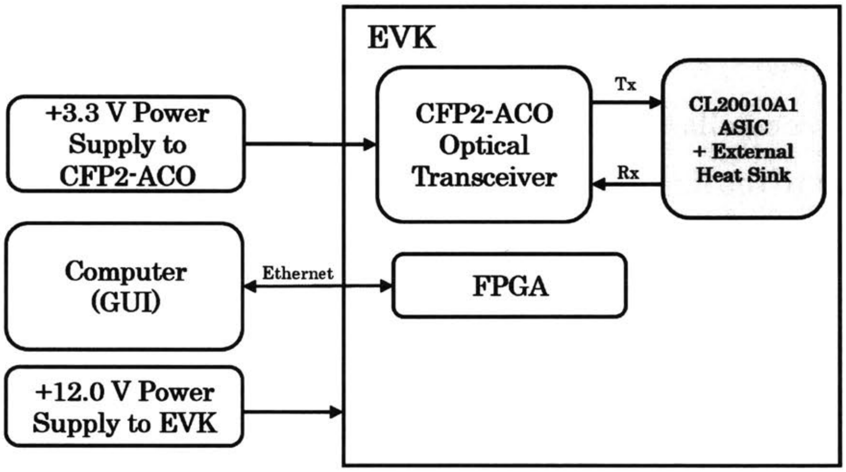

Figure 3.3 CL20010A1 ASIC integrated on EVK with optical transceiver. Computer and power supply connected to EVK.

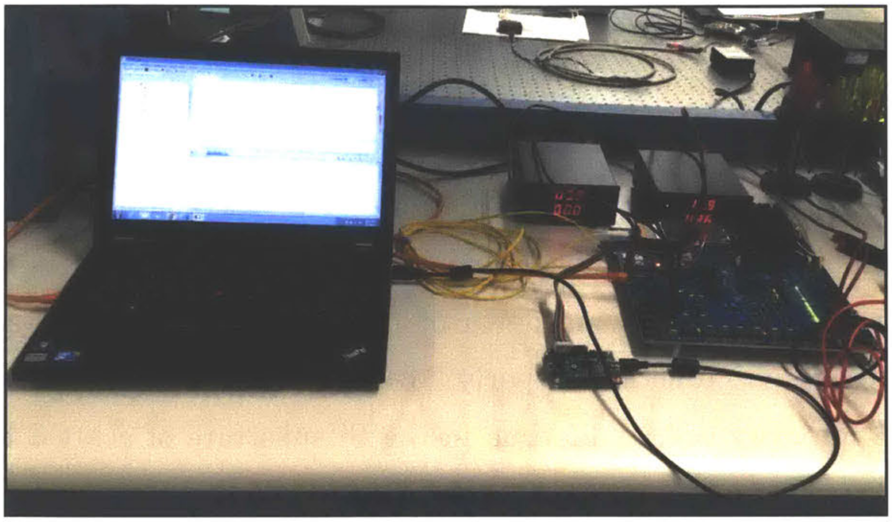

Figure 3.4 Test setup of CL20010Al-EVK system. CL20010A1-EVK connected to computer and power supplies.

Detailed modeling of the PCB and CL20010Al layers are discussed in Chapter 4 for SRIM simulations. The EVK system and CFP2-ACO optical transceiver have components potentially susceptible to radiation damage, such as the FPGA, direct current to direct current (DC-DC) converters, ADCs, DACs, and point of loads (POLs). Consideration was taken to decouple the effects of radiation on the EVK and CFP2-ACO components versus on the CL20010A1 from the test campaigns (Chapter 5). The diameter and geometry of the proton beams used in the radiation test campaigns were controlled so that only the CL20010A1 was directly irradiated. The EVK was also designed with strategic placement of all radiation-sensitive commercial components sufficiently far away from CL20010A1 in case there was slight scattering of protons from the center of the beam.

3.2 Potential Radiation Damage to the CL20010A1 ASIC in a LEO Space Environment

As a CMOS device with silicon active region, the CL20010A1 ASIC is susceptible to both ionizing and non-ionizing radiation damage. Ionizing radiation damage to MOS devices can occur from TID effects and SEEs, and non-ionizing radiation damage can occur from TNID or DD effects.

MOS devices exposed to ionizing radiation have degradation in performance parameters and changes to electrical characteristics, such as shifts in threshold voltage, decrease in gain, slowing down of integrated circuits, increased leakage currents, and ceasing to function properly [Ma and Dressendorfer, 1989]. DD causes a reduction in minority carrier lifetime in the Si substrate of a MOS device. Most MOS devices, however, are not significantly affected by minority carrier lifetime [Ma and Dressendorfer, 1989]. The main concerns for the CL20010A1 are ionizing radiation damage from TID effects and SEEs. As mentioned in Section 2.2.3 and highlighted in Table 2.2, the types of SEEs relevant to the CL20010A1 ASIC include single event upsets (SEUs), single event functional interrupts (SEFIs), multiple bit upsets (MBUs), multiple cell upsets (MCUs), single event latch-ups (SELs), and single event hard errors (SEHEs) [Mutuel, 2016].

3.2.1 Ionizing Radiation Damage to CMOS Devices

Ionizing radiation leads to damage because it generates mobile electrons and holes in both the SiO_2 insulator layer and Si substrate in MOS devices. The insulating SiO_2 layers of circuit structures within the ASIC are most susceptible to ionizing radiation damage. Radiation damage to the SiO_2 layer consists of the build-up of trapped charge in the oxide layer, an increase in interface traps, and an increase in bulk oxide traps. Charge and trap sites created by ionizing radiation originate from three different processes: electron-hole pair creation in SiO_2 layer, and bond breaking and atomic relaxation of electron-hole pairs, and electron and hole transport [Srour and McGarrity, 1988; Ma and Dressendorfer, 1989].

Ionizing radiation and internal photoemission from the device contacts can create electrons and holes within the SiO_2 layer. These electrons and holes can recombine within the SiO_2 layer or can be transported through the SiO_2 layer. Electrons are mobile within the SiO_2 layer and move to the contacts. Holes have low mobility and can become trapped in the SiO_2 layer, generating a positive charge. If holes can move to the SiO_2/Si interface and capture electrons, an interface trap is created. The electrons and holes transported from the SiO_2 layer, along with ionizing radiation, can break chemical bonds in the SiO_2 structure. If the broken chemical bonds do not reform from the recombination of electrons and holes, electrically active defects are formed. These defects become interface traps or trap sites for carriers. Broken bonds, specifically from hydrogen or hydroxyl groups, can release impurities which mobilize and migrate to the SiO_2/Si interface, resulting in an interface trap [Ma and Dressendorfer, 1989].

3.2.2 Total Ionizing Dose and Single Event Upset Trends in CMOS Devices

There has been a recent trend toward increased TID hardness levels in CMOS ICs as manufacturers strategically design these technologies to be less susceptible to ionizing radiation effects. CMOS technologies at the 0.13 to 0.25 μm feature size have exhibited TID tolerance for up to 300 krad (SiO_2) [Dodd et al., 2010]. From this, it could be hypothesized that the CL20010A1 should be radiation tolerant to TID levels of the LEO space missions modeled in Section 2.3. Table 2.6 indicates 88.6 krad as the maximum TID requirement for all the modeled LEO space missions based on 100 mils aluminum shielding and factor of 2 margin. However, variation exists between manufacturers of CMOS technologies and even between CMOS devices manufactured in different lots, which could result in different radiation hardness levels [Dodd et al., 2010]. Since there have been no published studies on TID testing of the CL20010A1, it is necessary to test the CL20010A1 ASIC for radiation damage up to TID levels from requirements of the modeled LEO missions.

With improvements to power efficiency, the amount of charge that represents stored information has decreased and results in increased sensitivity of CMOS devices to single-particle charge collection transients. Additionally, there has been increased sensitivity of CMOS devices to SETs as operating speeds have increased [Dodd et al., 2010]. SEUs are the single largest contributor to device soft failure rates in CMOS devices. SELs are a major concern for CMOS devices since this type of SEE can be destructive. Complex devices, such as the CL20010A1, are also susceptible to SEFIs [Samaras, 2014]. It is critical that the CL20010A1 be tested for SEEs.

Proton radiation test campaigns are completed in Chapter 5 to assess effects of TID and SEEs on the CL20010A1. For SEE testing, the CL20010A1-EVK system is powered during proton irradiation to monitor real-time SEE occurrences, the time duration of an SEE occurrence is recorded, and SEEs effects on the system performance are observed, such as losing connection between the CL20010A1 and EVK and receiver loss of lock (LOL). For TID testing, the CL20010A1-EVK system is also powered to monitor ionizing radiation effects on the performance of the CL20010A1 through degradation to bit error rate (BER).

Chapter 4

SRIM Analyses of CL20010A1 ASIC

Proton beam radiation is used to test the CL20010A1 for ionizing radiation damage, specifically TID effects and SEEs. Prior to radiation testing, analyses are conducted to determine the threshold proton energy level required to penetrate through the active silicon region of the CL20010A1. Figure 4.1 highlights the relevant contributions from Chapter 4 in the high-level approach of this work toward assessing the CL20010A1 ASIC for application in the LEO radiation environment.

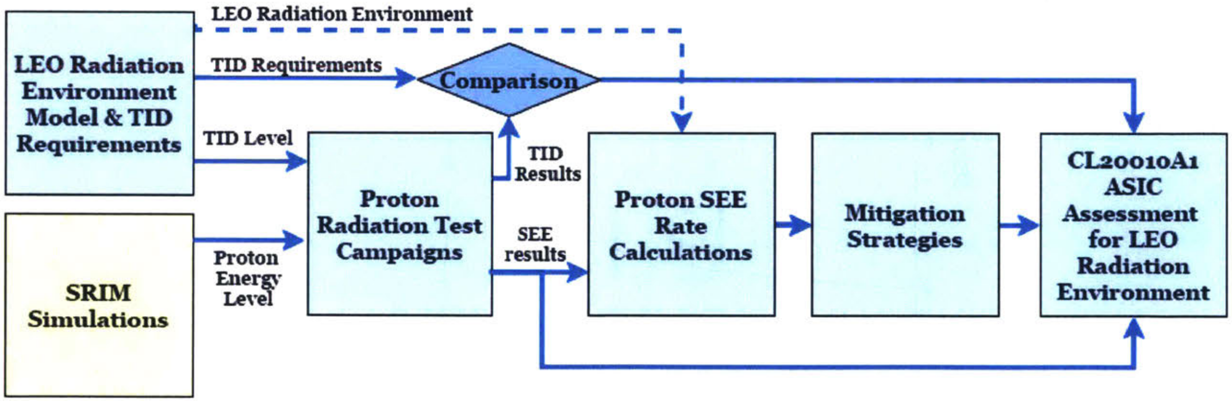

Figure 4.1 High-level approach used in this work to evaluate the CL20010A1 ASIC for LEO space radiation environment with Chapter 4 accomplishments highlighted in yellow.

The external heat sink above the CL20010A1 on the EVK precludes proton beam irradiation from the front side. The most direct path to irradiate the CL20010A1 is through the back side of the 24-layer printed circuit board (PCB). Detailed calculations through all PCB layers, ASIC ball grid array, and other packaging layers were performed to ensure the analysis of energy deposition in the active die was accurate based on the model of the CL20010A1-EVK.

As protons travel through a material, energy is lost due to protons ionizing atoms and depositing dose along the travelled path in the material. The range that the proton penetrates through a material is dependent on the initial energy level and the target material properties, such as density, electronic characteristics, and nuclear characteristics [Buchner et al., 2002]. The maximum range that the proton penetrates through a target material is characterized by the Bragg peak, which is the point of maximum ionizing energy loss for the proton. Figure 4.2 displays the relationship between ionizing energy loss and the range for 64.0 MeV protons in silicon.

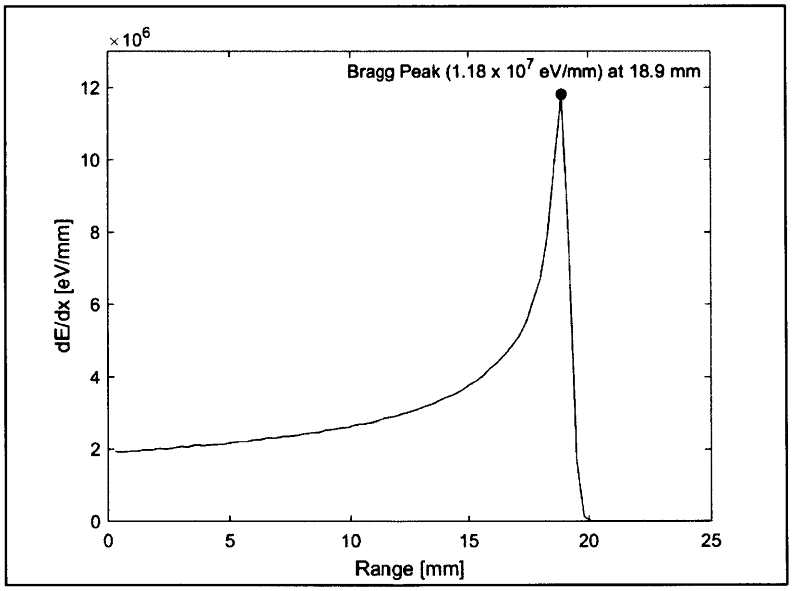

Figure 4.2 Energy loss for 64.0 MeV protons in silicon as a function of distance from material surface. Bragg peak indicated.

The range at which the Bragg peak occurs is calculated for radiation test campaigns when it is desired to evaluate the ionizing radiation effects for protons stopping in the target material. However, this work focuses on evaluating the ionizing radiation effects of protons penetrating completely through the CL20010A1 silicon active region, which is most representative of what the ASIC will experience in a LEO mission for protons with energy levels high enough to penetrate through the CL20010A1-EVK system layers. There is only a small range of energy levels near the Bragg peak energy level for which protons will stop in the active region. Otherwise, protons will either be stopped in the CL20010A1-EVK layers above and below the active region or will completely penetrate the active region and induce ionizing radiation effects.

The CL20010A1-EVK system modeled for the SRIM analyses in this work is not high fidelity due to the lack of proprietary information on material properties of the PCB and packaging material. With an assumed model (further described in Section 4.1), the proton energy level needed for the Bragg peak to occur in the CL20010A1 silicon active region cannot be accurately calculated. The CL20010A1 silicon active region layer is less than 1 mm thick, thus any slight deviations in the calculation could result in protons without sufficient energy to reach the target region. Overall, this work is focused on ensuring that protons have sufficient energy levels to penetrate through the CL20010A1 silicon active region in order to produce ionizing radiation effects.

4.1 CL20010A1-EVK System Modeling

The computer program, SRIM, specifically the Transport of Ions in Matter (TRIM) module, is used to model the CL20010A1 behind the EVK PCB layers and packaging material. TRIM is used to analyze the energy level needed for protons to penetrate through the PCB and packaging layers prior to reaching the CL20010A1 silicon active region. As described in Section 3.1.2, the CL20010A1 was mounted between the EVK and external heat sink. Figure 4.3 shows the model of the integrated EVK system with CL20010A1 and displays the different layer components modeled in TRIM.

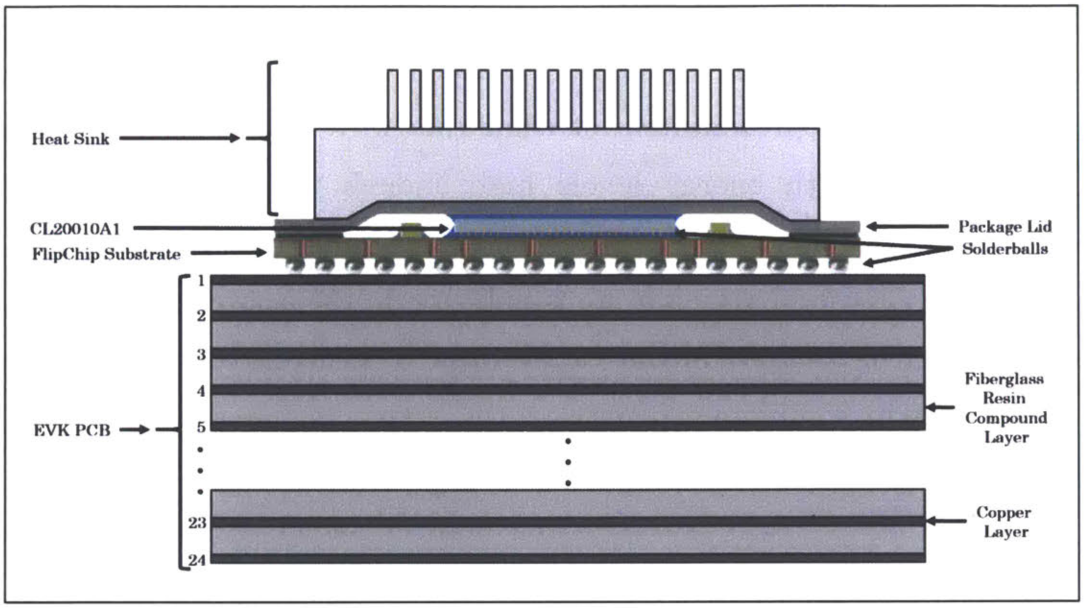

Figure 4.3 Model of CL20010A1 between EVK and Heat Sink

The chemical stoichiometry and material properties of the PCB and flip chip substrate are proprietary information. Because complete information would not be provided by Inphi, the manufacturer of the EVK, we instead approximate chemical compositions and densities of these layers for SRIM modeling.

The EVK PCB consists of 24 layers of copper with inter-layer dielectric (ILD) material between each layer. The ILD is composed of fiber-glass cloth and resin compound, Megtron 6. Megtron 6 Prepreg cloth style 1078 was used to model the EVK PCB ILD. The Megtron 6 Prepreg 1078 compound is a polyphenylene oxide (PPO) blend resin system with 72% resin content [Panasonic, 2016]. Assuming 72% PPO (C_8H_8O) and 28% fiber glass cloth (SiO_2), an effective density of 1.52 g/cm^3 and an effective chemical stoichiometry of $C_{60}H_{60}O_{19}Si_6$ is used as a combination of PPO and fiber glass to model the ILD layers.

The flip chip substrate layer from Phoenix Precision Technology Corporation patent consists of an organic polymer resin, such as bismaleimide trizxine (BT), polyimide (PI), benzocyclobutene (BCB), liquid crystal polymeric (LCP), and polytetrafluoroethylene (PTFE) [Hsu, 2008]. PTFE is used as the material for modeling the flip chip substrate since it had the highest density (2.2 g/cm^3). A higher density material causes higher energy loss for protons travelling through the material and this results in a more conservative TRIM calculation than a lower density material.

The external solder balls are modeled with chemical stoichiometry $Sn_{96.5}Ag_3Cu_{0.5}$ [Topline, 2017]. The CL20010A1 is modeled as a silicon dye. The back end of line (BEOL) components in the CL20010A1, such as transistors, capacitors, etc., are not modeled since these detailed components are small features and the active silicon region is the main region of interest for radiation effects. Each layer is modeled in TRIM based on atomic composition, density, and layer thickness, as detailed in Table 4.1.

Table 4.1 CL20010A1-EVK system layers modeled in TRIM based on atomic composition, density, and layer thickness. Parenthesis in thickness column indicate number of layers. Assumptions are indicated with (*).

Layer	**Atomic Composition**	**Density**	**Thickness** (number of layers)
CL20010A1 ASIC Silicon Die	Si	2.329 g/cm^3	0.775 mm
Solder balls (Internal CL20010A1)	$Sn_{98.5}Ag_{1.5}$*	g/cm^3	0.075 mm
Flip Chip Substrate – PTFE	C_2F_4*	2.200 g/cm^3 *	0.880 mm
Solder balls (External)	$Sn_{96.5}Ag_3Cu_{0.5}$*	7.386 g/cm^3	0.330 mm
PCB Total (All 24 Layers)	--	--	4.454 mm
PCB Individual Copper Layer (x24)	Cu	8.96 g/cm^3	17.78 µm (20) 35.56 µm (4)
PCB Individual ILD Layer (x23)	$C_{60}H_{60}O_{19}Si_6$*	1.520 g/cm^3 *	50.80 µm (5) 104.00 µm (2) 200.66 µm (6) 208.00 µm (9) 312.00 µm (1)

4.2 TRIM Analyses of CL20010A1-EVK System

We simulate five thousand protons (H^+ ions) with 64 MeV energy level penetrating through the modeled layers with TRIM. A proton energy level of 64.0 MeV is set as the baseline for the SRIM analyses since this energy level is one of the typical proton energy levels for radiation test campaigns at UC Davis Crocker Nuclear Laboratory (CNL), with maximum proton beam energy level of 67.5 MeV [Hartman, 2013]. As discussed in Chapter 2 and summarized in Table 2.1, the LEO radiation environment includes trapped protons with energy levels between 10 keV to 300 MeV, solar energetic protons with energy levels up to 500 MeV, and GCR protons with energy levels up to 1 GeV [Varotsou, 2017; Hastings and Garrett, 1996].

TRIM simulations were approached with the intention to conduct proton test campaigns with energy levels that would span the potential LEO environment proton energy range. The high financial costs of proton test campaigns limited this work to conduct only two tests. The SRIM simulations were used to evaluate the lower energy level that could be used for a proton test campaign of the CL20010A1. The lower proton energy level must have sufficient energy to reach the end of the CL20010A1 ASIC active region after travelling through the modeled CL20010A1-EVK system. The higher proton energy level selection was based on the upper edge of the high energy range of solar energetic protons (500 MeV) [Varotsou, 2017].

Within TRIM, the calculation model "Detailed Calculation with Full Damage Cascades" is used. To simulate the proton beam penetrating through the bottom of the EVK, layers are modeled in TRIM in the following order: PCB layers, external solder balls, flip chip substrate, internal CL20010A1 solder balls, and CL20010A1 silicon die.

To address concerns that 100 data points from the ionization data file would not be sufficient for accurately summarizing the ionization energy data for a complex, multilayer system, we use a layer-by-layer comparison approach. Two approaches are used to model the CL20010A1-EVK system with TRIM. In the first approach, the CL20010A1 ASIC-EVK system is modeled with all layers of the PCB, external solder balls, flip chip substrate, internal solder balls, and ASIC silicon die input to TRIM as an integrated system simulation. In the second approach, the system is modeled as individual layers with a simulation for each layer. The results of these approaches are compared to ensure that a proton energy level of 64 MeV would be sufficient to reach the CL20010A1 active area. For both approaches, the calculated ionization energy levels at the end of the CL20010A1 active region are analyzed.

For both approaches, the TRIM ionization data from the file IONIZ.txt is used to calculate the proton energy level through the system or individual layers. The file IONIZ.txt contains 100 data points for each simulation. With only 100 data points representing 51 modeled layers for the full integrated CL20010A1-EVK system, the ionization loss for a particular data point could encompass multiple layers. For example, some PCB ILD layers are tens of micrometers while other layers are hundreds of micrometers. We conduct a layer-by-layer approach for modeling the system to verify the results of the integrated system simulation in case there were any inaccuracies with the first modeling method.

IONIZ.txt contains an array of 3 columns: target depth in units of angstroms, the ionization energy loss from ions per target depth thickness in units of eV per angstrom, and the ionization energy loss from recoils per target depth thickness in units of eV per angstrom. Figure 4.4 below shows a section of the IONIZ.txt TRIM file for the first EVK PCB copper layer in the layer-by-layer TRIM model approach.

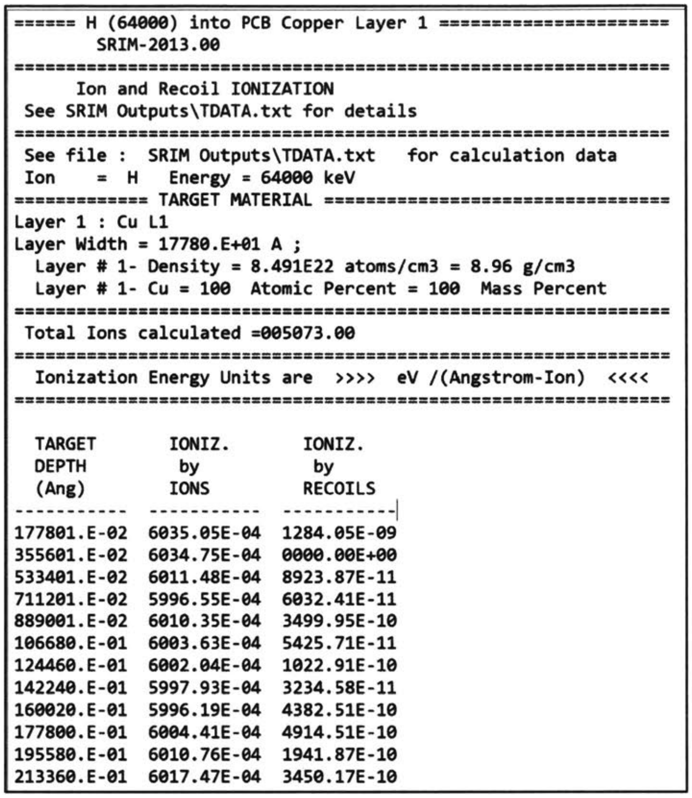

```
====== H (64000) into PCB Copper Layer 1 ======================
        SRIM-2013.00
==============================================================
      Ion and Recoil IONIZATION
 See SRIM Outputs\TDATA.txt for details
==============================================================
 See file :  SRIM Outputs\TDATA.txt   for calculation data
 Ion    =  H   Energy = 64000 keV
============= TARGET MATERIAL ================================
Layer 1 : Cu L1
Layer Width = 17780.E+01 A ;
  Layer # 1- Density = 8.491E22 atoms/cm3 = 8.96 g/cm3
  Layer # 1- Cu = 100  Atomic Percent = 100  Mass Percent
==============================================================
 Total Ions calculated =005073.00
==============================================================
  Ionization Energy Units are  >>>>  eV /(Angstrom-Ion)  <<<<
==============================================================

  TARGET       IONIZ.       IONIZ.
  DEPTH         by           by
  (Ang)        IONS         RECOILS
-----------  -----------  -----------
177801.E-02  6035.05E-04  1284.05E-09
355601.E-02  6034.75E-04  0000.00E+00
533401.E-02  6011.48E-04  8923.87E-11
711201.E-02  5996.55E-04  6032.41E-11
889001.E-02  6010.35E-04  3499.95E-10
106680.E-01  6003.63E-04  5425.71E-11
124460.E-01  6002.04E-04  1022.91E-10
142240.E-01  5997.93E-04  3234.58E-11
160020.E-01  5996.19E-04  4382.51E-10
177800.E-01  6004.41E-04  4914.51E-10
195580.E-01  6010.76E-04  1941.87E-10
213360.E-01  6017.47E-04  3450.17E-10
```

Figure 4.4 TRIM ionization data file "IONIZ.txt" used for calculating energy loss through EVK PCB copper layer.

A Matlab script, ioniz.m, calculates the total ionization energy loss of the protons through the modeled layer or integrated system and is included in Appendix section A.2 Matlab Script for TRIM Simulation Data Analyses. Data from IONIZ.txt was input to the Matlab script. Equation 4.1 calculates the total ionization energy loss by ions (dE) by multiplying the total layer thickness (dx) with the average ionization energy loss per target depth thickness $\left(\frac{dE}{dx}\right)_{avg}$. The average ionization energy loss is calculated by taking the average of the "Ionization by Ions" column of data in the IONIZ.txt file. Ionization energy loss is in units of eV.

$$dE = \left(\frac{dE}{dx}\right)_{avg} \cdot dx \, [\frac{eV}{Ang} \cdot Ang = eV] \text{ (Equation 4.1)}$$

Equation 4.2 calculates the final ionization energy level of the protons (E_F) in the integrated CL20010A1-EVK system approach, by subtracting the total ionization energy loss (dE) from the initial energy level of protons entering the system (E_0) or specific layer (based on which approach was used). In the layer-by-layer approach, Equation 4.3 calculates the ionization energy level of the protons at the end of a layer (E_x) by subtracting the ionization energy loss through that layer (dE_x) from the energy level of the protons penetrating the prior region (E_{x-1}).

$$E_F = (E_0 - dE)\ [eV] \text{ (Equation 4.2)}$$

$$E_x = (E_{x-1} - dE_x)\ [eV] \text{ (Equation 4.3)}$$

4.2.1 Integrated CL20010A1-EVK System TRIM Simulation

For the integrated CL20010A1-EVK system model approach, all layers of the EVK PCB, external solder balls, flip chip substrate, internal solder balls, and CL20010A1 ASIC silicon die are input to TRIM as a single model simulation. Figure 4.5 below displays a block diagram of the integrated system TRIM simulation method.

Figure 4.5 Integrated CL20010A1-EVK System Model TRIM Simulation Method

The average ionization energy loss per target depth thickness is ~0.24 eV/angstrom and the total ionization energy loss through the integrated system is ~15.60 MeV. The ionization energy level of protons penetrating into the CL200101A1 ASIC silicon region is ~50.22 MeV, and the final ionization energy level of protons at the end of the ASIC active region is ~48.40 MeV. Table 4.2 summarizes the results of integrated system TRIM simulation for 64.0 MeV protons penetrating through the modeled CL200101A1-EVK system.

Table 4.2 TRIM simulation results for CL20010A1-EVK integrated system model.

Average Ionization Energy Loss Per Target Depth Thickness	0.24 eV/angstrom
Total Ionization Loss Through System	15.60 MeV
Ionization Energy Level Penetrating into CL20010A1 Active Region	50.22 MeV
Final Ionization Energy Level at end of CL20010A1 Active Region	48.40 MeV
Ionization Energy Loss in CL20010A1 Active Region	1.82 MeV

Figure 4.6 shows the TRIM simulation of five thousand protons penetrating completely through the integrated system model. The integrated system simulation method verifies that protons with 64.0 MeV energy level would be sufficient to penetrate the CL20010A1 active region. With a final ionization energy level of 48.40 MeV at the end of the CL20010A1 active region, there is more than 40 MeV of margin for 64.0 MeV protons to penetrate through the end of the active region. This amount of margin is more than sufficient to account for deviations from the actual total ionization energy loss through the system.

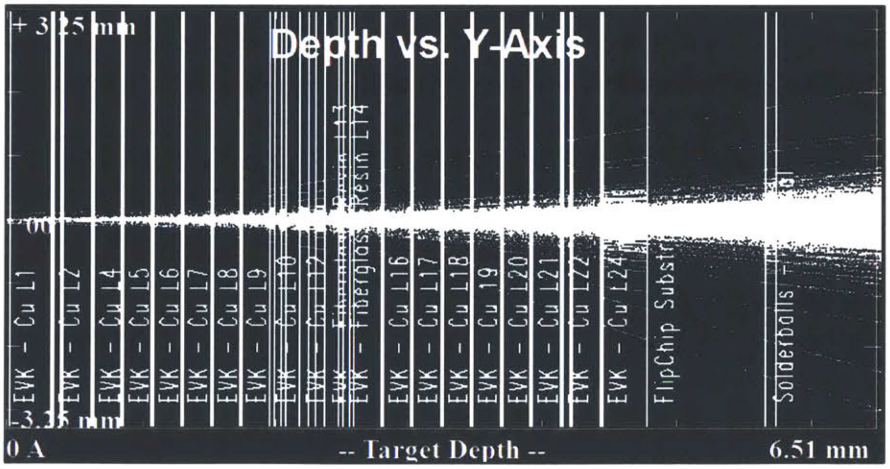

Figure 4.6 Integrated system TRIM simulation of five thousand 64.0 MeV protons penetrating through CL20010A1-EVK system.

4.2.1.1 Worst-Case Integrated System TRIM Simulation

We also conduct an integrated CL20010A1-EVK system TRIM simulation for the worst-case scenario of protons travelling through a path of copper-filled vias within the EVK PCB. The EVK PCB is modeled as an individual layer of copper. The following layers of external solder balls, flip chip substrate, internal solder balls, and CL20010A1 silicon die are modeled as previously described.

The “worst-case” integrated system TRIM simulation method calculates an ionization energy level of ~23.30 MeV entering the CL20010A1 ASIC silicon active region and an ionization energy level of ~19.87 MeV for protons penetrating through the end of the ASIC silicon active region. Table 4.3 summarizes the results of the “worst-case” integrated system TRIM simulation.

Table 4.3 TRIM simulation results for CL20010A1-EVK integrated system model worst-case scenario.

Average Ionization Energy Loss Per Target Depth Thickness	0.68 eV/angstrom
Total Ionization Loss Through System	44.13 MeV
Ionization Energy Level Penetrating into CL20010A1 Active Region	23.30 MeV
Final Ionization Energy Level at end of CL20010A1 Active Region	19.87 MeV
Ionization Energy Loss in CL20010A1 Active Region	3.43 MeV

Figure 4.7 shows the TRIM simulation of five thousand 64.0 MeV protons penetrating completely through the PCB layers, modeled as copper, and through the CL200101A1 ASIC silicon active region (last layer to the right side of Figure 4.6). Even in this

worst-case scenario, protons with 64.0 MeV energy can still penetrate through the copper-filled vias in the PCB to reach the CL20010A1 active region. With a final ionization energy level of 19.87 MeV at the end of the CL20010A1 active region, there is more than 10 MeV margin for 64.0 MeV protons to penetrate through the end of the active region if the TRIM simulations slightly deviate from the actual total ionization energy loss through the system.

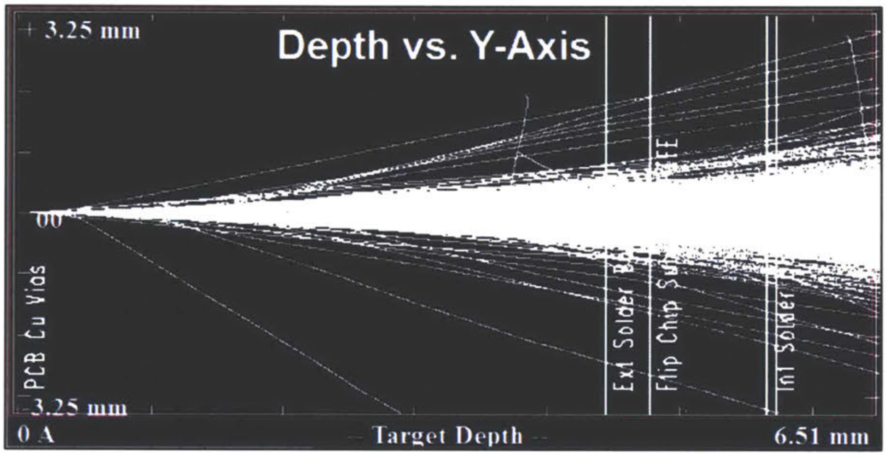

Figure 4.7 Integrated system TRIM simulation of five thousand 64.0 MeV protons penetrating through CL20010A1-EVK system. Worst case scenario is modeled for protons through copper-filled vias in PCB.

4.2.2 Layer-By-Layer CL20010A1-EVK System TRIM Simulations

Each layer in the CL20010A1-EVK system was individually modeled and simulated in TRIM. The TRIM ionization data (IONIZ.txt) of each simulated layer was input to the Matlab script, ioniz.m. For each simulated layer, ioniz.m calculates the average ionization energy loss per target depth thickness, the total ionization energy loss, and the ionization energy level of protons at the end of the layer. The ionization energy level of protons at the end of each layer is used as an input for the proton energy level for the following layer simulation. Figure 4.8 below shows a block diagram of the layer-by-layer TRIM simulation method.

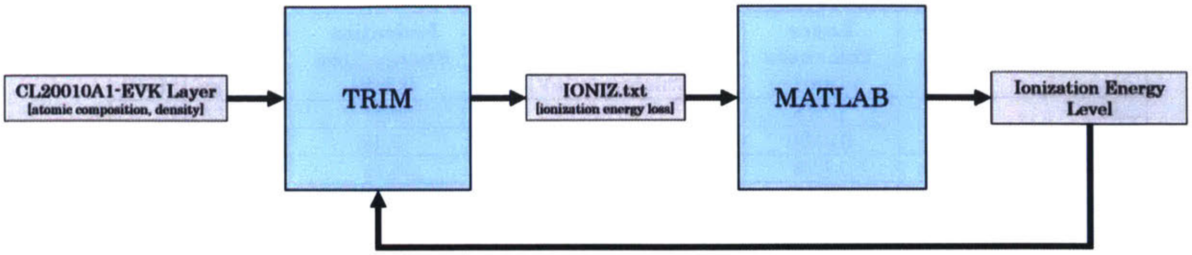

Figure 4.8 Layer-by-layer TRIM Simulation Method. The ionization energy level is input to a feedback loop, unlike the integrated simulation method in Figure 4.5.

For example, the first TRIM simulation for this method is a model of the copper layer on the bottom of the PCB. Protons with 64.0 MeV energy level are used for the first simulation through the first copper layer. The Matlab script calculated the ionization energy level of the protons at the end of the first copper layer as ~63.89 MeV. This is the proton energy level input for the TRIM simulation of the next layer, which was an ILD layer in the PCB. Each layer of the CL20010A1-EVK system was modeled with the same process as described for the first copper layer until the final ionization energy level is calculated for the protons through the CL20010A1 ASIC active region. Table 4.4 shows the calculations for the average ionization energy loss per target depth thickness, the total ionization energy loss, and the final ionization energy level for each layer.

Table 4.4. CL20010A1-EVK system layer-by-layer TRIM model calculations for average ionization energy loss per target depth thickness, the total ionization energy loss, and the final ionization energy level at the end of the layer.

Layer	Layer Thickness [μm]	Avg. Ionization Energy Loss per Layer Thickness [eV]	Ionization Energy Loss [MeV]	Final Ionization Energy [MeV]
Cu L1	17.78	0.60	0.11	63.89
ILD L1	312.00	0.15	0.46	63.44
Cu L2	17.78	0.60	0.11	63.33
ILD L2	50.80	0.15	0.07	63.25
Cu L3	17.78	0.61	0.31	62.95
ILD L3	208.00	0.15	0.31	62.64
Cu L4	17.78	0.61	0.11	62.53
ILD L4	200.66	0.15	0.30	62.23
Cu L5	17.78	0.61	0.11	62.12
ILD L5	208.00	0.15	0.31	61.81
Cu L6	17.78	0.62	0.11	61.70
ILD L6	200.66	0.15	0.30	61.40
Cu L7	17.78	0.62	0.11	61.29
ILD L7	208.00	0.15	0.31	60.97
Cu L8	17.78	0.62	0.11	60.86
ILD L8	200.66	0.15	0.31	60.56
Cu L9	17.78	0.63	0.11	60.44
ILD L9	208.00	0.15	0.32	60.13
Cu L10	35.56	0.63	0.22	59.90
ILD L10	50.80	0.15	0.08	59.82
Cu L11	35.56	0.63	0.23	59.60
ILD L11	104.00	0.15	0.16	59.44
Cu L12	71.12	0.64	0.45	58.98
ILD L12	50.80	0.16	0.08	58.90
Cu L13	71.12	0.64	0.46	58.45
ILD L13	104.00	0.16	0.16	58.28
Cu L14	35.56	0.64	0.23	58.06
ILD L14	50.80	0.16	0.08	57.97
Cu L15	35.56	0.65	0.23	57.74
ILD L15	208.00	0.16	0.33	57.41
Cu L16	17.78	0.65	0.12	57.30
ILD L16	200.66	0.16	0.32	56.98
Cu L17	17.78	0.65	0.12	56.86
ILD L17	208.00	0.16	0.33	56.53
Cu L18	17.78	0.66	0.12	56.41
ILD L18	200.66	0.16	0.32	56.09
Cu L19	17.78	0.66	0.12	55.97
ILD L19	208.00	0.16	0.34	55.63
Cu L20	17.78	0.67	0.12	55.51
ILD L20	200.66	0.16	0.33	55.18
Cu L21	17.78	0.67	0.12	55.06
ILD L21	208.00	0.16	0.34	54.72
Cu L22	17.78	0.68	0.12	54.60
ILD L22	50.80	0.17	0.08	54.52
Cu L23	17.78	0.67	0.12	54.40
ILD L23	208.00	0.17	0.34	54.05
Cu L24	17.78	0.68	0.12	53.93
Ext. Solder balls	330.00	0.49	1.62	52.31
Flip Chip Substrate	880.00	0.22	1.95	50.36
Int. Solder balls	75.00	0.51	0.38	49.97
CL20010A1 Silicon Die	775.00	0.23	1.81	48.16

The layer-by-layer TRIM simulation method calculates an ionization energy level of ~49.97 MeV entering the CL20010A1 ASIC silicon active region and an ionization energy level of ~48.16 MeV for protons penetrating through the end of the ASIC silicon active region. Figure 4.9 displays the TRIM simulation of five thousand protons with ~49.97 MeV energy level penetrating completely through the CL200101A1 ASIC silicon active region.

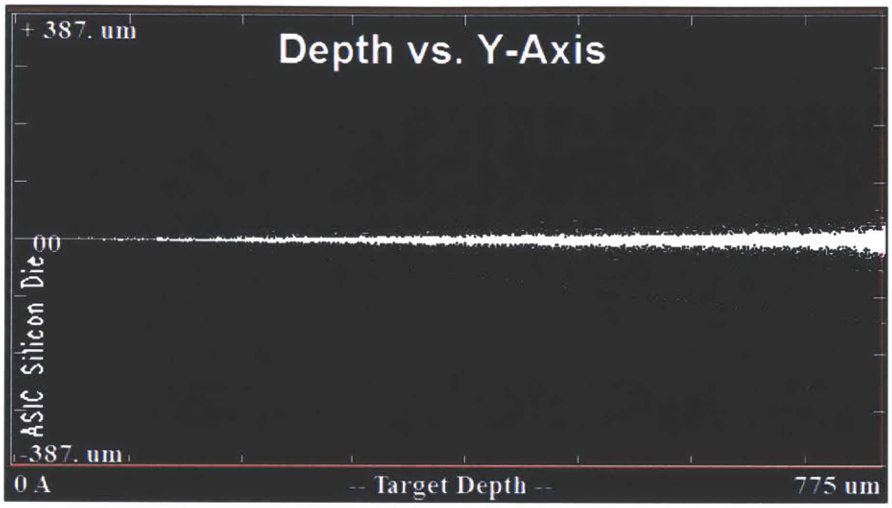

Figure 4.9. Layer-by-layer TRIM simulation of five thousand 49.97 MeV protons penetrating through CL20010A1 ASIC silicon active region

The layer-by-layer method verifies that protons with 64.0 MeV energy level would be sufficient to reach the CL20010A1 active region. With a final ionization energy level of 48.16 MeV at the end of the CL20010A1 active region, there is more than 40 MeV margin for 64.0 MeV protons to penetrate through the end of the active region if the TRIM simulations slightly deviate from the actual total ionization energy loss through the system.

4.2.2.1 Worst-Case Layer-by-Layer System TRIM Simulation

A layer-by-layer TRIM simulation is also conducted for the worst-case scenario of protons travelling through a path of copper-filled vias within the EVK PCB. Table 4.5 shows the calculations for the average ionization energy loss per target depth thickness, the total ionization energy loss, and the final ionization energy level for each layer in the worst-case model.

Table 4.5 CL20010A1-EVK system layer-by-layer TRIM model calculations for "worst-case" scenario of protons through PCB copper-filled vias. Calculations for average ionization energy loss per target depth thickness, the total ionization energy loss, and the final ionization energy level at the end of the layer.

Layer	Layer Thickness [µm]	Avg. Ionization Energy Loss per Layer Thickness [eV]	Ionization Energy Loss [MeV]	Final Ionization Energy [MeV]
PCB (Cu Vias)	4454.48	0.76	33.98	30.02
Ext. Solder balls	330.00	0.77	2.55	27.47
Flip Chip Substrate	880.00	0.38	3.38	24.09
Int. Solder balls	75.00	0.88	0.66	23.43
Silicon Die	775.00	0.44	3.43	19.99

The "worst-case" layer-by-layer TRIM simulation method results in an ionization energy level of ~23.43 MeV entering the CL20010A1 ASIC silicon active region and an ionization energy level of ~19.99 MeV for protons penetrating through the end of the ASIC silicon active region. Figure 4.10 displays the TRIM simulation of five thousand protons with ~23.43 MeV energy level penetrating completely through the CL200101A1 ASIC silicon active region. Even in this worst-case scenario, protons with 64.0 MeV energy level can still penetrate through the copper-filled vias in the PCB to reach the CL20010A1 active region. Based on the calculated energy level of protons penetrating through the active region, there is almost 20 MeV of margin if the TRIM simulations slightly deviate from the actual total ionization energy loss through the system.

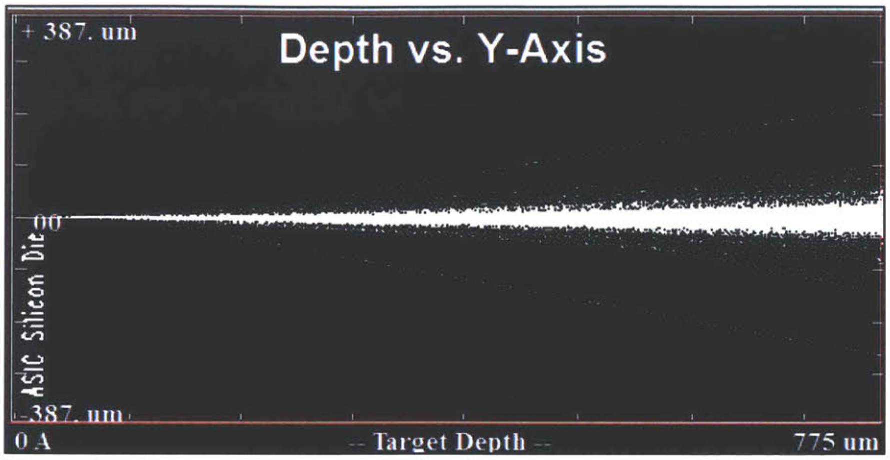

Figure 4.10 “Worst case” layer-by-layer TRIM simulation of five thousand 23.43 MeV protons penetrating through CL20010A1 ASIC silicon active region.

4.3 TRIM Analyses Summary

TRIM is used to analyze if 64.0 MeV protons could penetrate through the bottom side of the EVK and reach the CL20010A1 ASIC silicon active region. TRIM simulations of both the integrated system model and layer-by-layer model of the CL20010A1-EVK reveals that 64.0 MeV protons would reach the ASIC active region with margin. The integrated system simulation indicated an energy level of 50.22 MeV entering the CL20010A1 active region and the layer-by-layer model indicated an energy level of 49.97 MeV entering the CL20010A1 active region. The results of the two models did not significantly differ.

Simulations with both approaches are also conducted for the worst case scenario of protons travelling through a path of only copper-filled vias in the PCB. The worst-case simulation for the integrated model indicated an energy level of 23.30 MeV entering the CL20010A1 active region and the worst-case simulation for the layer-by-layer model indicated an energy level of 23.43 MeV entering the CL20010A1 active region. These results also did not significantly differ.

The results of the TRIM simulations are used to help plan proton radiation testing for SEEs and TID effects at the 64.0 MeV energy level.

Table 4.6 Summary of TRIM Simulation Results for ionization energy level of protons penetrating into and completely through the CL20010A1 ASIC active region.

Ionization Energy Level	Integrated System Approach	Layer-by-Layer Approach	Worst Case Integrated System Approach	Worst Case Layer-by-Layer Approach
Protons penetrating into CL20010A1 active region	50.22 MeV	49.97 MeV	23.30 MeV	23.43 MeV
Protons at end of CL20010A1 active region	48.40 MeV	48.16 MeV	19.87 MeV	19.99 MeV

Chapter 5

Single Event Effect and Total Ionizing Dose Assessment of the CL20010A1 ASIC with Proton Radiation Test Campaigns

Proton test campaigns are conducted to investigate the susceptibility of the CL20010A1 to SEEs as well as the CL20010A1 performance for increasing levels of TID. One proton test campaign was performed at UC Davis CNL with 64 MeV proton energy level and a second proton test campaign was conducted at Tri-University Meson Facility (TRIUMF) National Laboratory with 480 MeV proton energy level in January 2017. The 64 MeV proton energy level was selected based on the SRIM simulations of the CL20010A1-EVK system model described in Chapter 4. A higher proton energy level of 480 MeV was selected since solar energetic protons reach levels up to 500 MeV and GCR protons can reach energy levels up to 1 GeV [Varotsou, 2017; Hastings and Garrett, 1996]. Figure 5.1 highlights the relevant contributions from Chapter 5 in the high-level approach of this work and shows the path from SRIM simulations described in Chapter 4.

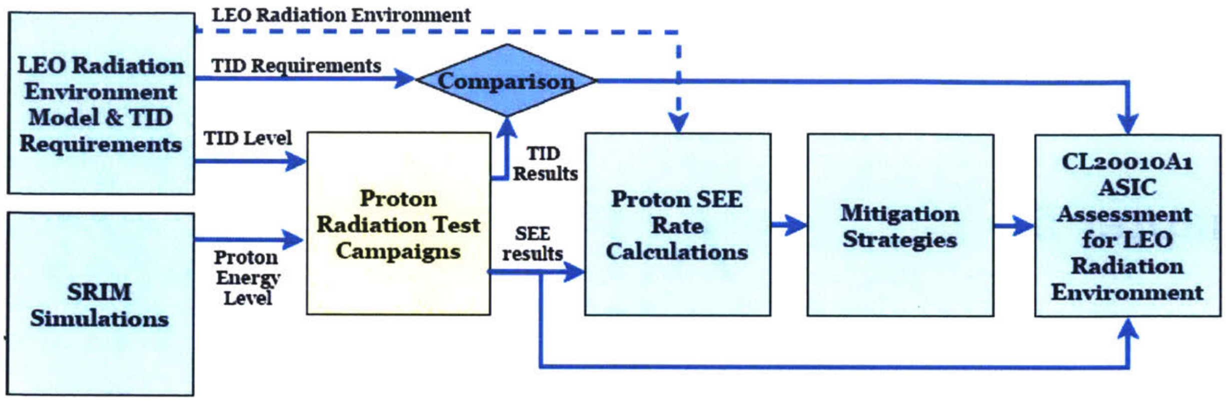

Figure 5.1 High-level approach used in this work to evaluate the CL20010A1 ASIC for LEO space radiation environment with Chapter 5 accomplishments highlighted in yellow.

5.1 Experimental Approach

5.1.1 Single Event Effect and Total Ionizing Dose Testing at Crocker Nuclear Laboratory Facility

SEE and TID measurements were performed at CNL using the custom EVK with the CL20010A1 ASIC and CFP2-ACO optical transceiver module. All radiation-sensitive commercial components were placed sufficiently far away from CL20010A1 on the EVK. The ASIC evaluation was performed in noise-loaded optical loopback (Figure 5.2). The transmit path was noise-loaded to set the optical signal-to-noise ratio (OSNR) level near the CL20010A1 receiver FEC correction threshold. This configuration represents the most stress for the optical transceiver system, because the optical communication link is signal-starved and the receiver is operating near the FEC threshold. The transmit and receive wavelengths of the CFP2 module were set to 1550.92 nm and transmit power to 0 dBm. The noise loading was accomplished by connecting the CFP2 module transmit output to a variable optical attenuator (VOA) followed by an erbium doped fiber amplifier (EDFA). The amplifier output was filtered with a 100 GHz optical band-pass filter (OBPF) centered at 1550.92 nm. The VOA attenuation was set to produce a pre-FEC bit BER of 0.01. The OSNR at this

BER is 1.6 dB higher than that required for BER of 0.02 which is the FEC "breaking" threshold.

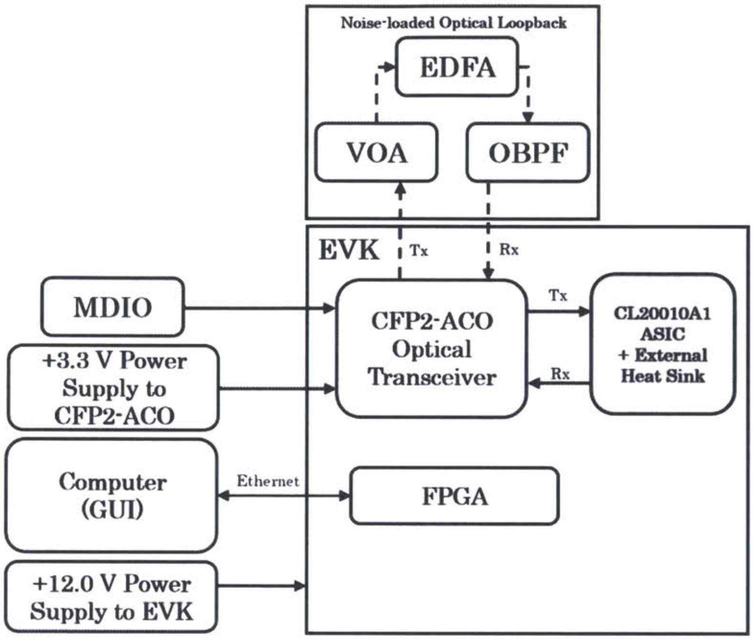

Figure 5.2 CL20010A1 SEE and TID experimental block diagram for CNL Testing

The EVK setup at CNL is shown in Figure 5.3, with the bottom of the board directly exposed to the incident proton beam. A laser was used to align the center of the proton beam to the center of the ASIC.

Figure 5.3 EVK proton irradiation test setup at CNL; (left) front side of board with CL20010A1 in top right corner and CFP2-ACO in top left; (right) irradiated back side of board and laser used for proton beam alignment.

At the beginning of each SEE test campaign, the proton beam was powered on and the start time recorded. The pre-FEC BER, the number of uncorrected FEC errors, and the connection to the EVK were actively monitored. Two types of SEEs were observed, SEUs and SEFIs, based on the following occurrences: EVK lost connection to CL20010A1 device and the receiver loss of lock (LOL). It could not be determined which type of SEE between SEUs and SEFIs specifically corresponded to each observed occurrence. After detection of a SEE, the proton beam was powered off, and the average beam flux and end time stamp were recorded. The CL20010A1 was subsequently power cycled, restoring all pre-SEE functionality. The SEE test was then repeated until a total of 10 SEE data points were collected.

After completion of SEE testing, performance of CL200010 ASIC was measured for increasing levels of TID. The CL20010A1 ASIC had been exposed to a cumulative 1211.35 rad(Si) from SEE testing. For the first five sets of TID testing, the proton beam current was set to 5 nA for five minute intervals, yielding TID of ~20 krad(Si) in each interval. The last round of TID testing irradiated the ASIC with the same beam current, but for a 10-minute interval, providing for additional 50 krad(Si). Hence, the ASIC was irradiated to a cumulative TID of 170 krad(Si). This level of TID sufficiently encompasses the LEO TID requirement levels determined in Chapter 2 from modeling the sample LEO missions and shown in Table 2.6. After each round of TID testing, the CL20010A1 was power cycled and the noise-loaded optical system performance was thoroughly characterized.

5.1.2 Single Event Effect Proton Test Campaign at TRIUMF National Laboratory

An identical EVK with CL20010A1 was used for proton testing at TRIUMF National Laboratory. In contrast to the test setup at CNL, the EVK at TRIUMF used a Finisar

ML4030 CFP2-ACO transceiver module in electrical loopback mode as the line-side interface, and the ASIC evaluation was not performed with noise-loading. The TRIUMF test setup diagram is shown in Figure 5.4.

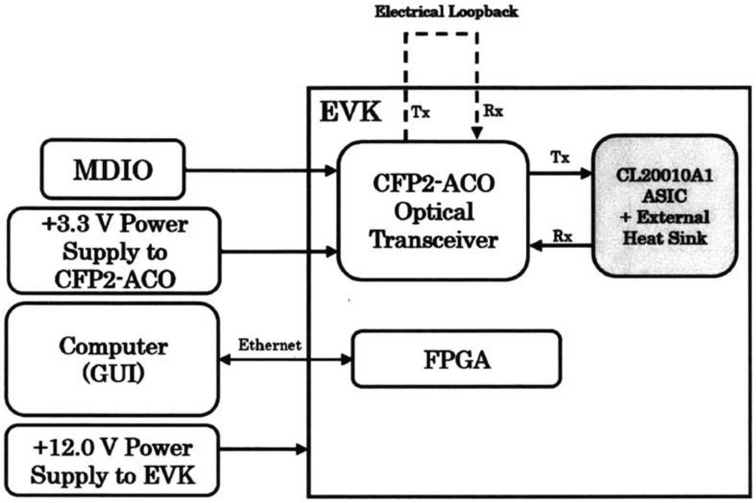

Figure 5.4 CL20010A1 SEU experimental block diagram for TRIUMF testing

The EVK setup at TRIUMF is shown in Figure 5.5, with the bottom side of the board directly exposed to the incident proton beam, as in the CNL setup. The center of the proton beam was aligned to the center of the ASIC with a laser. A 1-inch by 1-inch square aperture was used to focus the proton beam to a size closely encompassing the ASIC on the EVK.

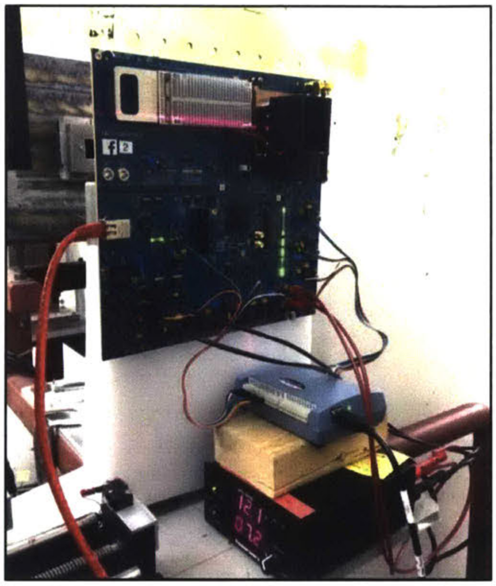

Figure 5.5 EVK proton irradiation test setup at TRIUMF. Front side of board with CL20010A1 in top right corner and CFP2-ACO in top left. Laser used for proton beam alignment.

5.2 Experimental Results

5.2.1 Single Event Effects

The specific types of SEEs observed include SEFIs and SEUs. No SELs were observed. Table 5.1 and Table 5.2 list the durations, average flux and accumulated fluence for each SEE test campaign at CNL with 64 MeV protons and at TRIUMF with 480 MeV protons, respectively.

Table 5.1 CL20010A1 SEE data from CNL test campaign with 64 MeV protons

SEE Number	Time Duration [seconds]	Average Flux [protons/second]	Fluence [protons/cm^2]
1	183	3.23×10^6	5.91×10^8
2	26	3.20×10^6	8.32×10^7
3	13	3.20×10^6	4.16×10^7
4	422	1.24×10^6	5.23×10^8
5	195	1.85×10^6	361×10^8
6	26	1.85×10^6	3.07×10^7
7	65	1.86×10^6	1.21×10^8

8	407	2.47×10^{6}	1.01×10^{9}
9	144	2.36×10^{6}	3.40×10^{8}
10	409	2.36×10^{6}	9.65×10^{8}

Table 5.2 CL20010A1 SEE data from TRIUMF test campaign with 480 MeV protons.

SEE Number	Time Duration [seconds]	Average Flux [protons/second]	Fluence [protons/cm^2]
1	2103	3.43×10^{6}	7.21×10^{9}
2	690	3.43×10^{6}	2.37×10^{9}
3	171	3.43×10^{6}	5.87×10^{8}
4	333	3.43×10^{6}	1.14×10^{9}
5	265	1.37×10^{7}	3.63×10^{9}
6	122	1.37×10^{7}	1.67×10^{9}
7	54	1.37×10^{7}	7.40×10^{8}
8	550	1.37×10^{7}	7.54×10^{9}
9	41	1.37×10^{7}	5.62×10^{8}
10	177	1.37×10^{7}	2.42×10^{9}
11	196	1.37×10^{7}	2.69×10^{9}
12	87	1.37×10^{7}	1.19×10^{9}
13	334	1.37×10^{7}	4.58×10^{9}
14	12	1.37×10^{7}	1.64×10^{8}
15	388	1.37×10^{7}	5.32×10^{9}
16	36	1.37×10^{7}	4.93×10^{8}
17	240	1.37×10^{7}	3.29×10^{9}
18	114	1.37×10^{7}	1.56×10^{9}

The test data from both proton test campaigns are used to calculate the proton SEE cross-sections in Chapter 6. The results are further discussed in Chapter 6 and are used to calculate the CL20010A1 SEE rate for the LEO missions modeled in Chapter 2.

5.2.1 Total Ionizing Dose

The summary of TID runs is listed in Table 5.3. Following each run, the CL20010A1 had to be power cycled to restore operation. The pre-FEC BER was measured and used to assess any potential degradation in the transmit and/or receive paths of the ASIC. In particular, any degradation in the mixed-signal portion of the device would have degraded the signal quality and therefore the BER prior to FEC correction. No significant measurable change in ASIC performance was observed (Figure 5.6) up to a TID level of 170 krad(Si). The test was stopped after the sixth round of TID irradiation due to facility closure.

Table 5.3 CL20010A1 ASIC TID data summary from CNL test campaign with 64 MeV protons

Time Duration [seconds]	Average Beam Flux [protons/second]	Cumulative Fluence [protons/cm^{2}]	Cumulative TID [krad]	Average Pre-FEC BER
348	$5.93\text{x}10^{8}$	$1.87\text{x}10^{11}$	25.01	$9.41\text{x}10^{-3}$
300	$5.56\text{x}10^{8}$	$3.57\text{x}10^{11}$	47.71	$9.41\text{x}10^{-3}$
300	$5.69\text{x}10^{8}$	$5.28\text{x}10^{11}$	70.51	$8.53\text{x}10^{-3}$
300	$5.75\text{x}10^{8}$	$7.01\text{x}10^{11}$	93.61	$8.53\text{x}10^{-3}$
300	$6.42\text{x}10^{8}$	$8.94\text{x}10^{11}$	119.41	$9.02\text{x}10^{-3}$
600	$6.22\text{x}10^{8}$	$1.27\text{x}10^{12}$	169.31	$9.11\text{x}10^{-3}$

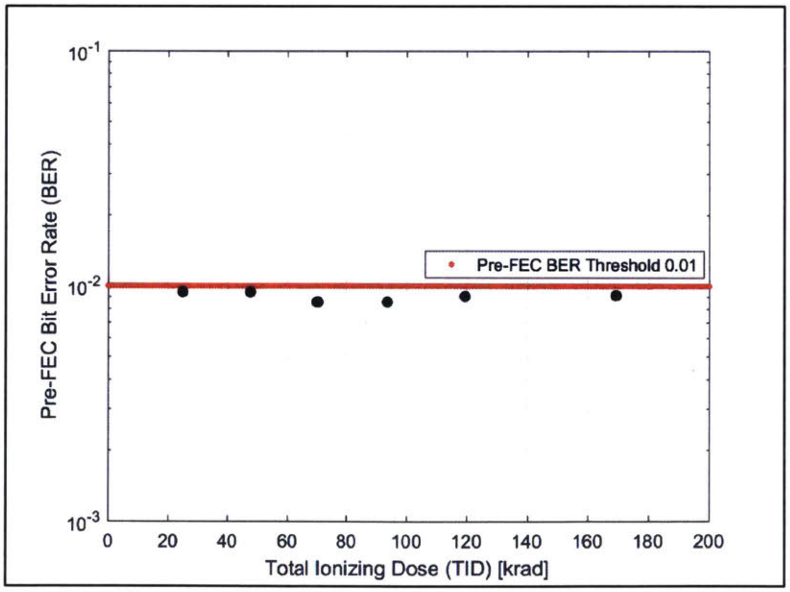

Figure 5.6 CL20010A1 Pre-FEC BER vs TIDs

Chapter 6

Single Event Effect Calculations for CL20010A1 ASIC

Proton SEE data from the CNL and TRIUMF test campaigns are used to calculate the proton SEE cross sections for energy levels 64 MeV and 480 MeV, respectively. Figure 6.1 highlights the relevant step accomplished from Chapter 6 in the high-level approach of this work and shows the transition in the path with SEE data collected from the proton test campaigns. The proton SEE rate calculations in this chapter will be used assess mitigation strategies against radiation effects on the CL20010A1 (Chapter 7), such as programming periodic resets or power cycles.

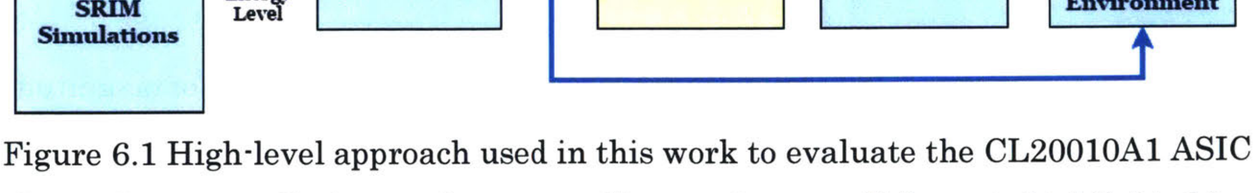

Figure 6.1 High-level approach used in this work to evaluate the CL20010A1 ASIC for LEO space radiation environment. Chapter 6 accomplishments highlighted in yellow. The transition in the path with the SEE data collected from the proton test

campaigns is showed. SEE rate calculation will be used to assess mitigation strategies against radiation effects on the CL20010A1.

6.1 Proton Single Event Effect Cross Section Calculations and Analyses

Equation 2.6 was used to calculate the SEE cross sections. The calculated SEE cross section values, based on proton energy level, are listed in Table 6.1 and plotted in Figure 6.2.

Table 6.1 SEE cross section results from proton beam testing of CL20010A1 ASIC

Proton Energy Level [MeV]	Single Event Effect Cross Section [cm^2]
64	2.46×10^{-9}
480	3.82×10^{-10}

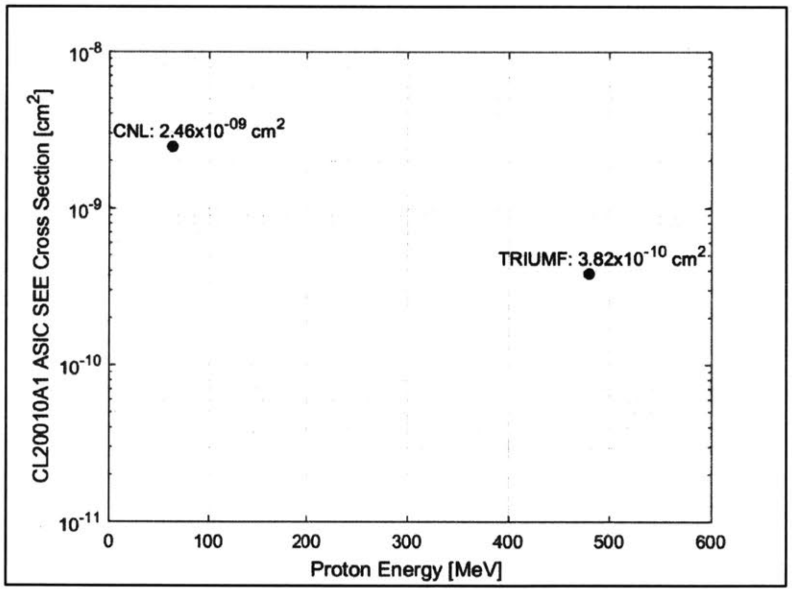

Figure 6.2 CL20010A1 ASIC proton single event effect cross-section data

The SEE cross-section at 480 MeV proton energy level is nearly an order of magnitude lower in comparison to that at the lower 64 MeV proton energy level. These results differ from the expectation of a higher proton SEE cross section for a higher proton energy level. After the Bragg peak energy level, higher proton energy levels have a lower LET or stopping power. Figure 6.3 shows the LET curve as a function of energy level for protons penetrating through silicon material. The Bragg peak energy level for silicon is 55 keV with LET 5.382 x 10^{-1} MeV/(mg/cm^2), and proton energy levels greater so 55 keV have decreasing LET values.

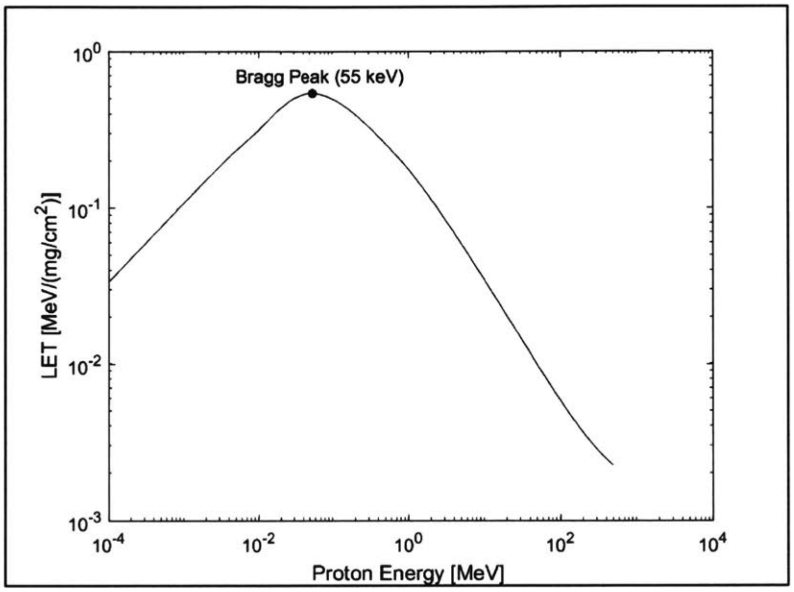

Figure 6.3 LET versus energy curve for protons through silicon target material

Previous studies on proton-induced SEEs in CMOS technologies, specifically SRAMs, observe results consistent this work, where lower proton energy levels induce higher SEE cross section values in comparison to higher proton energy levels [Heidel et al., 2008; Cannon et al., 2010. Guillermin et al., 2016]. Both attribute the results of higher proton SEE cross sections for lower proton energy levels to direct ionization effects. In commercial CMOS circuit devices for space applications, proton-induced SEEs are dominated by secondary ions generated from nuclear collision events rather than by direct ionization [Heidel et al., 2008]. However, the studies by Heidel et al. [2008], Cannon et al. [2010], and Guillermin et al. [2016] find that a significant number of SEEs are produced from direct ionization from protons relative to high energy collision events. The proposal is that for a certain range of low energy protons (prior to the Bragg peak energy level), the ionization rate as the particles cross a device is higher in comparison to the rate for higher energy protons. These low energy protons have high LETs and are losing energy rapidly [Petersen, 1996].

The Cannon et al. [2010] study assesses proton SEE sensitivity of a 90-nm SRAM device. One proton test campaign in the study assesses an energy range from 0.6 MeV to 2.0 MeV at the Boeing Radiation Effects Laboratory (BREL). For proton energy levels less than 1 MeV, the cross section curve increased to a peak value at ~ 0.7 MeV then decreased for following energy levels to ~ 1 MeV. There was a slight increase in SEE cross section values for energy levels between 1 MeV to 2 MeV. In a second proton test campaign of the same unit, the SEE cross sections were determined for energy range ~20 MeV to 200 MeV at Indiana University Cyclotron Facility (IUCF). The highest proton SEE cross section was observed slightly above 20 MeV and the SEE cross section values decreased for the data collected at increasing proton energy levels. In both test campaigns, the greatest SEE cross section values occurred at energy levels above the silicon Bragg peak value of 55 keV.

In the Heidel et al. [2008] study, proton SEE sensitivity is assessed for a silicon on insulator (SOI) SRAM device. SEE data over a 1 to 500 MeV energy range was collected from proton test campaigns at 5 different accelerators. Similar to the Cannon et al. [2010] study, the cross section data showed significant rise in SEEs approximately below the 1 MeV energy level. Data collected from the CNL test campaign with the 14.6 MeV proton beam showed an increase in SEE cross section values between 10 MeV and 30 MeV. The cross section was also observed to slightly increase at around the 30 MeV level for proton test campaigns at TRIUMF and Northeast Proton Therapy Center (NPTC), and the cross section values tended to decrease as proton energy increased between 30 MeV and 100 MeV.

For a proton beam energy level of 64.0 MeV, CL20010A1-EVK SRIM model simulations from Chapter 4 predict that the proton energy level entering the CL20010A1 silicon active region would be ~50 MeV for the nominal case model and

~23 MeV for the worst case model. The worst case model represents the scenario of protons travelling through a path of copper-filled vias in the PCB. The results of the CNL proton test campaign with 64.0 MeV protons could be considered consistent with observations of the Heidel et al. [2008] and Cannon et al. [2010] studies, if the worst case SRIM model simulation of the CL20010A1-EVK occurred with ~23 MeV protons entering the silicon active region. In the Cannon et al. study [2010], the proton SEE cross section values decreased as proton energy levels increased between 20 MeV and 200 MeV. Although this similar trend was observed by Heidel et al. [2008], the observation was over the proton energy range between 30 MeV and 100 MeV.

The Cannon et al. study [2010] also modeled the CMOS SRAM DUT in SRIM to evaluate the proton energy levels through the active region. However, the study described limitations in the SRIM program with modeling detailed layers of the device and approximating metallization layers as a uniform layer of dielectric. The Canon et al. SRIM model did not account for different proton trajectories crossing different materials within a layer and introducing spread in the final proton energy distribution. Device metallization and passivation layers significantly broaden the proton energy spectrum at the active silicon region despite the tight energy spread of the proton beam [Cannon et al., 2010].

A similar situation to the Cannon et al. [2010] study could have occurred with this work due to limitations with the SRIM model of the CL20010A1-EVK. As described in Chapter 4, the CL20010A1-EVK SRIM model was based on assumptions of the chemical composition of the PCB and packaging material layers as well as approximated detailed, metallization and passivation layers. In the proton test campaigns at CNL and TRIUMF described in Chapter 5, broadening of the proton energy spectrum through the 51 layers of PCB and packaging material is highly likely to have occurred. The protons in the silicon active region of the CL20010A1 could have been in the energy range (near 1 MeV for the two studies mentioned) for causing direct ionization. The low energy protons between 0.5 MeV to 1.0 MeV entering the

CL20010A1 could have stopped inside the active region and the Bragg peak could have been located within the active region [Guillermin et al., 2016].

Overall, the effects of proton direct ionization in the Heidel et al. [2008] and Cannon et al. [2010] appear to be consistent with the results of this work. A greater number of proton SEE data points at different energy levels will need to be collected through future test campaigns and compared to the Heidel et al. [2008] and Cannon et al. [2010] studies. Additional proton test campaigns are proposed and described in Section 8.2.1.

6.2 Proton Single Event Effect Rate Calculations for the CL20010A1 ASIC

The SEE proton cross section results from experimental testing of the CL20010A1 are used to calculate the SEE rate of the CL20010A1 for the sample LEO missions described in Chapter 2 and summarized in Table 2.4. Section 2.2.3.2 describes the process and details of SEE rate calculations. The SEE rate calculation module within OMERE was used for the calculation.

The CL20010A1 ASIC is modeled into the component database of SEE rate calculation module as a component of 1 sensitive cell with a 775 μm cell depth. The SEE proton cross section data from Table 6.1 was used for a Weibull fit curve. Equation 6.1 is the functional form of the Weibull function used to calculate the proton SEE cross section ($F(x)$) in units of cm^2 [Petersen et al., 1992; Tylka, et al., 1996]. The proton energy in units of MeV is represented by x, the limiting cross section is represented by A, the Weibull width parameter is represented by W, and the Weibull dimensionless exponent parameter is represented by s.

$$F(x) = A\left(1 - e^{-\left[\frac{x-x_0}{W}\right]^s}\right)\ [cm^2]\ \text{(Equation 6.1)}$$

Table 6.2 displays the Weibull width parameter, *W*, and the Weibull dimensionless exponent parameter, *s*, for the CL20010A1 proton SEE cross section Weibull distribution fit. Figure 6.4 displays the Weibull curve fit from the proton SEE cross section data.

Table 6.2 Weibull parameters for curve fit from proton SEE cross section data.

W	**s**
0.84112	–0.28699

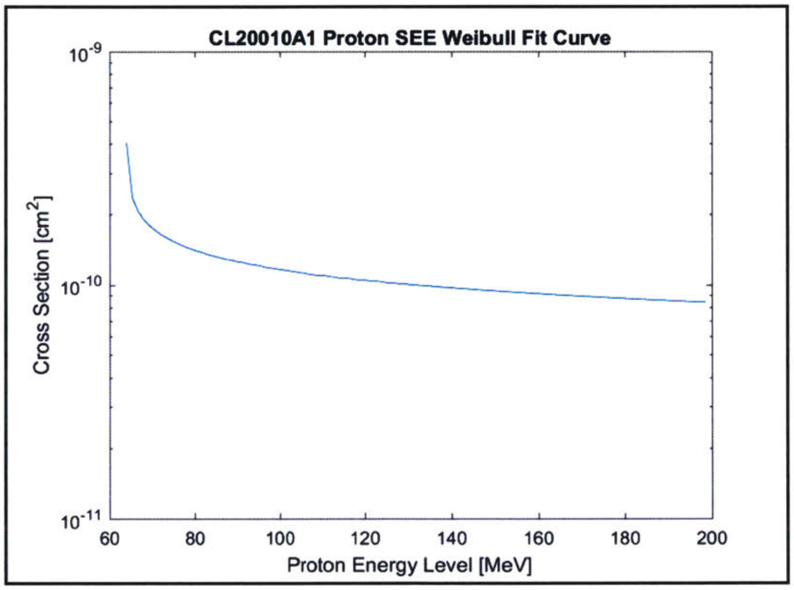

Figure 6.4 CL20010A1 proton SEE cross section Weibull fit curve

Due to the proton SEE cross section results, the CL20010A1 Weibull fit curve does not follow the expected Weibull distribution or behavior. The nominal Weibull fit distribution behavior is shown in Figure 6.5, with the proton SEE cross section having initial logarithmic-like growth and reaching a plateau as proton energy level increases [Petersen, 1996]. The CL20010A1 proton SEE cross section Weibull fit curve has a leveled, exponentially decreasing behavior with decreasing proton SEE cross section for increasing proton energy levels. Additional proton test campaigns, described in section 8.2.1, will be conducted in future work to include more proton

SEE cross section data points at energy levels below 64 MeV and between 64 MeV and 480 MeV. Additional SEE cross section data points will provide greater fidelity in the Weibull fit curve and in the final SEE rate calculation.

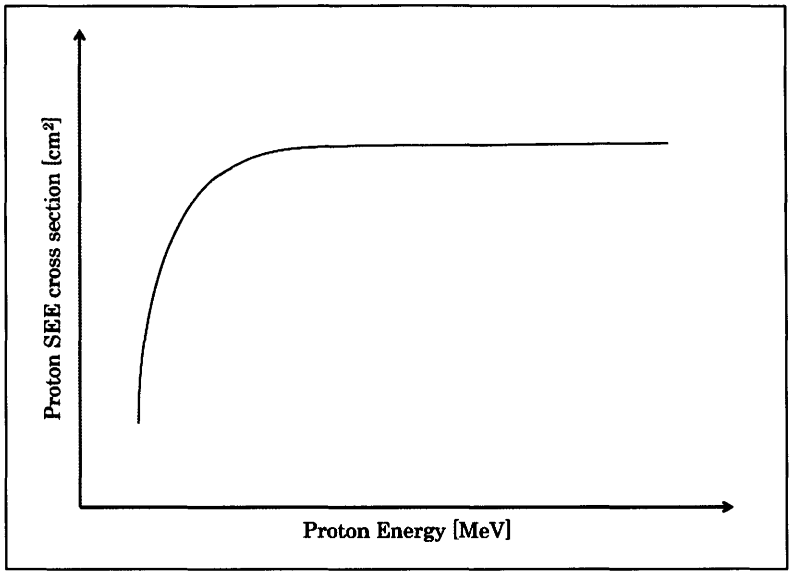

Figure 6.5 Nominal proton SEE cross section Weibull distribution behavior

Proton mission environment data for each of the LEO missions is taken into account with the proton Weibull fit curve to calculate the SEE rate specific to each mission. The proton mission environment was defined by trapped proton fluxes, solar flare proton fluxes, and cosmic ray proton fluxes transported through 100 mils of aluminum shielding. The proton fluxes transported were calculated through the OMERE Transport module, which generated a transport proton flux file as an input to the environment data field of the OMERE SEE rate calculation module. Table 6.3 shows the proton SEE rate calculations for each sample LEO orbit.

Table 6.3 Proton SEE rate calculations for each modeled LEO orbit.

LEO Mission Orbit	Proton SEE Rate [SEEs/day]	Proton SEE Rate [SEEs/year]
ISS	3.82×10^{-3}	~ 1.38
1000 km, 0° Inclination	2.61×10^{-3}	~ 0.95

800 km, Polar	5.44 x 10^{-2}	~ 19.59

The calculated SEE rates for the sample LEO missions estimate that the CL20010A1 could experience under ~2 proton-induced SEEs per year in an ISS orbit, ~1 proton-induced SEE per year in a 1000 km 0° inclination orbit, and as many as ~ 20 proton-induced SEEs per year in an 800 km polar inclination orbit. These SEE rates could be used to program a reset of the CL20010A1 or power cycle the full OTA system, as discussed in Chapter 7.

Chapter 7

Mitigation Strategies Against Radiation Damage to the CL20010A1 ASIC

The main mitigation strategies to protect the CL20010A1 against radiation damage are physical techniques of spot shielding, strategic placement in the spacecraft, and incorporation of diagnostic or protective electronic devices in the circuit board design with the CL20010A1. Software-based approaches to help resolve SEEs could be implemented, such as programming device or system resets or power cycles based on the calculated SEE rate could be used to resolve SEEs. Software mitigation strategies (like voting logic) cannot be applied directly to the ASIC as a pre-programmed device. Other strategies could include design and development of a radiation-tolerant ASIC, but the intent of this work is to explore the potential of using the commercial CL20010A1 for a space application in the LEO radiation environment.

7.1 Spot Shielding

Spot shielding on sensitive areas of a device or system is a common mitigation strategy used by spacecraft designers against TID effects. Specifically, spot shielding is effective in protecting against electrons and low-energy protons. The dose depth curve from space environment modeling of a mission can be used to determine the appropriate amount of shielding needed for a component or system to meet TID requirements. Aluminum is typically the baseline shielding material used to calculate the TID curve for a given mission and can be used for additional low mass spot shielding. Tantalum, tungsten, and lead are also typically used for spot shielding since these materials are high electron or high-Z materials with higher the density than aluminum [Maurer, 2008]. These materials could be difficult to use for mass-sensitive spacecraft, but the high density allows for thinner shields than aluminum. Thin shields could be specifically applied to regions with tightly packed printed circuit boards, such as an optical transceiver assembly with the CL20010A1.

Besides an increase in mass and volume on a spacecraft, spot shielding may have other disadvantages, such as inducing additional radiation effects. Bremsstrahlung or secondary electrons and photons can be generated from ionizing radiation penetrating through high-Z material spot shields [Biddle & Monteiro, 2012]. A thin inner layer of aluminum can be applied under the high-Z spot shields and at the integrated circuit die to shield against potential Bremsstrahlung radiation effects. It is important to make sure that any shielding is properly grounded. However, thick spot shields with high-Z materials can increase the SEE rate on a device from the generated Bremsstrahlung particles [Maurer, 2008].

7.2 Strategic Placement in Spacecraft

Strategic component or system placement within the spacecraft is another common mitigation strategy. Other spacecraft components can serve as additional sources of shielding to sensitive devices or systems. Modeling can be used to determine the impact of radiation effects on a component in different locations on a spacecraft. Tools or programs, such as FASTRAD and GEANT4, can be used in the spacecraft design phase to ensure that sensitive components or systems are strategically placed in areas with sufficient shielding from radiation effects.

7.3 Incorporation of Protective Electronic Devices in Circuit System Design

Protective components can be incorporated to the circuit board design of an optical transceiver assembly with the CL20010A1 ASIC to prevent destructive damage from SEEs. A Latch-Up current limiter (LCL) is a protection device incorporated in digital circuit systems, such as ASICs and FPGAs, sensitive to SELs. SELs can have destructive effects on a device and are observed through over-current levels. LCLs, such as the 3DPM0168-2 from 3D Plus, monitor the power supply line of the radiation sensitive device and instantaneously switches it off when it detects over-current levels in the occurrence of radiation-induced SELs [3D Plus, 2013]. The 3D Plus 3DPM0168-2 LCL is "Rad Hard by Design", designed with radiation mitigation techniques and utilizes space design derating rules. This LCL could be used in the circuit system with the CL20010A1 and programmed with current thresholds specific to the CL20010A1.

A power distribution load switch is another protective device that could be incorporated in the board layout with the CL20010A1. This device would also protect the CL20010A1 from SELs. The AP22802 by Diodes Incorporated is a single channel current-limited integrated high-side power switch used as a protection solution against heavy capacitive loads, short circuit, and over-current [Diodes Incorporated, 2015].

7.4 Programming Periodic CL20010A1 Resets or Full System Power Cycles

Resetting the device or power cycling the full system are two ways to restore loss of normal operation in the CL20010A1 caused by SEEs. Based on the SEE rate calculation for a given LEO mission described in Chapter 6 and summarized in Table 6.3, the CL20010A1 could be programmed with periodic resets or the full optical transceiver system could be programmed with periodic power cycles. The device resets or the full system power cycles would need to be strategically programmed to not interfere with optical transceiver operation during the mission. Power cycling the full system with the CL20010A1 is an aggressive solution to restoring normal operation so it is recommended that more periodic device resets occur than full system power cycles.

Chapter 8

Conclusions and Future Work

8.1 Conclusions

The Inphi CL20010A1, a commercial, optical coherent DSP ASIC, was evaluated for application in a LEO radiation environment. This work introduced the LEO radiation environment, described the main sources of radiation expected for the orbits of interest, and focused on the effects that are most relevant for the device characteristics. The radiation environment for sample LEO missions were modeled using OMERE and the expected TID to the CL20010A1 was calculated for each mission based on dose depth curves (Table 2.5). A set of TID requirements for each LEO mission was created in Table 2.6. The CL20010A1 was analyzed, and the potential radiation damage to this CMOS device was evaluated. SRIM analyses of the CL20010A10-EVK system were conducted to evaluate the proton energy sufficient to penetrate through the EVK system and reach the silicon active region of the CL20010A1. Simulations showed that 64 MeV protons have sufficient energy to penetrate through the active region, and there is margin if TRIM simulations slightly deviate from the actual total ionization energy loss through the system. Two proton radiation test campaigns at 64 MeV and 480 MeV were conducted to assess the performance of the CL20010A1 to TID and SEEs. Proton SEE cross section data from the proton test campaigns was used to calculate the SEE rate. Potential radiation damage mitigation strategies for the CL20010A1 were proposed.

Based on modeling the radiation environment for the three sample LEO missions (ISS orbit, 1000 km with 0° inclination, and 800 km in polar orbit) over 1-year, 5-year, and 10-year durations, the maximum expected TID that the CL20010A1 ASIC would encounter for 100 mils aluminum shielding is 44.3 krad for a 10-year, 800 km polar orbit. For the TID requirements with 2x margin, the highest expected TID is 88.6 krad. The CL20010A1 ASIC survived and experienced no performance degradation from TID exposure up to 170 krad(Si). Thus, the CL20010A1 meets the TID requirements for the sample LEO missions and has a TID tolerance of at least 170 krad (Si), which surpasses the requirements.

When the CL20010A1 is implemented into an optical transceiver assembly (OTA) and into a spacecraft payload, additional shielding from the OTA housing, payload components, and spacecraft structure will further protect the CL20010A1 from TID effects. Careful consideration should be taken to evaluate if other components may be susceptible to TID at lower doses. Detailed analyses with modeling tools, such as FASTRAD and GEANT4, can be used to evaluate the CL20010A1 in an OTA and in a spacecraft.

The measured CL20010A1 proton SEE cross section was 2.46×10^{-9} cm^2 at the 64 MeV energy level and 3.82×10^{-10} cm^2 at the 480 MeV energy level. The results of the SEE cross section data are attributed to proton direct ionization effects. Based on the cross section data, the calculated SEE rates for the sample LEO missions estimated that the CL20010A1 could experience under ~2 proton-induced SEEs per year in an ISS orbit, ~1 proton-induced SEE per year in a 1000 km 0° inclination orbit, and as many as ~ 20 proton-induced SEEs per year in an 800 km polar inclination orbit. These SEE rates could be used to program a reset of the CL20010A1 or power cycle the full OTA system.

Overall the findings of this work suggest that the Inphi CL20010A1 ASIC could be feasibly implemented on a spacecraft application in the LEO radiation environment.

8.2 Future Work

Further evaluation of the performance of the CL20010A1 at different proton energy levels and up to higher levels of TID could be completed through additional proton radiation test campaigns. Heavy ion test campaigns of the CL20010A1 would also provide useful insight on the effects of heavy ions. Data from additional test campaigns could be used to better understand CL20010A1 radiation tolerance and effects to CL20010A1 performance from radiation damage. This work could be used as an initial step toward developing a coherent optical communications optical transceiver with COTS components, such as the CL20010A1.

8.2.1 Additional Proton Radiation Test Campaigns

Additional proton radiation test campaigns could be completed on the previously tested CL20010A1 ASICs, as described in Chapter 6, at different proton energy levels. Proton SEE cross section data for energy levels between ~45 MeV to 64 MeV and between 64 MeV and 480 MeV could be used to evaluate if proton direct ionization yields effects on the CL20010A1. 45 MeV is preliminarily indicated as the lowest energy level for an additional test campaign, based on SRIM simulations results in Chapter 4 and summarized in Table 4.6. The SRIM simulation results showed that 64.0 MeV protons in the modeled CL20010A1-EVK system have ionization energy levels of ~ 20 MeV and ~48 MeV at the end of the active region in the worst case model and baseline model, respectively. An energy level of 45 MeV protons appears sufficient for protons to still reach the end of the active region. Additional SRIM simulations with 45 MeV protons will need to be completed to confirm this hypothesis, prior to future proton test campaigns.

SEE cross section data points from additional proton test campaigns could be further compared to the two studies mentioned in Chapter 7 with relevant results due to proton direct ionization effects. The results from additional proton radiation test campaigns at different energy levels could also provide other proton SEE cross section data points, which could be incorporated in the Weibull-fitted SEE proton cross section curve in Chapter 7. Additional data points would provide for a more statistically significant Weibull-fitted proton cross section curve of the CL20010A1. Thus, a higher fidelity CL20010A1 SEE rate could be estimated for a specific mission.

An additional proton radiation test campaign at the 64 MeV energy level could be conducted on the same CL20010A1 ASIC to evaluate the ultimate TID tolerance of the device. The test campaign assessed the CL20010A1 up to TID level of 170 krad (Si). Further testing to higher TID levels were not completed due to time limitations at the test facility. A TID level of 170 krad(Si) is sufficient for a LEO environment, but if there is interest in testing for GEO environment, higher TID levels could be tested.

The 64 MeV and 480 MeV proton test campaign in Chapter 6 could be repeated for CL20010A1 ASICs manufactured in different lot. The results of all test campaigns could be compared to provide a better understanding of differences in radiation tolerance for CL20010A1 ASICs based on manufacturing lot and to evaluate consistency in the Inphi manufacturing process for these devices.

Table 8.1 summarizes the additional proton test campaigns that could be completed for future work. Data from these test campaigns could provide useful information to further assess proton radiation effects on the CL20010A1.

Table 8.1 Proposed future proton test campaigns to further assess performance of CL20010A1 to LEO radiation effects. *Indicates additional SRIM simulations needed to determine the lowest energy level to reach the end of the CL20010A1 active region.

Proton Energy Level	**Unit**	**Reasoning**
Between 45 MeV* – 64 MeV	Both the CL20010A1 unit tested in this	Obtain additional SEE cross section data points for Weibull distribution.

	work and a different CL20010A1 unit	Evaluate SEE cross-section values at energy levels below 64 MeV. Conduct additional TID tolerance testing.
64 MeV	CL20010A1 unit tested in this work	Evaluate ultimate TID tolerance.
	Different CL20010A1 unit	Compare SEE cross section values at 64 MeV of previously tested CL20010A1 unit against different CL20010A1 unit. Evaluate consistency in SEE test results. Conduct additional TID tolerance testing.
Between 64 MeV – 480 MeV	Both the CL20010A1 unit tested in this work and a different CL20010A1 unit	Obtain additional SEE cross section data points for Weibull distribution. Evaluate SEE cross-section values between 64 MeV and 480 MeV Conduct additional TID tolerance testing.
480 MeV	Different CL20010A1 unit	Compare SEE cross section values at 480 MeV of previously tested CL20010A1 unit against different CL20010A1 unit. Evaluate consistency in SEE test results. Conduct additional TID tolerance testing.

8.2.2 Heavy Ion Radiation Test Campaigns

Proton beam testing was used to generate TID effects and SEEs on the CL20010A1 ASIC. However, it is also important to complete heavy ion radiation testing of the CL20010A1 to evaluate SEEs caused by heavy ions from GCRs and solar flares. Protons undergo nuclear interactions, which then subsequently produce SEEs through direct ionization. In contrast, most heavy ion-induced SEEs are from direct ionization [Buchner et al., 2002].

TRIM simulations and analyses, as described in Chapter 4, could be repeated with ions instead of protons prior to heavy ion testing. These simulations would be used to evaluate the required energy levels of ions sufficient to penetrate through the bottom side of the OTA and into the CL20010A1 silicon active region. The experimental methodology and setup for heavy ion testing of the CL20010A1-EVK would be similar to the CNL and TRIUMF proton beam tests described in Chapter 5. The experimental data from the heavy ion tests would be used to calculate ion SEE cross section data points for specific LET levels. A Weibull distribution curve would be fitted to the ion SEE cross section data from heavy ion testing, and the Weibull curve would be used to calculate the estimated SEE rate for a specific mission.

8.2.3 Development of a Coherent Optical Transceiver for LEO spacecraft application

The Inphi CL20010A1 DSP ASIC is an integral component needed for the development of a coherent, DSP optical transceiver, which can transmit and receive optical signals with data rates up to 200 Gbps. Future work will focus on designing and developing an OTA with the CL20010A1 and commercial optical components for line side.

The commercial optical components for OTA line side would include an optical modulator, modulator driver, and optical coherent receiver. Research will be conducted on the susceptibility of these optical components to LEO radiation damage. The performance of these components would be assessed for radiation damage through radiation testing. Optical components are susceptible to TID and TNID effects from trapped particles, solar protons, and GCR protons in the LEO radiation environment. Radiation testing for TID effects and displacement damage effects is also necessary for these components. After testing the commercial optical components individually, a fully integrated OTA with the CL20010A1 and line-side optical components, such as an optical modulator, modulator driver, and optical coherent receiver, could be tested for ionizing and non-ionizing radiation damage.

This work is a first step toward assessing the feasibility of a commercial-based 200 Gbps coherent optical communications transceiver for use on a spacecraft in the LEO radiation environment.

Appendix

A.1 Single Event Effects

An SEU can also trigger an SET, which is an electrical pulse of signal or voltage generated in the device and propagated from the device to the system [Normand, 2004]. SETs occur in analog and linear devices, such as voltage references, operational amplifiers, voltage regulators, and comparators [Samaras, 2014]. Peaks in voltage amplitude and high voltage durations of a device characterize a SETAlthough a SET can be non-destructive to a device, the effects of a SET can be destructive to a system if there are connected components which take voltage input from the SET-affected device.

Single event stuck bits (SESBs) result in the change to device functionality or operation from a stuck bit in a memory device. SEBEs are a type of SEHE with only semi-permanent damage since annealing can recover functionality of the memory device [Samaras, 2014].

SEGRs result from an ion-induced formation of a conducting path in the gate oxide of N-channel or P-channel power MOSFETs. A SEGR is observed through the dielectric breakdown of a power MOSFET gate [Samaras, 2014]. SEBs occur in power transistors, specifically N-channel power MOSFETs. These type of SEEs result in a high current state and are caused by the activation of parasitic NPN bipolar transistor in vertical power MOSFET [Normand, 2004, Miroshnichenko, 2003]. SEDRs are the result of the breakdown of thin oxide layer in programmable IC, linear devices, such as FPGAs.

A.2 Matlab Script for TRIM Simulation Data Analyses

Filename: ioniz.m

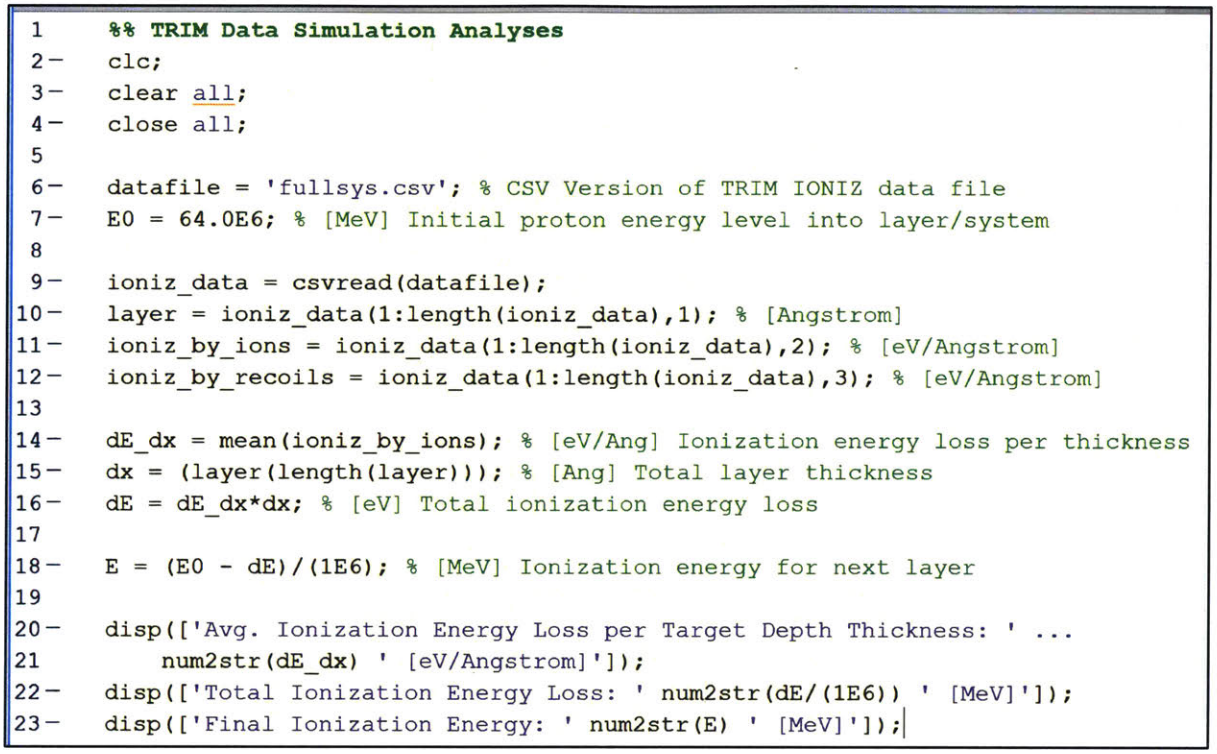

```
%% TRIM Data Simulation Analyses
clc;
clear all;
close all;

datafile = 'fullsys.csv'; % CSV Version of TRIM IONIZ data file
E0 = 64.0E6; % [MeV] Initial proton energy level into layer/system

ioniz_data = csvread(datafile);
layer = ioniz_data(1:length(ioniz_data),1); % [Angstrom]
ioniz_by_ions = ioniz_data(1:length(ioniz_data),2); % [eV/Angstrom]
ioniz_by_recoils = ioniz_data(1:length(ioniz_data),3); % [eV/Angstrom]

dE_dx = mean(ioniz_by_ions); % [eV/Ang] Ionization energy loss per thickness
dx = (layer(length(layer))); % [Ang] Total layer thickness
dE = dE_dx*dx; % [eV] Total ionization energy loss

E = (E0 - dE)/(1E6); % [MeV] Ionization energy for next layer

disp(['Avg. Ionization Energy Loss per Target Depth Thickness: ' ...
    num2str(dE_dx) ' [eV/Angstrom]']);
disp(['Total Ionization Energy Loss: ' num2str(dE/(1E6)) ' [MeV]']);
disp(['Final Ionization Energy: ' num2str(E) ' [MeV]']);
```

References

Alig, R. C., and S. Bloom. "Electron-hole-pair creation energies in semiconductors." Physical Review Letters 35.22 (1975): 1522.

Araki, K et al. "Experimental operations of laser communication equipment onboard ETS-VI satellite." Photonics West'97. International Society for Optics and Photonics, 1997.

Badhwar, Gautam D. "The radiation environment in low-Earth orbit." Radiation research 148.5s (1997): S3-S10.

Baker, D. N. (2002): How to cope with space weather, Science, 297(5586), 1486–1487, doi: 10.1126/science.1074956

Biddle, A., and Monteiro, T. "Space Radiation Mitigation for *Fox-1.*" AMSAT Space Symposium 2012.

Bogorad, A.L., Likar, J.J., Lombardi, R.E., Herschitz, R., and Kircher G. (2010): On-Orbit Total Dose Measurements from 1998 to 2007 Using pFET Dosimeters, IEEE Transactions on Nuclear Science, 57(6), 3154-3162, doi:10.1109/TNS.2010.2076832.

Boroson, Don M., et al. "Overview and results of the lunar laser communication demonstration." SPIE LASE. International Society for Optics and Photonics, 2014.

BridgeSat. "The Swedish Space Corporation (SSC) and BridgeSat Announce Partnership to Benefit the BridgeSat Optical Communications Network and the SSC Universal Space Network." Press Release 2017.

Buchner, Stephen, et al. "Proton Test Guideline Development – Lessons Learned." NASA/Goddard Space Flight Center. 2002.

Cannon, E. H., et al. "Heavy ion, high-energy, and low-energy proton SEE sensitivity of 90-nm RHBD SRAMs." IEEE Transactions on Nuclear Science 57.6 (2010): 3493-3499.

Ciminelli, Caterina, Francesco Dell'Olio, and Mario Nicola Armenise. PHOTONICS IN SPACE: Advanced Photonic Devices and Systems. World Scientific, 2016.

Cisco. The Zettabyte Era – Trends and Analysis. 2016. *Doc ID 1465272001812119.*

Cornwell, Donald. "Space-based laser communications break threshold." Optics and Photonics News 27.5 (2016): 24-31.

Diodes Incorporated. "AP22802 Single Channel Power Distribution Load Switch." DS36218 Rev.3-2. August 2015.

ESA. "Space Environment Standard ECSS-E-ST-10-04C" (PDF). ESA Requirements and Standards Division. November 15, 2008. Retrieved 2013-09-27.

Fields, R., et al. “NFIRE-to-TerraSAR-X laser communication results: satellite pointing, disturbances, and other attributes consistent with successful performance.” SPIE Defense, Security, and Sensing. International Society for Optics and Photonics, 2009.

Fletcher, G. D., et al. “The SILEX optical interorbit link experiment.” Electronics and communication engineering journal 3.6 (1991): 273-279.

Fujiwara, Yuuichi, et al. "Optical inter-orbit communications engineering test satellite (OICETS)." Acta Astronautica 61.1 (2007): 163-175.

Ganushkina, N. et al. "Locations of boundaries of outer and inner radiation belts as observed by Cluster and Double Star." 38th COSPAR Scientific Assembly. Vol. 38. 2010.

Gregory, M., et al. "Coherent inter-satellite and satellite-ground laser links." Proc. SPIE. Vol. 7923. No. 792303-1. 2011.

Guillermin, J. et al. “Assessment of the direct ionization contribution to the proton SEU rate.” Proc. RADECS 2016

Hartman, Spencer. “UC Davis 76 Inch Isochronous Cyclotron: Radiation Effects Infrastructure.” 2013.

Hastings, Daniel, and Henry Garrett. Spacecraft-environment interactions. Cambridge university press, 2004.

Heidel, David F., et al. "Low energy proton single-event-upset test results on 65 nm SOI SRAM." IEEE Transactions on Nuclear Science 55.6 (2008): 3394-3400.

Hemmati, Hamid. “Near-Earth Laser Communications.” Chapter 1. Introduction. Taylor & Francis Group, LLC, 2008.

Heynderickx, D. "Review on modelling of the radiation belts." International Journal of modern physics A 17.12n13 (2002): 1675-1684.

Hiemstra, David M., and Ewart W. Blackmore. "LET spectra of proton energy levels from 50 to 500 MeV and their effectiveness for single event effects characterization of microelectronics." IEEE Transactions on Nuclear Science 50.6 (2003): 2245-2250.

Hsu, Shih-Ping. Surface structure of flip chip substrate. Phoenix Precision Technology Corporation, assignee. Patent US 7382057 B2. 2008. Print.

Inphi. CL20010A1 Coherent Transceiver/Framer EVK data sheet [PDF], April 18, 2014.

Janson, S. et al. “The NASA Optical Communications and Sensor Demonstration Program: Initial Flight Results.” (2016).

Kikuchi, Kazuro. "Coherent optical communications: Historical perspectives and future directions." High Spectral Density Optical Communication Technologies. By Nakazawa et al. Springer Berlin Heidelberg, 2010. 11-49.

Lacoe, Ronald C., et al. "Application of hardness-by-design methodology to radiation-tolerant ASIC technologies." IEEE Transactions on Nuclear Science 47.6 (2000): 2334-2341.

Laser Light Communications. "HALO Global Optical Network." Website www.laserlightcomms.co/halo_network.php. 2017.

Liu Xiang, Sethumadhavan Chandrasekhar, and Peter J. Winzer. "Digital Signal Processing Techniques Enabling Multi-Tb\/s Superchannel Transmission: An overview of recent advances in DSP-enabled superchannels." IEEE Signal Processing Magazine 31.2 (2014): 16-24.

Lohmeyer, Whitney Q. "Space Radiation Environment Impacts on High Power Amplifiers and Solar Cells On-Board Geostationary Communications Satellites." Thesis. Massachusetts Institute of Technology, 2015.

Ma, Tso-Ping, and Paul V. Dressendorfer. Ionizing radiation effects in MOS devices and circuits. John Wiley & Sons, 1989.

Maurer, Richard H., et al. "RHarsh Environments: Space Radiation." Johns Hopkins APL technical digest 28.1 (2008): 17.

McMorrow, Dale, Joseph S. Melinger, and Alvin R. Knudson. "Single-event effects in III-V semiconductor electronics." International journal of high speed electronics and systems 14.02 (2004): 311-325.

Miroshnichenko, Leonty I. "Radiation Conditions in Space." Radiation Hazard in Space. Springer Netherlands, 2003. 23-46

Mutuel, L.H. "Single Event Effect Mitigation Techniques Report." Federal Aviation Administration. DOT/FAA/TC-15/62 (2016).

Nelson, Lynn E., et al. "A robust real-time 100G transceiver with soft-decision forward error correction [Invited]." *Journal of Optical Communications and Networking* 4.11 (2012): B131-B141.

Normand, Eugene. "Single event effects in avionics and on the ground." International journal of high speed electronics and systems 14.02 (2004): 285-298.

NTIA. "Authorized Frequency Usage." Manual of Regulations and Procedures for Federal Radio Frequency Management. Sept 2015 Revision of May 2013 Edition.

Oaida, Bogdan V., et al. "Optical link design and validation testing of the Optical Payload for Lasercomm Science (OPALS) system." SPIE LASE. International Society for Optics and Photonics, 2014.

Panasonic. “Megtron 6 Data Sheet: R-5775K and R-5670K Megtron 6 PPE Blend Resin System.” Santa Ana, CA. 2016.

Petersen, E. “Approaches to proton singe-event rate calculations.” IEEE Transactions on Nuclear Science 43.2 (1996): 496-504.

Petersen, E. “Single Event Effects in Aerospace”, Chapter 8, pp. 319, Wiley, 2011.

Petersen, E., et al. “Rate prediction for single event effects – a critique.” IEEE Transactions on Nuclear Science 39.6 (1992): 1577-1599.

Pfau, Timo, et al. "Coherent optical communication: Towards realtime systems at 40 Gbit/s and beyond." Optics Express 16.2 (2008): 866-872.

Poivey, Christian, and John H. Day. "Radiation hardness assurance for space systems." (2002).

Poizat, Marc. Space Radiation and its Effects on EEE Components - Total Ionizing Dose Mechanisms and Effects. N.p.: ESA/ESTEC, June 2009.

Pribil, Klaus and Hemmati, Hamid. “Near-Earth Laser Communications.” Chapter 4. Laser Transmitters: Coherent and Direct Detection. Taylor & Francis Group, LLC, 2008.

Rasmussen, Christian, et al. "Real-time DSP for 100+ Gb/s." Optical Fiber Communication Conference. Optical Society of America, 2013.

Reis, Jacklyn D., et al. "System Validation of Polymer-based Transmitter Optical Sub-Assembly for 100G/200G Modules." 2016.

Roberts, Kim, et al. "Performance of dual-polarization QPSK for optical transport systems." Journal of lightwave technology 27.16 (2009): 3546-3559.

Robinson, B., et al. "Overview of the Lunar Laser Communications Demonstration", Proc SPIE 7923 (2011).

Samaras, Anne. “Single Event Effects and Rate Calculation.” TRAD Short Course, 2014.

Sanmina-SCI Corporation. “PCB Fabrication: Buried Capacitance Technology.” 2006. PDF File.

Savory, Seb J. Electronic signal processing in optical communications. Proc. SPIE 7136, Optical Transmission, Switching, and Subsystems VI, 71362C (2008, November 11); doi:10.1117/12.806530

Seltzer, S.M. “SHIELDOSE, A Computer Code for Space-Shielding Radiation Dose Calculations.” National Bureau of Standards, NBS-IR 74457. 1980.

Seltzer, S.M. “Updated calculations for routine space-shielding radiation dose estimates: SHIELDOSE-2.” NIST Publication, NISTIR 5477. 1994.

Sinclair, Doug, and Jonathan Dyer. “Radiation effects and COTS parts in SmallSats.” (2013).

Sinclair Interplanetary. “Laser Downlink plus Star Tracker.” Datasheet2017.

Sinclair Interplanetary. “Symmetric Laser Crosslink.” Datasheet2017.

Srour, Joseph R., and James M. McGarrity. "Radiation effects on microelectronics in space." Proceedings of the IEEE 76.11 (1988): 1443-1469.

Stark, John P.W. "Chapter 2 The Spacecraft Environment and Its Effect on Design." Space Systems Engineering. Ed. Peter W. Stark, 2011.

Sun, H. et al. “Real-time measurements of a 40 Gb/s coherent system.” Optics Express 16.2 (2008): 873-879.

Swinerd G. Graham, and John P.W. Stark. Fourth ed. N.p.: John Wiley & Sons, n.d. N. pag. Print.

Stassinopoulos, E. G., and James P. Raymond. "The space radiation environment for electronics." Proceedings of the IEEE 76.11 (1988): 1423-1442.

Sukhaseum, Nicolas. “Radiation Engineering.” TRAD Short Course (2017).

Suparta, Wayan. "The variability of space radiation hazards towards LEO spacecraft." Journal of Physics: Conference Series. Vol. 539. No. 1. IOP Publishing, 2014.

Tolker-Nielsen, Toni, and Gotthard Oppenhauser. "In-orbit test result of an operational optical intersatellite link between ARTEMIS and SPOT4, SILEX." High-Power Lasers and Applications. International Society for Optics and Photonics, 2002.

Topline Corporation. “BGA Solder Ball.” 2017. http://www.topline.tv/BGA_SolderBall.html. Milledgeville, GA.

Toyoshima, Morio, et al. "Ground-to-satellite optical link tests between Japanese laser communications terminal and European geostationary satellite ARTEMIS." Lasers and Applications in Science and Engineering. International Society for Optics and Photonics, 2004.

Toyoshima, Morio. "Trends in satellite communications and the role of optical free-space communications [Invited]." Journal of Optical Networking 4.6 (2005): 300-311.

Tuite, Don. "Understanding In-Flight And In-Space Radiation Effects On CMOS Devices." Electronic Design. N.p., 21 Oct. 2013. Web. <http://electronicdesign.com/circuit-protection/understanding-flight-and-space-radiation-effects-cmos-devices>.

Tylka, Allan J., et al. “Single event upsets caused by solar energetic heavy ions.” IEEE Transactions on Nuclear Science. 43.6 (1996): 2758-2766.

Varotsou, Athina. “Space Radiation Environment.” TRAD Short Course, 2017.

Vialight. "Laser Communication. The optical fiber for the skies and beyond." Website: www.vialight.de/technology/ (2017).

Yoon, Hyosang. "Pointing System Performance Analysis for Optical Inter-satellite Communication on CubeSats." Thesis. Massachusetts Institute of Technology, 2017.

3D Plus. "Hi-Rel Latch-Up Current Limiter (LCL)." LCL/3DPM0168-2. Sept 2013.